

Cal Poly

Caltech

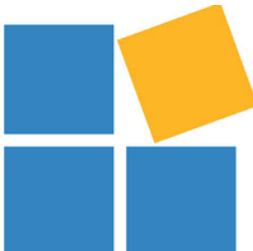
SC/EC
AN NSF+USGS CENTER

UC Irvine

UCLA

**UC Santa
Barbara**

USC



Comparison of FDHI Fault Displacement Models

Alexandra Sarmiento, P.E., C.E.G.
University of California, Los Angeles

Yousef Bozorgnia, Ph.D., P.E., F.ASCE
University of California, Los Angeles

Brian S.J. Chiou, Ph.D.
California Department of Transportation

Albert Kottke, Ph.D., P.E.
Pacific Gas & Electric Company

Chun-Hsiang Kuo, Ph.D.
National Central University
National Center for Research on Earthquake
Engineering

Christopher W.D. Milliner, Ph.D.
California Institute of Technology

Kate Thomas
California Geological Survey

Yongfei Wang, Ph.D.
Southern California Earthquake Center

Grigorios Lavrentiadis, Ph.D.
University of California, Los Angeles
California Institute of Technology

Rui Chen, Ph.D., P.G.
California Geological Survey

Timothy E. Dawson, C.E.G.
California Geological Survey

Nicolas Kuehn, Ph.D.
University of California, Los Angeles

Chris Madugo, Ph.D.
Pacific Gas & Electric Company

Robb Moss, Ph.D., P.E., F.ASCE
California Polytechnic State University

Stephen Thompson, Ph.D., C.E.G.
Lettis Consultants International

Kourosh Younesi, Ph.D., P.E.
Science and Research Branch of Azad University

Arash Zandieh, Ph.D., P.E.
Lettis Consultants International

A report on research conducted with support from Pacific Gas & Electric Company, California High-Speed Rail Authority, California Department of Transportation, Southern California Gas Company, Los Angeles Department of Water and Power, and California Energy Commission.

Report Report GIRS-2022-10
DOI: 10.34948/N3W88V

University of California, Los Angeles (headquarters)

Natural Hazards Risk & Resiliency Research Center

B. John Garrick Institute for the Risk Sciences

Comparison of FDHI Fault Displacement Models

Alexandra Sarmiento, P.E., C.E.G.

University of California, Los Angeles

Grigorios Lavrentiadis, Ph.D.

University of California, Los Angeles

California Institute of Technology

Yousef Bozorgnia, Ph.D., P.E., F.ASCE

University of California, Los Angeles

Rui Chen, Ph.D., P.G.

California Geological Survey

Brian S.J. Chiou, Ph.D.

California Department of Transportation

Timothy E. Dawson, C.E.G.

California Geological Survey

Albert Kottke, Ph.D., P.E.

Pacific Gas & Electric Company

Nicolas Kuehn, Ph.D.

University of California, Los Angeles

Chun-Hsiang Kuo, Ph.D.

National Central University

National Center for Research on Earthquake
Engineering

Chris Madugo, Ph.D.

Pacific Gas & Electric Company

Christopher W.D. Milliner, Ph.D.

California Institute of Technology

Robb Moss, Ph.D., P.E., F.ASCE

California Polytechnic State University

Kate Thomas

California Geological Survey

Stephen Thompson, Ph.D., C.E.G.

Lettis Consultants International

Yongfei Wang, Ph.D.

Southern California Earthquake Center

Kourosh Younesi, Ph.D., P.E.

Science and Research Branch of Azad
University

Arash Zandieh, Ph.D., P.E.

Lettis Consultants International

A report on research conducted with support from Pacific Gas & Electric Company, California High-Speed Rail Authority, California Department of Transportation, Southern California Gas Company, Los Angeles Department of Water and Power, and California Energy Commission.

Report GIRS-2022-10

Natural Hazards Risk and Resiliency Research Center
B. John Garrick Institute for the Risk Sciences
University of California, Los Angeles (Headquarters)

April 2023 (Initial Release)
January 2025 (Revision 1)

ABSTRACT

This report presents comparisons between four new fault displacement prediction models that were developed through the Fault Displacement Hazard Initiative (FDHI) Project. The comparisons focus on displacements occurring on principal surface ruptures; however, different definitions of displacement are used among the models, and the differences should be considered when applying the new models. All FDHI models were developed using a database of 75 events that underwent an extensive and systematic data quality review in coordination with the model developers. The new models also use advanced statistical modeling which, in most cases, includes magnitude scaling breakpoints, separation of between- and within-event aleatory components that are magnitude- and location-dependent, and estimation of the within-model epistemic uncertainty. Two of the new models are applicable to all styles of faulting, while the other two models are for strike-slip and reverse events, respectively. All new models are applicable between M 6.0 and 8.0, where most of the empirical data exist, but some are applicable to lower or higher magnitudes. Similar to previously published models, the new models use earthquake size and normalized location along the strike of the rupture as predictor variables.

The quantitative comparisons in this report capture a broad range of scenarios defined by style of faulting, magnitude, and normalized location along the rupture. Four previously published principal fault displacement models commonly used in engineering practice are also included for comparison with the new models. Average displacement predictions in the FDHI models are within a factor of about 1.5 for most magnitudes and styles of faulting and within a factor of 2.5 in all cases. The average displacements in new models are generally smaller than in previously published models. An exception is $M \sim 7$, where the average displacement predictions in the new models are roughly 40% higher. The upper-tail predictions (e.g., 99th percentile) in the FDHI models are within a factor of about 1.5 at the rupture midpoint in most cases and a factor of about 2.5 at the rupture endpoint. Compared to previously published models, the upper-tail predictions range from about 2 to 10 times lower in most cases. Importantly, the upper tails of the displacement probability distributions in the new models are in good agreement with empirical observations of maximum displacement, particularly for large magnitudes, which is driven by a combination of an expanded database and improvements to the aleatory variability modeling and magnitude scaling.

ACKNOWLEDGMENTS

Support for this project was provided by the California Energy Commission, Pacific Gas & Electric Company, California High-Speed Rail Authority, California Department of Transportation, Southern California Gas Company, and Los Angeles Department of Water and Power. Multiple individuals and organizations were partners in this project, as is evident from the list of the authors of this report.

The support of these organizations is gratefully appreciated. The opinions, findings, conclusions, or recommendations expressed in this publication are those of the authors and do not necessarily reflect the views of the study sponsors, the Natural Hazards Risk and Resilience Research Center (NHR3), or the Regents of the University of California.

This work was completed through the Fault Displacement Hazard Initiative (FDHI) Project, which is a multi-year, community-based research program. The structured but cooperative nature of the FDHI Project provided a forum for fault displacement modeling teams and database developers to have extensive interactions and fruitful technical discussions, which resulted in higher quality models than each researcher could achieve individually. Acknowledgment and appreciation are given to over 40 researchers and practicing professionals who worked on various parts of the FDHI Project. Their contributions, dedication, and teamwork are greatly appreciated.

ADDENDUM FOR REVISION 1

This report has been updated since its original release to reflect the final models published in the “Fault Displacement Hazard Analysis Special Collection” of *Earthquake Spectra*, which is the peer-reviewed journal of the Earthquake Engineering Research Institute (EERI). Most new models are also documented in reports available through the Natural Hazards Risk and Resiliency Research Center (NHR3). The text, tables, figures, appendices, and chapter layout have been revised since the original release.

CONTENTS

| | |
|--------------------------------------------------------------------------------|-------------|
| ABSTRACT | iii |
| ACKNOWLEDGMENTS | iv |
| ADDENDUM FOR REVISION 1..... | v |
| TABLE OF CONTENTS | vi |
| LIST OF FIGURES | viii |
| LIST OF TABLES | xi |
| 1 Introduction..... | 1 |
| 2 Definitions of Displacement Used in Fault Displacement Models..... | 4 |
| 2.1 Displacement Vector Component | 4 |
| 2.2 Participating Ruptures..... | 7 |
| 3 Model Formulations and Parameters | 10 |
| 4 Data Set Selection and Model Applicability | 18 |
| 4.1 Data Set Selection | 18 |
| 4.2 Model Applicability | 21 |
| 5 Model Comparisons | 22 |
| 5.1 x/L Scaling | 23 |
| 5.2 Average Displacement | 25 |
| 5.3 Maximum Displacement..... | 28 |
| 5.4 Median Predictions | 32 |
| 5.5 Aleatory Variability | 33 |
| 5.5.1 Cumulative Distributions and Percentiles..... | 33 |
| 5.5.2 Exceedance Probabilities | 50 |
| 6 Epistemic Uncertainty | 53 |
| 6.1 LA23 Model..... | 53 |
| 6.2 MEA24 model..... | 58 |
| 6.3 KEA24 Model..... | 60 |
| 6.4 CEA25 Model | 66 |
| 7 Summary..... | 68 |
| REFERENCES..... | 71 |

**APPENDIX A: PRELIMINARY COMPARISONS OF RESULTS FROM DIFFERENT
DISPLACEMENT SUMMATION APPROACHES**

LIST OF FIGURES

| | | |
|-------------|------------------------------------------------------------------------------------------------------------------------------------------------|----|
| Figure 2.1 | Fault displacement vector components. | 6 |
| Figure 2.2 | Example of complex surface rupture pattern and irregularly spaced displacement measurement sites from a fictitious earthquake. | 7 |
| Figure 2.3 | Scaling of sum-of-principal displacement (D_{sp}) with aggregate displacement (D_{agg}) in the LA23 model. | 9 |
| Figure 3.1 | Example empirical displacement profiles showing principal displacements. Normalized distance ratio x/L is shown on the top axis. | 14 |
| Figure 5.1 | Comparison of x/L scaling using equal-area mean profiles. | 24 |
| Figure 5.2 | Comparison of magnitude scaling for average displacement. | 27 |
| Figure 5.3 | Number of standard deviations corresponding to the median prediction for maximum displacement in the LA23 FDM for aggregate displacement. | 29 |
| Figure 5.4 | Comparison of magnitude scaling using the median prediction for maximum displacement. | 31 |
| Figure 5.5 | Comparison of aleatory variability for strike-slip M 6.0. | 35 |
| Figure 5.6 | Comparison of aleatory variability for strike-slip M 6.8. | 36 |
| Figure 5.7 | Comparison of aleatory variability for strike-slip M 7.2. | 37 |
| Figure 5.8 | Comparison of aleatory variability for strike-slip M 7.7. | 38 |
| Figure 5.9 | Comparison of aleatory variability for strike-slip M 8.0. | 39 |
| Figure 5.10 | Comparison of aleatory variability for reverse M 6.0. | 40 |
| Figure 5.11 | Comparison of aleatory variability for reverse M 6.8. | 41 |
| Figure 5.12 | Comparison of aleatory variability for reverse M 7.2. | 42 |
| Figure 5.13 | Comparison of aleatory variability for reverse M 7.7. | 43 |
| Figure 5.14 | Comparison of aleatory variability for reverse M 8.0. | 44 |
| Figure 5.15 | Comparison of aleatory variability for normal M 6.0. | 45 |
| Figure 5.16 | Comparison of aleatory variability for normal M 6.8. | 46 |

| | | |
|-------------|-----------------------------------------------------------------------------------------------------------------|----|
| Figure 5.17 | Comparison of aleatory variability for normal M 7.2. | 47 |
| Figure 5.18 | Comparison of aleatory variability for normal M 7.7. | 48 |
| Figure 5.19 | Comparison of aleatory variability for normal M 8.0. | 49 |
| Figure 5.20 | Comparison of probability of exceedance curves at rupture midpoint. | 51 |
| Figure 5.21 | Comparison of probability of exceedance curves at rupture endpoint. | 52 |
| Figure 6.1 | LA23 epistemic uncertainty model for the predicted median aggregate displacement in transformed units. | 54 |
| Figure 6.2 | Comparison of LA23 within-model epistemic uncertainty at rupture endpoints for strike-slip events. | 55 |
| Figure 6.3 | Comparison of LA23 within-model epistemic uncertainty at rupture midpoints for strike-slip events. | 55 |
| Figure 6.4 | Comparison of LA23 within-model epistemic uncertainty at rupture endpoints for reverse events. | 56 |
| Figure 6.5 | Comparison of LA23 within-model epistemic uncertainty at rupture midpoints for reverse events. | 56 |
| Figure 6.6 | Comparison of LA23 within-model epistemic uncertainty at rupture endpoints for normal events. | 57 |
| Figure 6.7 | Comparison of LA23 within-model epistemic uncertainty at rupture midpoints for noraml events. | 57 |
| Figure 6.8 | Comparison of MEA24 within- and between-model epistemic uncertainty at rupture endpoints. | 59 |
| Figure 6.9 | Comparison of MEA24 within- and between-model epistemic uncertainty at rupture midpoints. | 59 |
| Figure 6.10 | KEA24 estimated epistemic uncertainty on the predicted median in Box-Cox transformation units. | 61 |
| Figure 6.11 | KEA24 estimated epistemic uncertainty on the predicted standard deviation in Box-Cox transformation units. | 61 |
| Figure 6.12 | Logic tree for capturing epistemic uncertainty in median prediction and standard deviation in KEA24 model. | 62 |

| | | |
|-------------|----------------------------------------------------------------------------------------------------------|----|
| Figure 6.13 | Comparison of KEA24 within-model epistemic uncertainty at rupture endpoints for strike-slip events. | 63 |
| Figure 6.14 | Comparison of KEA24 within-model epistemic uncertainty at rupture midpoints for strike-slip events. | 63 |
| Figure 6.15 | Comparison of KEA24 within-model epistemic uncertainty at rupture endpoints for reverse events. | 64 |
| Figure 6.16 | Comparison of KEA24 within-model epistemic uncertainty at rupture midpoints for reverse events. | 64 |
| Figure 6.17 | Comparison of KEA24 within-model epistemic uncertainty at rupture endpoints for normal events. | 65 |
| Figure 6.18 | Comparison of KEA24 within-model epistemic uncertainty at rupture midpoints for normal events. | 65 |
| Figure 6.19 | Comparison of CEA25 within-model epistemic uncertainty at rupture endpoints. | 67 |
| Figure 6.20 | Comparison of CEA25 within-model epistemic uncertainty at rupture midpoints. | 67 |

LIST OF TABLES

| | | |
|-----------|---------------------------------------------------------------------------------------------|----|
| Table 1.1 | Fault displacement models (FDMs) compared in this report..... | 2 |
| Table 2.1 | Summary of displacement definitions used in the FDMs evaluated in this report..... | 5 |
| Table 3.1 | Summary of metrics provided in fault displacement models and their predictor variables..... | 11 |
| Table 3.2 | Summary of fault displacement model formulations and aleatory variability components..... | 12 |
| Table 3.3 | Summary of model scaling components..... | 16 |
| Table 4.1 | Summary of data sets used in models for x/L scaling. | 20 |
| Table 4.2 | Summary of data sets used in models for magnitude scaling. | 20 |
| Table 4.3 | Recommended model applicabilit..... | 21 |

1 Introduction

The Fault Displacement Hazard Initiative (FDHI) Project is a multi-year, community-based research project coordinated by the University of California. The objectives of the project are to compile a comprehensive fault rupture and displacement database and develop a set of next-generation empirical fault displacement models. The new database is documented in a separate report available through the Natural Hazards Risk and Resiliency Research Center (NHR3) web site (Sarmiento et al., 2021). The database was compiled in coordination with the model developers, and all data were systematically and repeatedly reviewed for quality, completeness, and consistency. Using the new empirical database, four research teams developed new fault displacement amplitude prediction models, which we refer to more generally as Fault Displacement Models (FDMs).

This report provides a comparison of the four new FDMs developed through the FDHI Project (Table 1.1). The new models are available in the “Fault Displacement Hazard Analysis Special Collection” of *Earthquake Spectra*¹, which is the peer-reviewed journal of the Earthquake Engineering Research Institute (EERI). Most new models are also documented in NHR3 reports.

For completeness, four previously published FDMs commonly used in engineering practice are also included in the comparisons (Table 1.1). The list of existing FDMs is not intended to be exhaustive because our focus is on comparing features and predictions of the new models; however, including common existing models provides a useful point-of-reference for the predictions in the new models. For example, the Wells and Coppersmith (1994) magnitude scaling relations for average and maximum displacement are included because they are familiar to most practitioners, although many other displacement–magnitude scaling relations are available. The Takao et al. (2013, 2018) models are based on a regional dataset and are generally not used outside of Japan, so they are excluded to simplify the comparisons. While some previously published FDMs provided predictions for principal and distributed fault displacements, the comparisons in this study are for principal or aggregate displacements only². Other elements of a full probabilistic

¹ Earthquake Spectra’s “Fault Displacement Hazard Analysis Special Collection” is available at https://journals.sagepub.com/topic/collections-eqs/eqs-1-fault_displacement_hazard_analysis_special_collection/eqs.

² The terms principal, distributed, and aggregate displacement are defined in Chapter 2.

fault displacement hazard analysis (PFDHA) implementation, such models for the conditional probability of surface rupture (e.g., Wells and Coppersmith, 1993), also are not considered here.

Table 1.1. Fault displacement models (FDMs) compared in this report.

| Status | Model Name / Authors | Abbreviation ⁽¹⁾ | Journal DOI ⁽²⁾ | NHR3 DOI |
|----------|-----------------------------------------------------------------------------------------------------------------------|-----------------------------|----------------------------|----------------------|
| New | Lavrentiadis and Abrahamson (2023) <i>G. Lavrentiadis N. Abrahamson</i> | LA23 | 10.1177/87552930231201531* | Report not available |
| New | Moss et al. (2024) <i>R. Moss S. Thompson C.-H. Kuo K. Younesi D. Baumont</i> | MEA24 | 10.1177/87552930241288560* | 10.34948/N3F595 |
| New | Kuehn et al. (2024) <i>N. Kuehn A. Kottke A. Sarmiento C. Madugo Y. Bozorgnia</i> | KEA24 | 10.1177/87552930241291077* | 10.34948/N3X59H |
| New | Chiou et al. (2025) <i>B. Chiou R. Chen K. Thomas C. Milliner T. Dawson M. Petersen</i> | CEA25 | To Be Assigned* | 10.34948/N3RG6X |
| Existing | Wells & Coppersmith (1994) | WC94 | 10.1785/BSSA0840040974 | Not applicable |
| Existing | Youngs et al. (2003) | YEA03 | 10.1193/1.1542891 | Not applicable |
| Existing | Petersen et al. (2011) | PEA11 | 10.1785/0120100035 | Not applicable |
| Existing | Moss & Ross (2011) | MR11 | 10.1785/0120100248 | Not applicable |

⁽¹⁾ The abbreviation “EA” (*et al.*) is used for models with more than two authors.

⁽²⁾ Asterisk (*) indicates article is part of the “Fault Displacement Hazard Analysis Special Collection” published in 2025 by *Earthquake Spectra*.

We begin with a discussion on the different definitions of displacement used in FDMs in Chapter 2. Users should consider the different definitions of displacement when applying the new models. Chapter 3 provides a general overview of the model formulations and parameters, and Chapter 4 summarizes the data sets used in the development of each model and the recommended applicability ranges for each model. Comparisons of the model predictions are presented in

Chapter 5, and examples of within-model epistemic uncertainty are provided in Chapter 6. The results and conclusions of this report are summarized in Chapter 7.

Median comparisons are shown for all magnitudes, normalized locations along rupture, and style of faulting. The aleatory and epistemic comparisons are provided for several scenarios defined by style of faulting, moment magnitude, and normalized location along rupture. While the range of scenarios considered herein is not exhaustive, it is broad enough to demonstrate similarities and differences between the models. Similar to the Next Generation Attenuation (NGA) Program's comparisons for ground motion models (Abrahamson et al., 2008; Gregor et al., 2014, 2022), we provide explanations of key differences, but detailed evaluations of the performance of each model are outside the scope of this report.

The FDHI Project facilitated extensive collaboration among geologists, earthquake engineers, model developers, practicing professionals, end-users, and sponsors. The collaboration occurred in monthly project meetings beginning in June 2018 and several topical working group meetings related to database development, model development, and model comparisons. Each new model team is also participating in the International Atomic Energy Agency (IAEA) probabilistic fault displacement hazard analysis (PFDHA) benchmarking study (Valentini et al., 2021). Detailed evaluations of model strengths and weaknesses conducted through the FDHI Project meetings and IAEA PFDHA benchmarking study informed the discussions and comparisons in this report.

2 Definitions of Displacement Used in Fault Displacement Models

Fault displacement models predict different definitions of displacement. The definition is based on the data used to develop the model, data processing or analysis performed by the modelers, and recommendations from the model developers. For example, the data might be limited to a specific style of faulting, displacement vector component, or type of rupture (e.g., principal, distributed, or summed across multiple ruptures). Understanding the displacement definition used in the FDM is necessary to correctly interpret and apply the results, compare results between models, and use alternative models to capture epistemic uncertainty.

Surface ruptures are usually classified as principal or distributed (e.g., Coppersmith and Youngs, 2000; Stepp et al., 2001; Youngs et al., 2003; Petersen et al., 2011). Principal ruptures are the surface projection of the fault plane that generated the earthquake and ruptured at depth. Distributed ruptures are the other secondary ruptures, splays, and shears. Principal and distributed data are usually treated separately in model development because the data and driving mechanisms are sufficiently different.

The definitions of displacement in the FDMs compared in this report are listed in Table 2.1. Most models that were developed for a specific style of faulting predict the associated displacement vector component (e.g., the MR11 model was developed for reverse faulting and predicts vertical displacement). The previously published models for principal faulting are assumed to apply to single-stranded principal ruptures; however, three new FDMs combine displacements across multi-stranded ruptures. The vector components and participating ruptures assumed in the FDMs are discussed separately below.

2.1 DISPLACEMENT VECTOR COMPONENT

Figure 2.1 illustrates the vector components that accommodate fault displacement. Post-earthquake measurements of fault displacement correspond to a specific component. The measured component is typically based on the style of faulting; for example, lateral displacement is usually measured in strike-slip earthquakes, and vertical displacement is usually measured in reverse and

normal earthquakes. The fault-normal (heave) component is rarely measured in strike-slip events because it is small for steeply dipping faults. In reverse events, it is rarely reported because it is difficult to measure in compressional deformation. The fault-normal component is more easily measured in extensional deformation, so it is occasionally reported in normal faulting events. Direct measurements of net displacement are rare, and less than 10% of the measurements in the FDHI Database (Sarmiento et al., 2021) are for the net component.

Table 2.1. Summary of displacement definitions used in the FDMs evaluated in this report.

| Model | Style of Faulting ⁽¹⁾ | | | Vector Component ⁽²⁾ | Participating Ruptures ⁽³⁾ | Abbreviation ⁽⁴⁾ |
|-------|----------------------------------|----|----|---------------------------------|---------------------------------------|-----------------------------|
| | SS | RV | NM | | | |
| LA23 | ✓ | ✓ | ✓ | Net* | Aggregate | $D_{agg,N*}$ |
| | | | | | Sum-of-Principal | $D_{sp,N*}$ |
| MEA24 | — | ✓ | — | Vertical | Single Principal | $D_{p,V}$ |
| KEA24 | ✓ | ✓ | ✓ | Net* | Aggregate | $D_{agg,N*}$ |
| CEA25 | ✓ | — | — | Net* | Sum-of-Principal | $D_{sp,N*}$ |
| WC94 | ✓ | ✓ | ✓ | Varies by style | Single Principal | $D_{p,X}$ |
| YEA03 | — | — | ✓ | Vertical | Single Principal | $D_{p,V}$ |
| PEA11 | ✓ | — | — | Lateral | Single Principal | $D_{p,L}$ |
| MR11 | — | ✓ | — | Vertical | Single Principal | $D_{p,V}$ |

⁽¹⁾ SS = Strike-slip; RV = Reverse; NM = Normal.

⁽²⁾ Best-estimate data for the Net* component may be incomplete; see text for discussion.

⁽³⁾ Aggregate refers to displacements summed across principal and distributed rupture.

⁽⁴⁾ Abbreviation for displacement D with subscripts identifying the participating ruptures and vector component.

The FDHI Database contains best-estimate net displacement amplitudes for all measurement sites. These values are based on direct measurements of the net component when available; otherwise, they are calculated from the available measurements. While the true net component can be computed as the vector sum of the lateral, fault-normal, and vertical components, it is very rare for all three orthogonal components to be measured at an individual site. The values of unreported components are assumed to be zero for the purposes of calculating the best-estimate net displacement amplitudes; as a result, the calculated values in the FDHI Database may systematically underestimate the true net displacement for oblique-slip events. (We note that the database includes flags for non-zero but unmeasured components and these calculated net displacement values have a lower quality ranking.)

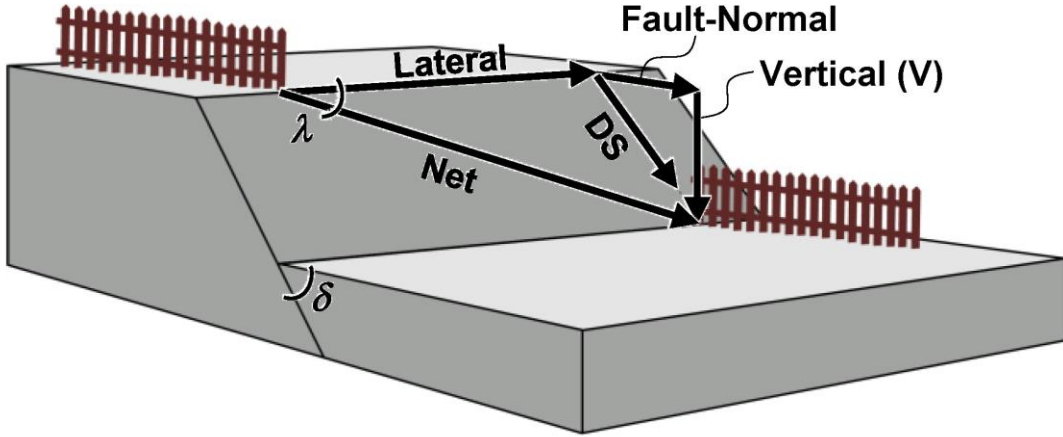


Figure 2.1. Fault displacement vector components. “DS” is dip-slip component. Angle δ is the fault dip, and angle λ is the rake. The net component is the vector sum of the lateral, fault-normal, and vertical components. The net component can also be calculated from trigonometric ratios using the dip and rake; see text for discussion.

The new FDMs use the FDHI Database, and three new FDMs predict the net component of displacement (Table 2.1). We use an asterisk (e.g., Net^* or N^*) to emphasize that the data for the best-estimate net component is incomplete in the FDHI Database and this limitation is inherited by the models. This can impact the models differently depending on the style of faulting. For example, it is generally more common for strike-slip event data sets to report both lateral and vertical components, and the fault-normal component is usually negligible for steeply dipping faults; therefore, best-estimate net displacement calculations values for strike-slip events are usually close to the true net displacement. For normal earthquakes, lateral and fault-normal components might be missing in some cases. Finally, for reverse events, both lateral and fault-normal components are commonly under-reported and the best-estimate (calculated) net displacement values in the FDHI Database may under-predict the true net displacement.

Trigonometric ratios can be used to compute the true net displacement (N) from the best-estimate net (N^*) or vertical (V) displacement predicted by the FDMs in site-specific application:

$$N = \frac{N^*}{\sin(\delta)} \quad (2.1)$$

$$N = \frac{V}{\sin(\delta)\sin(\lambda)} \quad (2.2)$$

where the fault dip (δ) and rake (λ) are schematically shown on Figure 2.1. (It is noted that the λ in Figure 2.1 is unrelated to the Box-Cox transformation parameter λ in the KEA24 model; the use of the same symbol is coincidental.)

2.2 PARTICIPATING RUPTURES

Surface rupture characteristics can vary from a single, spatially continuous discrete faults to networks of discontinuous fault segments with gaps and step-overs. Fault displacement is typically measured on individual ruptures. Figure 2.2 shows an example of a complex surface rupture pattern with (sub)parallel principal ruptures and nonuniform spatial distribution of fault displacement measurement sites. In previously published models for principal fault displacement, principal displacement measurements from all principal rupture segments are projected onto a reference line (defined by the nominal along-strike direction of the total rupture), effectively treating the measurements as adjacent along a single nominal principal rupture. The new MEA24 FDM also uses this approach, which is referred to as “single principal” in Table 2.1

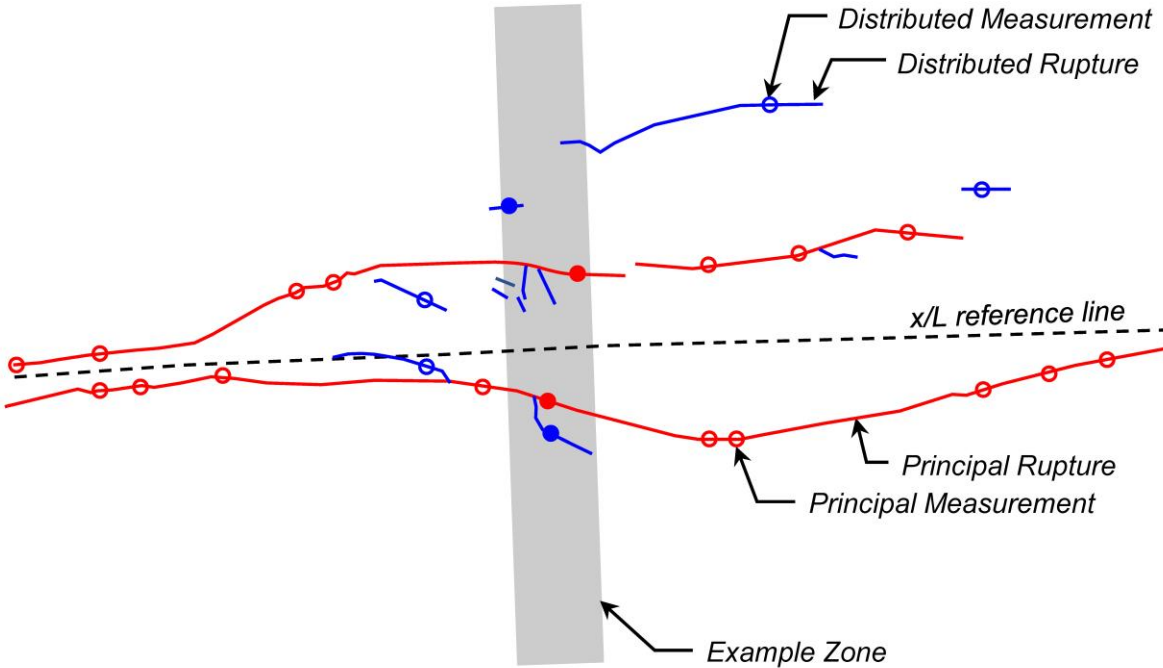


Figure 2.2. Example of complex surface rupture pattern (lines) and irregularly spaced displacement measurement sites (open and closed circles) from a fictitious earthquake. Reference line represents nominal along-strike path of the total rupture. See text for discussion on the different displacements that may be summed in the example zone.

Alternatively, three new FDMs sum displacements across (sub)parallel ruptures to capture the impact of surface rupture complexity on displacement amplitude. Summing the displacements was viewed as a more stable metric by some modeler teams to account for complex surface rupture effects that are not modeled. The CEA25 model only considers principal displacement measurements in the summation, which we refer to as “sum-of-principal” in Table 2.1. The KEA24 model includes all measurements (principal and distributed), which is referred to as “aggregate.” The LA23 modeling team developed models for both aggregate and sum-of-principal. Each team (KEA24, CEA25, and LA23) used a unique method to sum the displacements in the example zone on Figure 2.2, but all methods aimed to account for irregular spacing of displacement measurement sites, which is common in field data sets due to various geologic or logistic factors.

To better understand the impact of the different displacement summation approaches, an FDHI Working Group was convened to review results from six earthquakes. The findings are documented in Appendix A. In general, the Working Group found reasonable agreement among the different methods. However, direct comparisons between models that predict aggregate and principal displacements are not possible, and adjustments between predictions for aggregate and principal or sum-of-principal are not available in most models. The exception is the LA23 model, which provides formulations for sum-of-principal and aggregate. To provide a rough idea of the scaling between sum-of-principal and aggregate displacements, we show the LA23 scaling model in Figure 2.3. The scaling is independent of earthquake size and site location in the LA23 model. While the scaling in the LA23 model generally agrees with the principal-to-aggregate displacement ratios for the six events evaluated in Appendix A, it is specific to the LA23 model and should not be applied to other models.

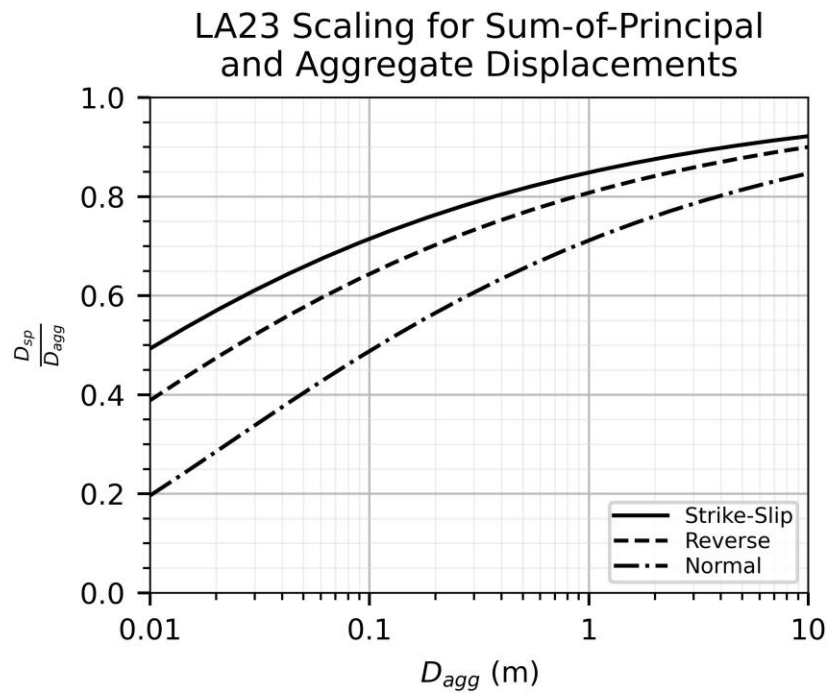


Figure 2.3. Scaling of sum-of-principal displacement (D_{sp}) with aggregate displacement (D_{agg}) in the LA23 model. Reproduced from Figure A16 in Lavrentiadis and Abrahamson (2023).

3 Model Formulations and Parameters

This chapter provides a high-level overview of the formulations, parametrizations, and aleatory variability modeling in FDMs. The model equations, coefficients, and details on the model development are outside the scope of this discussion and can be found in the source publications listed in Table 1.1.

Fault displacement models predict various displacement metrics. Early models by Bonilla et al. (1984), Wells and Coppersmith (1994), and several others developed empirical scaling relations between earthquake size and average or maximum displacement (AD and MD , respectively). More recent models by Youngs et al. (2003), Moss and Ross (2011), and Petersen et al. (2011) provide predictions for displacement normalized by the average and/or maximum displacement in an earthquake (D/AD and D/MD , respectively). Petersen et al. (2011) also provide formulations for the displacement amplitude itself (D). Three of the new FDHI FDMs predict displacement D (LA23, KEA24, and CEA25), whereas the MEA24 model predicts normalized displacements D/AD and D/MD . Additionally, the LA23 and CEA25 models provide predictions for AD , and LA23 also provides prediction for MD . Table 3.1 summarizes the displacement metrics provided in each model. The definitions of displacement from Table 2.1 are repeated for convenience.

The FDMs evaluated in this report use moment magnitude (M) and/or normalized location along-strike of the rupture (x/L) as predictor variables. The normalized location x/L is a distance ratio, where x is the length along the surface rupture and L is the total surface rupture length. Some models use alternative notations for x/L (e.g., l/L in PEA11, X/L in LA23, U_* in KEA24, and $l2L$ in CEA25). The location is normalized with respect to the total surface rupture length to remove the effects of variable surface rupture lengths. The estimated surface rupture length for a given earthquake magnitude and its aleatory variability is handled in the PFDHA integral using scaling relations for magnitude and surface rupture length.

The predictor variables vary based on the displacement metric used in the FDM (Table 3.1). For example, FDMs that predict the AD or MD in an earthquake are independent of along-strike location. An exception is the LA23 model, which uses the prediction at $x/L = 0.25$ as an arbitrary reference. Fault displacement models that predict normalized displacements D/AD or D/MD are independent of earthquake size. Normalized displacement models are coupled with

scaling relations for the normalization variable (AD or MD) to capture the effects of earthquake size.

Table 3.1. Summary of metrics provided in fault displacement models and their predictor variables.

| Model | Metric | Definition of Displacement ⁽¹⁾ | Predictor Variables ⁽²⁾ |
|-------|--------|-------------------------------------------|------------------------------------|
| LA23 | AD | D_{sp,N^*} or D_{agg,N^*} | $\mathbf{M}, x/L$ |
| | MD | D_{sp,N^*} | $\mathbf{M}, D(x/L = 0.25)$ |
| | MD | D_{agg,N^*} | $\mathbf{M}, D(x/L = 0.25)$ |
| MEA24 | AD | $D_{p,v}$ | \mathbf{M} |
| | MD | | \mathbf{M} |
| | D/AD | | x/L |
| | D/MD | | x/L |
| KEA24 | D | D_{agg,N^*} | $\mathbf{M}, x/L$ |
| CEA25 | D | D_{sp,N^*} | $\mathbf{M}, x/L$ |
| | AD | | \mathbf{M} |
| WC94 | AD | $D_{p,x}$ | \mathbf{M} |
| | MD | $D_{p,x}$ | \mathbf{M} |
| YEA03 | D/AD | $D_{p,v}$ | x/L |
| | D/MD | | x/L |
| PEA11 | D | $D_{p,L}$ | $\mathbf{M}, x/L$ |
| | D/AD | | x/L |
| MR11 | AD | $D_{p,v}$ | \mathbf{M} |
| | MD | | \mathbf{M} |
| | D/AD | | x/L |
| | D/MD | | x/L |

⁽¹⁾ Definition of response variable D , AD , and/or MD used in model formulation from Table 2.1.

⁽²⁾ Models applicable to multiple styles of faulting use the same predictor variables, but the functional forms and/or coefficients vary by style.

The aleatory variability is defined through the statistical distribution used in each FDM. Several different statistical distributions are used (e.g., lognormal, gamma, beta, and power-normal). In most models, the aleatory variability is partitioned into between- and within-event components, where the between-event variability is either magnitude-dependent or constant, and the within-event variability is location-dependent. Exceptions include the PEA11 models, which did not partition the variability, and the LA23 model, in which both terms are magnitude-dependent. Within-event variability is not applicable to models that predict AD or MD . Separating the aleatory variability into between- and within-event components avoids bias towards better-sampled events. Including magnitude- and location-dependence in the aleatory variability models improves hazard estimates because data dispersion is not constant for all magnitudes or locations

along the rupture. In models applicable to multiple styles of faulting (LA23 and KEA24), the between- and within-event components use different functional forms and/or coefficients for each style. The statistical distributions and aleatory components for each FDM are listed in Table 3.2.

Table 3.2. Summary of fault displacement model formulations and aleatory variability components.

| Model | Formulation ⁽¹⁾ | Between-Event ⁽²⁾ | Within-Event ⁽³⁾ |
|----------------------|---------------------------------------|------------------------------|-----------------------------|
| LA23 ⁽⁴⁾ | $D^{0.3} \sim Normal$ | \mathbf{M} -dependent | \mathbf{M} -dependent |
| MEA24 | $\log_{10}(AD) \sim Normal$ | Constant | – |
| | $\log_{10}(MD) \sim Normal$ | Constant | – |
| | $D/AD \sim Gamma$ | – | x/L -dependent |
| | $D/MD \sim Gamma$ | – | x/L -dependent |
| KEA24 | $(D^\lambda - 1)/\lambda \sim Normal$ | \mathbf{M} -dependent | x/L -dependent |
| CEA25 | $\ln(D) \sim nEMG$ | \mathbf{M} -dependent | x/L -dependent |
| WC94 | $\log_{10}(AD) \sim Normal$ | Constant | – |
| | $\log_{10}(MD) \sim Normal$ | Constant | – |
| YEA03 | $D/AD \sim Gamma$ | – | x/L -dependent |
| | $D/MD \sim Beta$ | – | x/L -dependent |
| PEA11 ⁽⁵⁾ | $\ln(D) \sim Normal$ | Constant ⁽⁶⁾⁽⁷⁾ | |
| | $\ln(D/AD) \sim Normal$ | Constant | Constant ⁽⁷⁾ |
| MR11 | $\log_{10}(AD) \sim Normal$ | Constant | – |
| | $\log_{10}(MD) \sim Normal$ | Constant | – |
| | $D/AD \sim Gamma$ | – | x/L -dependent |
| | $D/AD \sim Weibull$ | – | x/L -dependent |
| | $D/MD \sim Beta$ | – | x/L -dependent |

⁽¹⁾ Describes response variable and statistical distribution. Variables D , AD , and MD are displacement, average displacement, and maximum displacement, respectively. $nEMG$ is negative exponentially-modified Gaussian distribution (CEA25), and λ is Box-Cox transformation parameter (KEA24).

⁽²⁾ Between-event variability for models that predict D/AD or D/MD is provided by the AD or MD scaling relation and is typically constant.

⁽³⁾ Within-event variability for is not applicable for models that AD or MD .

⁽⁴⁾ The LA23 simplified FDM uses an additional \mathbf{M} -dependent within-even term to capture aleatory variability on fault segmentation

⁽⁵⁾ Alternative functional forms are provided for elliptical, quadratic, and bilinear profile shapes.

⁽⁶⁾ Error term was not separated.

⁽⁷⁾ Bilinear functional form is x/L -dependent.

Data transformations are commonly used to simplify statistical modeling, such as when the normality of residuals or residuals can be improved or nonlinear relationships can be linearized. For example, the Wells and Coppersmith (1994) scaling relations for AD and MD model the aleatory variability with a lognormal distribution by using a common (base 10) log transformation with a normal distribution. Two of the new FDHI FDMs use novel data transformations: the LA23 model uses a simple power transformation with an exponent of 0.3, and the KEA24 model uses a Box-Cox transformation, which is also a power transformation, that additionally shifts and scales the data. The data transformations used in each model are shown in Table 3.2.

In most cases, data transformations are not used for normalized displacements (Table 3.2). An exception is the Petersen et al. (2011) D/AD model, which uses a natural log transformation with a normal distribution. In forward application of normalized displacement models, the aleatory variability on the AD or MD should be convolved with the aleatory variability on the D/AD or D/MD . Common approaches for convolving statistical distributions include Monte Carlo sampling (Moss and Ross, 2011) and numerical integration (A. Zandieh, pers. comm.). Examples of both approaches are provided in Supplement B of Sarmiento et al. (2025).

We use the terms *magnitude scaling* to describe the relationship between displacement amplitude and the earthquake magnitude and x/L *scaling* to describe the relative relationship between displacement and the location along the rupture (i.e., the shape of the displacement profile). Table 3.3 provides qualitative descriptions of the scaling relationships used in each model.

The previously published models all use log-linear magnitude scaling. Three of the new FDHI FDMs use bilinear or trilinear magnitude scaling (LA23, KEA24, and CEA25). Although the MEA24 model uses log-linear magnitude scaling, the nonlinear magnitude scaling in the LA23 and KEA24 models approaches log-linear for reverse faulting, as discussed in Chapter 5.

The x/L scaling used in each FDM is a modeling decision. In most cases, modelers developed empirical displacement profiles from the earthquakes in the FDHI Database (e.g., Figure 3.1) and used this information to prescribe an along-strike functional form and develop a parametric model. One exception is the MEA24 model, where the x/L scaling is based on piecewise linear interpolation of pre-computed statistical distribution parameters and thus is non-parametric. (Alternatively, MEA24 provide regressions for the statistical distribution parameters in Moss et al., 2022; however, the interpolation method is preferred by the model developers per R. Moss, pers. comm.) Another exception is the LA23 model, in which the shape of the displacement profile is determined from simulations in the wavenumber domain (where the wavenumber model is based on the FDHI Database), and a space domain functional form with consistent taper scaling is provided for forward application. As discussed in Chapter 5, profile shapes vary with style of faulting.

Previous studies have found displacement profiles are commonly asymmetric (Hemphill-Haley and Weldon, 1999; Manighetti et al., 2005; Wesnousky, 2008; Youngs et al., 2003). Because the skewness usually cannot be determined *a priori*, most model developers “fold” empirical

displacement profiles about the rupture midpoint ($x/L = 0.5$) and use the folded data sets to develop the FDM. This approach leads to symmetrical profile predictions and captures asymmetry in the aleatory variability. An exception is the KEA24 model, which used the full (“unfolded”) normalized rupture length with the peak displacement located left of the rupture midpoint (i.e., at $x/L \leq 0.5$). The KEA24 model thus produces asymmetrical profiles; however, in forward applications, right- and left-skew profiles should be equally weighted in most cases, resulting in a symmetrical prediction that effectively treats the asymmetry as aleatory variability by marginalizing over the location. Additionally, the CEA25 model team provides an alternative unfolded formulation for applications where asymmetry is appropriate.

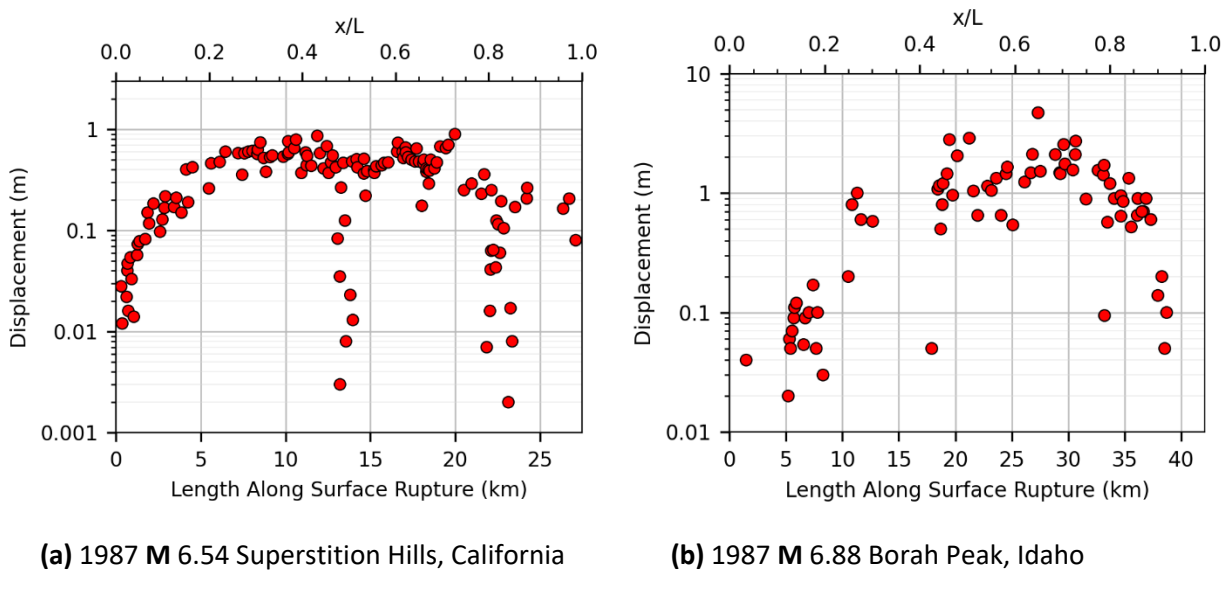


Figure 3.1. Example empirical displacement profiles showing principal displacements. Normalized distance ratio x/L is shown on top axis, where x is the length along the surface rupture and L is the total surface rupture length. Note rupture extends beyond measurements in the Borah Peak data set.

The x/L scaling is parameterized only using the normalized location along the rupture length in most FDMs. As a result, profile shapes are self-similar and independent of earthquake size in most cases. An exception is the LA23 model, which uses both M and x/L to determine the median profile shape. Although the functional form for the x/L scaling in the KEA24 model only depends on x/L , the data transformation used in their model does not preserve a constant scaling ratio and thus introduces a dependence on displacement amplitude that produces non-self-similar profiles.

Finally, we note that LA23 provide a model that is applicable to individual segments (x_{seg}/L_{seg}) and a “simplified FDM without segmentation” that uses the total surface rupture

length (x/L). Our focus throughout this report is on their simplified FDM that uses x/L , as other FDMs are developed for x/L . Further discussion on key differences in the LA23 FDMs in forward application are provided below.

Table 3.3. Summary of model scaling components.

| Model | Metric | Magnitude Scaling | | x/L Scaling | | | |
|-------|-------------------|----------------------------------------------------------|---------------------|-----------------------------------------|-----------------------|---------------------|----------------------|
| | | Prescribed Magnitude Scaling Relationship ⁽¹⁾ | Predictor Variables | Prescribed Profile Shape ⁽¹⁾ | Folded About Midpoint | Predictor Variables | Self-Similar Scaling |
| LA23 | D | Trilinear | \mathbf{M} | Approx. Quadratic ⁽²⁾ | Yes | $\mathbf{M}, x/L$ | No ⁽⁵⁾ |
| MEA24 | AD and MD | Linear | \mathbf{M} | — | — | — | — |
| | D/AD and D/MD | — | — | Approx. Quadratic ⁽³⁾ | Yes | x/L | Yes |
| KEA24 | D | Bilinear | \mathbf{M} | Beta Distribution PDF | No | x/L | No ⁽⁶⁾ |
| CEA25 | D | Bilinear | \mathbf{M} | Elliptical | Yes ⁽⁴⁾ | x/L | Yes |
| WC94 | AD and MD | Linear | \mathbf{M} | — | — | — | — |
| YEA03 | D/AD and D/MD | — | — | Linear | Yes | x/L | Yes |
| PEA11 | D | Linear | \mathbf{M} | Bilinear, Quadratic, or Elliptical | Yes | x/L | Yes |
| | D/AD | — | — | | | — | |
| MR11 | AD and MD | Linear | \mathbf{M} | — | — | — | — |
| | D/AD | — | — | Approx. Cubic Polynomial | Yes | x/L | Yes |
| | D/MD | — | — | Approx. Linear | Yes | x/L | Yes |

⁽¹⁾ In semi-log space.

⁽²⁾ Profile shape is determined in wavenumber domain.

⁽³⁾ Profile shape is determined from pre-computed x/L -dependent statistical distribution parameters.

⁽⁴⁾ An unfolded model is also provided.

⁽⁵⁾ Non-self-similar scaling is directly parameterized with \mathbf{M} in model functional form.

⁽⁶⁾ Magnitude dependence of profile shape is introduced by Box-Cox transformation.

The full probability distribution of fault displacement at an x/L location includes the probability of zero and non-zero displacements. Location-dependent FDMs provide the displacement probability distributions for non-zero displacements. The probability of zero displacement is handled separately. Zero aggregate displacement occurs when there is a gap in the surface rupture without any principal or distributed ruptures (i.e., where $D_{agg} = 0$), and zero principal displacement occurs when there are no principal ruptures at the location (i.e., $D_{sp} = 0$). Like other conditional probability of surface rupture models, the gap probability (i.e., $P(Gap)$, which is equivalent to $P(D_{agg} = 0)$) and zero principal displacement probability (i.e., $P(D_{sp} = 0)$) scale down the conditional probability of exceedance by $1 - P(Gap)$ and $1 - P(D_{sp} = 0)$, respectively.

There are two key differences between the LA23 FDM and other models. First, LA23 provide a model that is applicable to individual segments (x_{seg}/L_{seg}) and a “simplified FDM without segmentation” that uses the total surface rupture length (x/L). The model for individual segments can be used when fault segments can be identified *a priori*. Second, the LA23 simplified FDM is developed from their model for individual segments by treating the number, location, and length of fault segments as aleatory variability. Gaps in surface rupture (i.e., where $D_{agg} = 0$) and locations of no principal displacement (i.e., $D_{sp} = 0$) are removed from the simplified FDM and handled through separate models for the probability of zero displacement ($P(Gap)$ and $P(D_{sp} = 0)$, respectively). As a result, artifacts of segmentation, such as median displacement amplitude tapering at segment endpoints (e.g., Figure 3.1a), are separated from the probability of zero displacement. In all other location-dependent FDMs, artifacts of segmentation are captured in the within-event variability of the probability of non-zero displacement.

The LA23 model provides simplified FDMs for aggregate and sum-of-principal displacement. When the simplified FDMs are used, the full distribution of displacements (i.e., zero and non-zero displacements) should be evaluated to correctly capture the effects of segmentation based on the assumptions in their modeling framework. Specifically, the simplified FDM for sum-of-principal displacement should be scaled by both the $P(Gap)$ and the $P(D_{sp} = 0)$. However, the simplified FDM for aggregate displacement only needs to be scaled by their $P(Gap)$ model because zero displacements on principal ruptures are inherently captured in the aggregate value.

Importantly, the $P(Gap)$ and the $P(D_{sp} = 0)$ models developed by LA23 are not compatible with other FDMs in most cases because these are coupled with their segmentation model, which forms the basis of their overall FDM. Specifically, the LA23 FDMs were developed using data from individual rupture segments, and the within-event variability in their model is therefore based on segment data. In the simplified FDMs, a separate additional aleatory variability model is used to capture the number, lengths, and locations of segments, along with adjustments to the median displacement. Other location-dependent FDMs were developed using data from the full rupture length, and segmentation effects are implicitly captured in the within-event aleatory variability in those models.

4 Data Set Selection and Model Applicability

This chapter summarizes the data sets used in the development of each FDM. Specifically, we summarize the number of events, number of measurements, and magnitude ranges for the models evaluated in this report (Table 1.1). Guidance on model applicability is provided at the end of this chapter.

4.1 DATA SET SELECTION

All four new FDMs used the FDHI Database (Sarmiento et al., 2021). The empirical database was developed in collaboration with earthquake geologists, model developers, engineering community end-users, and project sponsors through the FDHI Project. The primary goal of the database was to support the development of new FDMs by systematically collecting, reviewing, and organizing relevant data in a database. The database contains rupture traces and fault displacement measurements from 75 global historical surface-rupturing earthquakes. The earthquakes are from shallow crustal tectonic environments and include all styles of faulting.

The FDHI model development teams selected subsets of the FDHI database based on data selection criteria for their model. The specific criteria and justification for the excluded data are described in the respective model reports. Generally, model teams excluded events based on style of faulting (e.g., MEA24 and CEA25) or insufficient spatial distribution or number of displacement measurements. Individual measurements with low-quality flags were typically excluded, and some model developers selected one measurement data set when alternative data sets were available for the same event (e.g., the Hector Mine earthquake).

The x/L scaling component of the models use empirical displacement profiles (i.e., displacement amplitude as a function of normalized location along the rupture; Figure 3.1). The reference lines used to measure the normalized location can be based on manual or algorithmic interpretation of the rupture and/or displacement data. Manual efforts usually consist of a geologist determining the nominal rupture trace and projecting displacement measurements onto the trace. This approach can be subjective, especially when multiple (sub)parallel ruptures occur. Lavrentiadis et al. (2024) and Thomas et al. (2024) recently developed automated methods to remove or minimize subjectivity. The Event Coordinate System (ECS) algorithm by Lavrentiadis

et al. (2024) generates a reference line based on the spatial distribution of principal surface rupture traces and principal displacement measurement amplitudes. The Thomas et al. (2024) algorithm uses a least-cost path (LCP) analysis of the spatial distribution of surface rupture traces to create the reference line. Both methods use the second generalized coordinate system (GC2) by Spudich and Chiou (2015) to transform the event data into an along-strike dimension based on the reference line. The ECS coordinates are included in the FDHI Database. The Thomas et al. (2024) coordinates are published separately because they were finalized after the FDHI Database was released.

Table 4.1 summarizes the data sets used for x/L scaling in the new and previously published FDMs evaluated in this report. The new FDMs exclusively used the displacement measurements in the FDHI Database for x/L scaling. The previously published models used various data sets. The CEA25 model (which only applies to strike-slip style of faulting) used the LCP-based reference line for the along-strike projection of displacements, whereas the other new models used the ECS. Preliminary sensitivity evaluations by G. Lavrentiadis (pers. comm.) and Chiou et al. (2023), as well as a more detailed comparison by Thomas et al. (2024), found that while the surface rupture lengths derived from the ECS and LCP reference lines were similar for all strike-slip events, the LCP reference lines are systematically longer because they are not as smooth; however, the impact should not be significant in a PFDHA framework when ruptures are floated along a fault system.

The data sets used for magnitude scaling are shown in Table 4.2. Three of the new FDMs (KEA24, CEA25, and LA23) exclusively used the data from the FDHI Database for magnitude scaling. The MEA24 model predicts normalized displacements and therefore captures magnitude scaling using AD or MD . MEA24 compiled a separate data set of these metrics for reverse events using the FDHI Database and other sources. Similarly, the MR11 and YEA03 models also predict normalized displacements and thus used different data sets for magnitude and x/L scaling. The data sets for magnitude scaling are larger than those for x/L scaling in the normalized displacement models.

Table 4.1. Summary of data sets used in models for x/L scaling.

| Model | Reference Line Basis | Style of Faulting ⁽¹⁾ | N Events | Event M Range | N Measurements | Data Set |
|-------|----------------------|----------------------------------|----------|---------------|----------------|----------------------------------------------|
| LA23 | SCS ⁽²⁾ | SS | 34 | 5.0 – 7.9 | 9109 | FDHI |
| | | RV/RVO | 25 | 4.9 – 8.02 | 2769 | |
| | | NM/NMO | 15 | 6.2 – 7.76 | 8044 | |
| MEA24 | ECS | RV/RVO | 21 | 5.03 – 8.02 | 1038 | FDHI |
| KEA24 | ECS | SS | 34 | 5.2 – 7.9 | 5446 | FDHI |
| | | RV/RVO | 25 | 4.9 – 8.02 | 2123 | |
| | | NM/NMO | 14 | 6.2 – 7.76 | 3309 | |
| CEA25 | LCP | SS | 29 | 6.0 – 7.9 | 3309 | FDHI |
| YEA03 | Manual | NM/NMO | 11 | 6.22 – 7.29 | Not Reported | McCalpin and Slemmons (1998) |
| PEA11 | Manual | SS | 21 | 6.3 – 7.9 | 1666 | Wesnousky (2008) subset, plus 9 PEA11 events |
| MR11 | Manual | RV/RVO | 9 | 5.4 – 7.9 | Not Reported | Wesnousky (2008) subset, plus 1 MR11 event |

⁽¹⁾ SS = Strike-slip; RV = Reverse; RVO = Reverse-oblique; NM = Normal; NMO = Normal-oblique.

⁽²⁾ The Segment Coordinate System (SCS) uses the ECS methodology to develop reference lines for individual segments.

Table 4.2. Summary of data sets used in models for magnitude scaling.

| Model | Style of Faulting ⁽¹⁾ | N Events | Event M Range | Data Set |
|-------|----------------------------------|--------------------|------------------------------------|-------------------------------------------------|
| LA23 | SS | 34 | 5.0 – 7.9 | FDHI |
| | RV/RVO | 25 | 4.9 – 8.02 | |
| | NM/NMO | 15 | 6.2 – 7.76 | |
| MEA24 | RV/RVO | 29 (AD) 42 (MD) | 4.7 – 8.02 (MD) 4.7 – 8.02 (MD) | MEA24 ⁽²⁾ |
| KEA24 | SS | 34 | 5.2 – 7.9 | FDHI |
| | RV/RVO | 25 | 4.9 – 8.02 | |
| | NM/NMO | 14 | 6.2 – 7.76 | |
| CEA25 | SS | 29 | 6.0 – 7.9 | FDHI |
| YEA03 | NM/NMO | 56 | 5.6 – 8.1 | Wells and Coppersmith (1994), AD for all styles |
| PEA11 | SS | 21 | 6.3 – 7.9 | Wesnousky (2008) subset, plus 9 PEA11 events |
| MR11 | RV/RVO | 25 | 5.4 – 7.9 | MR11 MD |

⁽¹⁾ SS = Strike-slip; RV = Reverse; RVO = Reverse-oblique; NM = Normal; NMO = Normal-oblique.

⁽²⁾ Events statistics are based on “complete” subsets in MEA24.

4.2 MODEL APPLICABILITY

The applicability conditions for each model, as specified by the model developers, are listed in Table 4.3. The recommendations are generally based on the empirical data used to develop the model and the modelers' confidence in extrapolating beyond the data or limiting applicability where data are sparse. For example, the LA23 model developers note that the underlying model in their FDM is based on wavenumber spectrum analysis that provides a physical basis for magnitude scaling and enables extrapolation to smaller and larger magnitudes (Lavrentiadis and Abrahamson, 2019, 2023). The CEA25 model developers compared the magnitude scaling used in their model to *AD* data sets compiled by others and found the scaling was consistent for up to **M** 8.3 strike-slip earthquakes. The magnitude range for the PEA11 model is based on personal communication with the model developers. The recommended magnitude ranges for all other models are reported in the respective reference. All FDMs except KEA24 use a folded profile functional form, requiring the normalized location to be ≤ 0.5 .

Table 4.3. Recommended model applicability.

| Model | Style of Faulting ⁽¹⁾ | Magnitude | x/L |
|-------|----------------------------------|--------------------------|-------------------------|
| LA23 | All | 5.0 – 8.5 | [0, 0.5] |
| MEA24 | RV/RVO | 4.7 – 8.0 | [0, 0.5] |
| KEA24 | SS | 6.0 – 8.0 | [0, 1] ⁽²⁾ |
| | RV/RVO | 5.0 – 8.0 | |
| | NM/NMO | 6.0 – 8.0 | |
| CEA25 | SS | 6.0 – 8.3 | [0, 0.5] ⁽³⁾ |
| YEA03 | NM/NMO | 5.6 – 8.1 ⁽⁴⁾ | [0, 0.5] |
| PEA11 | SS | 6.0 – 8.0 | [0, 0.5] |
| MR11 | RV/RVO | 5.5 – 8.0 | [0, 0.5] |

⁽¹⁾ SS = Strike-slip; RV = Reverse; RVO = Reverse-oblique; NM = Normal; NMO = Normal-oblique.

⁽²⁾ Predicted profile is right-skewed (i.e., peak displacement occurs at $x/L \leq 0.5$); calculation for complimentary location ($1 - x/L$) should be equally-weighted in most cases because profile asymmetry is not known a priori.

⁽³⁾ An alternative right-skewed, unfolded [0,1] formulation is also provided.

⁽⁴⁾ Based on Wells and Coppersmith (1994) displacement – magnitude regression.

5 Model Comparisons

This chapter provides comparisons of the x/L scaling, magnitude scaling, and aleatory variability in the new and previously published FDMs.

Direct comparisons between the models are limited by the different definitions of displacement used among the models (Table 2.1). Methods to adjust for different participating ruptures (i.e., aggregate, sum-of-principal, and single principal) are not available. As discussed in Chapter 2.1, the data for the net component are incomplete, which prevents the use of *ad hoc* adjustments for displacement components. For example, the predicted vertical displacements from the MR11 and MEA24 models cannot simply be scaled using trigonometric ratios with an assumed fault dip to be compatible with models that predict net displacement because the net displacement data generally do not capture the fault-normal or dip-slip components in reverse earthquakes.

For models that have multiple formulations, the comparisons are limited to one or two alternatives for brevity. For example, only the results from the PEA11 $\ln(D)$ model for their elliptical functional form is shown. The YEA03 D/MD model based on the McCalpin and Slemmons (1998) data set is used. Only the MR11 D/AD Gamma distribution and D/MD (Beta distribution) model results are shown. The CEA25 results are for their preferred model (“Model7.nEMG”). The LA23 results are based on their “simplified FDM,” which is applicable to the full rupture (i.e., the segmented model x_{seg}/L_{seg} is not evaluated), and any adjustments for zero displacement are discussed separately for each comparison.

The normalized displacement models (YEA03, MR11, and MEA24) allow for any appropriate displacement – moment magnitude scaling relation. The following are used in the calculations herein:

- YEA03 D/AD : Wells and Coppersmith (1994) $\log(AD) - M$, all styles of faulting
- YEA03 D/MD : Wells and Coppersmith (1994) $\log(MD) - M$, all styles of faulting
- MR11 D/AD : Moss and Ross (2011), $\log(AD) - M$
- MR11 D/MD : Moss and Ross (2011), $\log(MD) - M$
- MEA24 D/AD : Moss et al. (2022) $\log(AD) - M$, “complete” subset
- MEA24 D/MD : Moss et al. (2022) $\log(MD) - M$, “complete” subset

Results for the normalized models include total aleatory variability (i.e., the aleatory variability on the AD or MD is convolved with the aleatory variability on the D/AD or D/MD).

Our implementation of the MEA24 FDMs has two key assumptions. First, we truncate the aleatory variability for the D/MD distribution at 1.0. MEA24 models the aleatory variability on D/MD using a Gamma distribution, which is defined on the interval $[0, \infty)$. As a result, it is possible to compute or sample a D/MD value greater than 1, although such values are not physically valid. (See Supplement D in Sarmiento et al., 2025 for further discussion.) Second, the x/L scaling used herein for the MEA24 FDMs is based on piecewise linear interpolation of the pre-computed statistical distribution parameters tabulated in Moss et al. (2024). The interpolation method is preferred by the MEA24 developers over the regressions in Moss et al. (2022) (R. Moss, pers. comm.).

The KEA24 calculations use the mean model coefficients with equal weighting on right- and left-skewed profiles (i.e., equal weighting with the complimentary location $1 - x/L$) to produce symmetrical profiles.

5.1 X/L SCALING

The x/L scaling controls how the predicted displacement varies along the rupture length. The functional forms of the x/L scaling components in FDMs determine the shape of the median displacement profile, including the intensity of displacement amplitude tapering at the ends of ruptures. Empirical observations suggest displacements are generally lower at rupture endpoints and increase toward the middle of the rupture (e.g., Hemphill-Haley and Weldon, 1999; Biasi and Weldon, 2006; Wesnousky, 2008).

Equal-area mean displacement profiles predicted by each model are shown on Figure 5.1 for each style of faulting. We use mean profiles instead of median because these more similar to empirical displacement profiles, which inherently contain within- and between-event variability. Because the LA23 and KEA24 FDMs have non-self-similar scaling, profiles are shown for M 6 and 8. The LA23 FDMs for aggregate and sum-of-principal have the same x/L scaling, and the probability of zero displacement is not included.

The profiles are area-normalized to remove the effects of magnitude scaling and provide a more direct comparison of the profile shapes and end-of-rupture tapering effects. The area-normalized profiles $f(x)$ are computed using the following equation:

$$f(x) = \frac{\bar{D}(x)}{\int_0^1 \bar{D}(x) dx} \quad (5.1)$$

where $x = x/L$ is used for convenience and $\bar{D}(x)$ is the predicted mean displacement at a given x/L . The integral was approximated using numerical integration with the trapezoidal rule and a step size of 0.01 units on Figure 5.1.

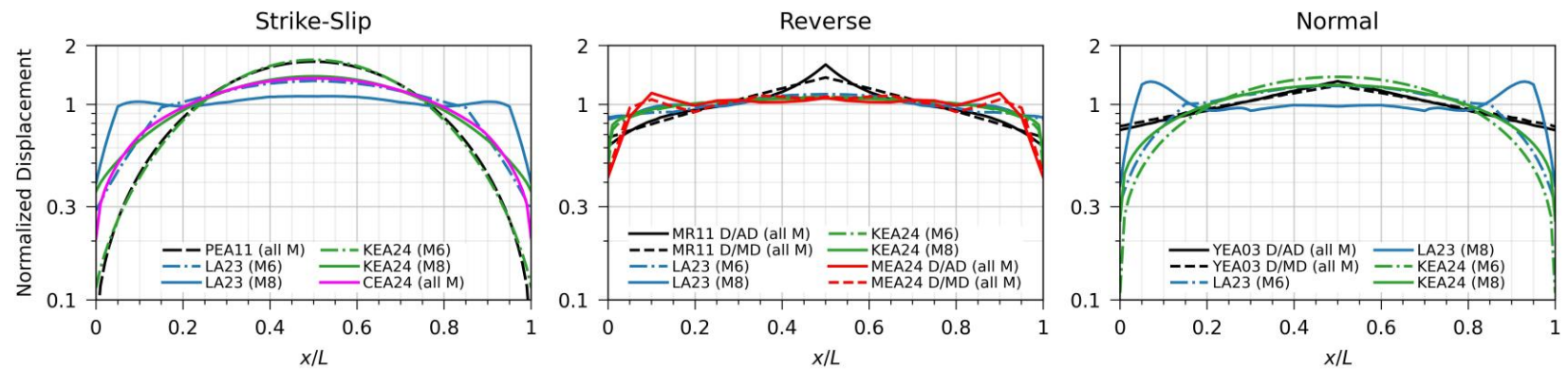


Figure 5.1. Comparison of x/L scaling using equal-area mean profiles.

While details of the comparisons between the profiles on Figure 5.1, some general observations can be made. Importantly, the x/L scaling varies significantly with style of faulting. For example, most new and previously published models predict highly elliptical shapes with steep end-of-rupture tapering for strike-slip and normal events. Conversely, the x/L scaling for reverse events is flatter. In general, the x/L scaling for the D/AD and D/MD alternatives for a given model are very similar. The x/L scaling in the LA23 M 8 profiles produces large displacements near the rupture endpoints (particularly for strike-slip and normal events) due to effects from their segmentation model.

The x/L scaling for the new and previously published FDMs are generally similar for strike-slip faulting. The KEA24 profile is nearly identical to PEA11 for M 6 and very similar to CEA25 for M 8. The KEA24 and CEA25 profiles are both elliptical, but the tapering is stronger for KEA24 at smaller magnitudes because dependence on displacement amplitude (and therefore earthquake magnitude) is introduced by the Box-Cox transform. In the LA23 model, the x/L scaling for strike-slip events is very similar to CEA25 for M 6; as magnitude increases, the LA23 profiles flatten, peak displacements migrate toward the rupture endpoints, and the end-of rupture tapering steepens and occurs over shorter distances.

For reverse events, the x/L scaling in the new FDHI FDMs is very similar, producing nearly flat profiles. In contrast, the MR11 models produced larger displacements at the rupture midpoint. Of the new reverse faulting models, LA23 has the weakest end-of-rupture-tapering. The magnitude dependence on the x/L scaling for reverse faults in LA23 and KEA24 is small.

Finally, the x/L scaling in the FDHI normal faulting models is generally quite different from YEA03. The KEA24 normal faulting profiles are elliptical, and the scaling is less sensitive to magnitude than in their strike-slip model. The scaling for M 6 normal events is reasonably similar for LA23 and KEA24, but the effects of segmentation in the LA23 model produce larger displacements near the rupture endpoints, steep tapering at the rupture ends, and flat scaling in the middle of the rupture for M 8.

5.2 AVERAGE DISPLACEMENT

We use average displacement (AD) to demonstrate the magnitude scaling component of the models because allows for comparisons between FDMs with different functional forms and modeling approaches. For example, x/L -independent models that predict AD are typically developed from regressions of earthquake size on empirical AD datasets (e.g., WC94, MR11, MEA24). For x/L -dependent models (e.g., PEA11, LA23, KEA24, CEA25), the AD can be calculated by integrating the predicted mean displacement profile:

$$AD(\mathbf{M}) = \int_0^1 \bar{D}(\mathbf{M}, x) dx \quad (5.2)$$

where $x = x/L$ is used for convenience, and $\bar{D}(\mathbf{M}, x)$ is the predicted mean displacement for a given moment magnitude \mathbf{M} at a given along-strike location x/L . The predicted mean displacement is computed by integrating over the aleatory variability (i.e., the probability density function, PDF):

$$\bar{D} = \int_0^{\infty} D f_{pdf}(D|\mathbf{M}, x) dD \quad (5.3)$$

where $f_{pdf}(D|\mathbf{M}, x)$ is the PDF of the model prediction for a given magnitude \mathbf{M} and location x/L . The PDF in Equation 5.3 should be based on within-event variability only because this controls the median AD , whereas the between-event variability controls the aleatory variability on AD .

The LA23 and CEA25 models provide formulations for AD based on Equation 5.2. We use their formulations to calculate the AD predictions on Figure 5.2. For the LA23 model, the probability of zero displacement is not considered for consistency with common magnitude scaling relations, such as WC94. The CEA25 model uses self-similar scaling, so the x term in Equation 5.2 can be integrated out to develop a simple magnitude scaling relation for AD . LA23 developed a parametric model for AD from a synthetic dataset generated by evaluating Equation 5.2. The KEA24 model recommends computing AD per Equation 5.2. The WC94, MR11, and MEA24 models use a different approach, providing empirical scaling relations for AD based magnitude. While PEA11 uses the WC94 strike-slip magnitude scaling relation for AD in their $\ln(D/AD)$ FDMs, they do not derive separate formulations for AD for their $\ln(D)$ FDMs, so we compute AD using Equation 5.2 for their elliptical $\ln(D)$ model. However, these results include between-event variability because the total aleatory variability is not separated into between- and within-event components in their $\ln(D)$ models (Table 3.3). By including the between-event variability, the PEA11 results on Figure 5.2 are analogous to the mean prediction for AD , whereas the results for the other models are analogous to the median prediction for AD .

Figure 5.2 shows how the AD scales with magnitude for each FDM. A key feature of most of the FDHI FDMs is the use of nonlinear magnitude scaling (Table 3.3; Figure 5.2). The scaling is linear in semi-log space for all previously published models. The FDHI models by KEA24 and CEA25 use bilinear magnitude scaling with breakpoints at $\mathbf{M} 7.0$ and 7.1 , respectively. The LA23 uses trilinear scaling with style-independent scaling above the upper breakpoint at $\mathbf{M} 7$, whereas the lower breakpoint and scaling vary with style. The scaling for reverse faulting is linear in MEA24 and approaches linear in LA23 and KEA24.

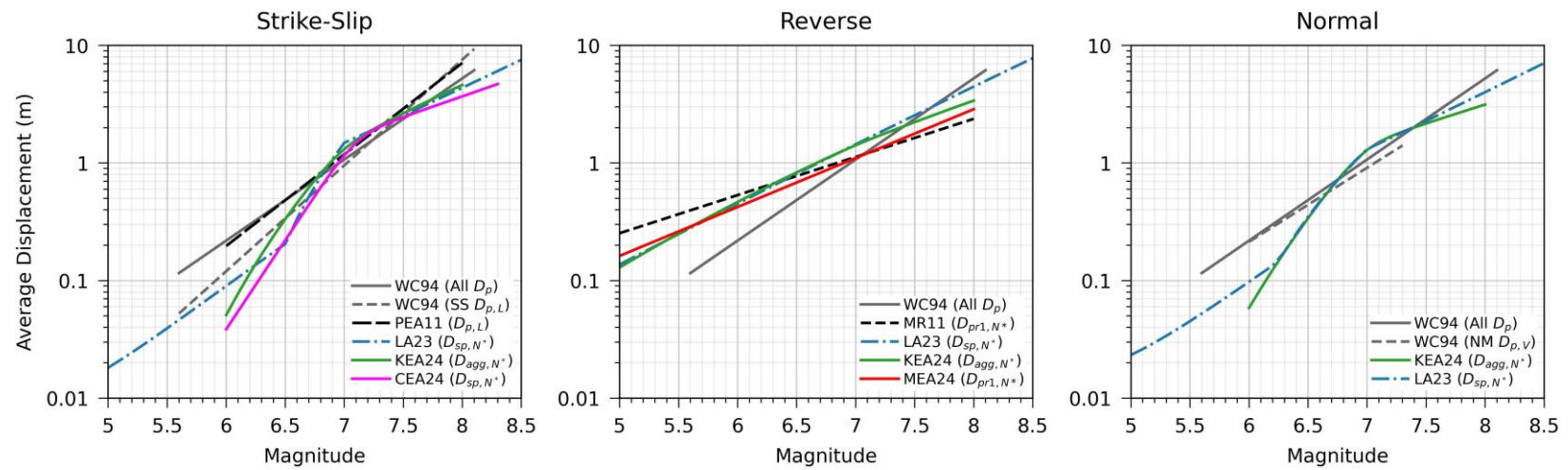


Figure 5.2. Comparison of magnitude scaling for average displacement. Results are shown for the recommended magnitude range of each model without extrapolation. Model displacement definitions are identified in parentheses per Table 2.1.

Strike-slip events have the steepest scaling in FDMs, and reverse events have the flattest scaling. The bilinear and trilinear scaling in the FDHI models for strike-slip and normal faulting produce significantly lower average displacements for small and large magnitudes, compared to previously published models; however, the predictions are higher near the upper breakpoints (i.e., $M \sim 7$). For reverse faulting, the scaling in the FDHI models is steeper than in MR11, which leads to lower AD predictions at smaller magnitudes and larger predictions at larger magnitudes. Different datasets, modeling approaches, and definitions of displacement in the MEA24 model lead to differences from the other FDHI AD models for reverse faulting.

While the AD predictions in the FDHI models are generally lower than in previously published models, $M \sim 7$ is an exception. The FDHI strike-slip models range from 22% higher than WC94 (CEA25) to 37% higher (KEA24). For reverse faulting, the predictions from LA23 and KEA24 are 27% higher than MR11; however, the predicted AD for $M 7$ in the MEA24 model is nearly identical to the MR11 prediction. The LA23 and KEA24 models for normal faulting are almost identical between $M 6.3$ and 7.4 and are 42% higher than WC94. The larger predictions for $M 7 AD$ are generally due to different definitions of displacement used in the models (i.e., net displacement versus lateral or vertical displacement and single principal versus sum-of-principal or aggregate), and the use of nonlinear magnitude scaling, which provides more flexibility to better capture the data.

At larger magnitudes, the AD in the FDHI models is lower for strike-slip and normal faulting and higher for reverse, relative to the previously published models. For example, the AD for $M 8$ in the FDHI models is lower by a factor of about 2 for strike-slip and about 1.3 to 1.7 for normal faulting (relative to WC94 strike-slip and all styles, respectively). For reverse faulting, the FDHI models are 21% to 88% higher (MEA24 and LA23 sum-of-principal, respectively), compared to MR11.

5.3 MAXIMUM DISPLACEMENT

Several x/L -independent FDMs provide predictions for maximum displacement (MD) developed from regressions of earthquake size on empirical MD datasets (e.g., WC94, MR11, MEA24). For x/L -dependent FDMs, the MD is not readily derived from the model predictions like AD (see Chapter 5.2 discussion). Instead, the MD is implicitly somewhere in the upper tail of the displacement probability distribution, and it can occur at any x/L location.

Magnitude scaling relations for MD are provided by WC94, MR11, and MEA24. The KEA24, CEA25, and PEA11 FDMs do not provide predictions for MD . LA23 used numerical simulation to develop a parametric model for MD that is consistent with their overall FDM. We use the percentiles (i.e., aleatory quantiles) corresponding to the LA23 median prediction for MD to facilitate a rough approximation of the MD “implied” in the KEA24, CEA25, and PEA11 FDMs

to allow for comparisons with models that predict MD . The LA23 MD model is conditioned on the median (transformed) displacement at $x/L = 0.25$ as an arbitrary reference. The probability of zero displacement is not included. The LA23 FDMs use a normal distribution to model the aleatory variability on (transformed) displacement, so Figure 5.3 shows the number of standard deviations (ε) on the left axis and the corresponding percentiles on the right axis for the median MD at $x/L = 0.25$ as a function of magnitude and style of faulting. The total aleatory variability for their aggregate FDM for individual segments was used. We used these magnitude–percentile pairs to calculate the predicted displacements at $x/L = 0.25$ in the KEA24, CEA25, and PEA11 FDMs, using the total aleatory variability in those models.

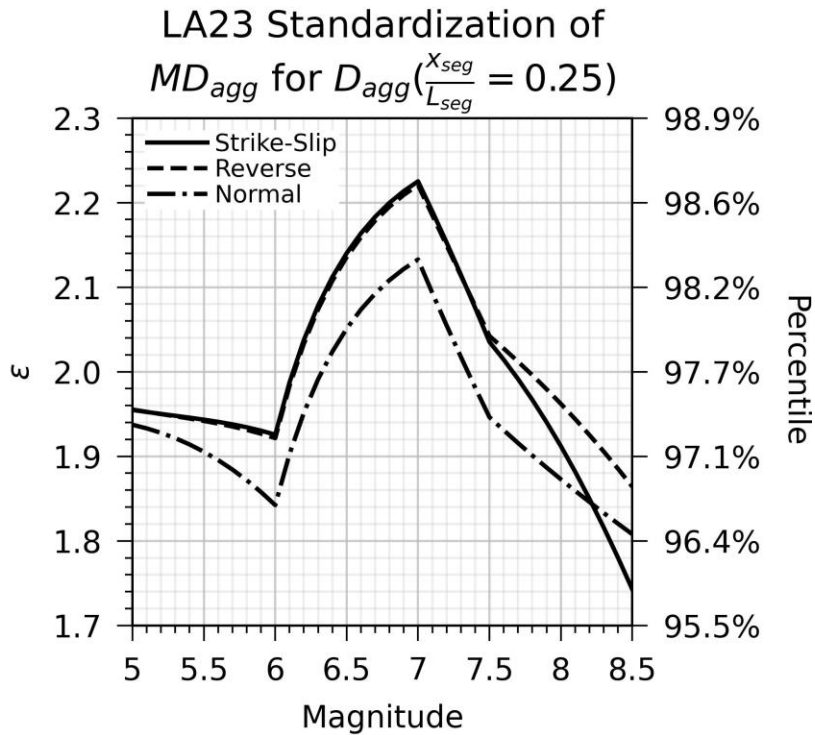


Figure 5.3. Number of standard deviations (ε) corresponding to the median prediction for maximum displacement in the LA23 FDM for aggregate displacement. Right axis shows corresponding percentile rank (i.e., cumulative probability) for the number of standard deviations on the left axis for a standard normal distribution.

Figure 5.4 shows how the predicted or implied MD scales with magnitude for each model. Empirical MD data sets are also shown on Figure 5.4 to demonstrate how the median MD predictions and estimations compare with historical observations. For reverse events, we show the data set used by MEA24 to develop their regression model. They supplemented the FDHI Database

with data from additional events. The aggregate displacement data set developed by LA23 (using data from the FDHI Database) is shown; however, we note that the LA23 *MD* model is not developed by regressing magnitude against these data, but rather a parametric fit of maximum displacements computed from their underlying FDM. Reported maximum displacements from other large, shallow crustal earthquakes in continental crust, such as the 1931 M 7.92 Kehetuohai, China and 1855 M 8.2 Wairarapa, New Zealand strike-slip earthquakes are also shown (Wells and Coppersmith, 1994; Manighetti et al., 2020).

The magnitude scaling for *MD* in the new models is flatter than in the previously published models for most magnitudes due to nonlinear magnitude scaling in most of the new models (Table 3; Figure 5.4). The median maximum displacement estimates in the LA23, KEA24, and CEA25 models tightly envelope the empirical data, indicating the statistical distributions and magnitude scaling used in these models are in reasonable agreement with the empirical data. Importantly, the estimates for large magnitudes ($M > 7.5$) are in good agreement with the data, which supports the use of these models in PFDHA for low probabilities of exceedance that correspond to long return periods.

For reverse faulting, the MEA24 median *MD* predictions are lower than LA23 and KEA24 results due to the use of different data sets, definitions of displacement, and modeling approaches. The MEA24 *MD* model was developed by regressing magnitude on a separate collection of empirical observations of maximum vertical displacement from individual principal ruptures; however, the LA23 *MD* model is for net aggregate displacement and is based on their underlying FDM that was developed using the FDHI Database. The KEA24 results represent a *MD* estimate for net aggregate displacement based on the upper tail predictions from their model.

The LA23 percentiles for the median *MD* are used here to provide a rough approximation of the *MD* implied in the PEA11, KEA24, and CEA25 models as a first-order validation of the shape of the upper tails of these models with respect to empirical data. This approach is not a rigorous assessment and imposes aspects of the LA23 model onto the other models that may not be applicable. However, it is a useful process for estimating magnitude- and style-specific percentiles that roughly correspond to the median *MD* to understand how the models extrapolate to longer return periods in PFDHA.

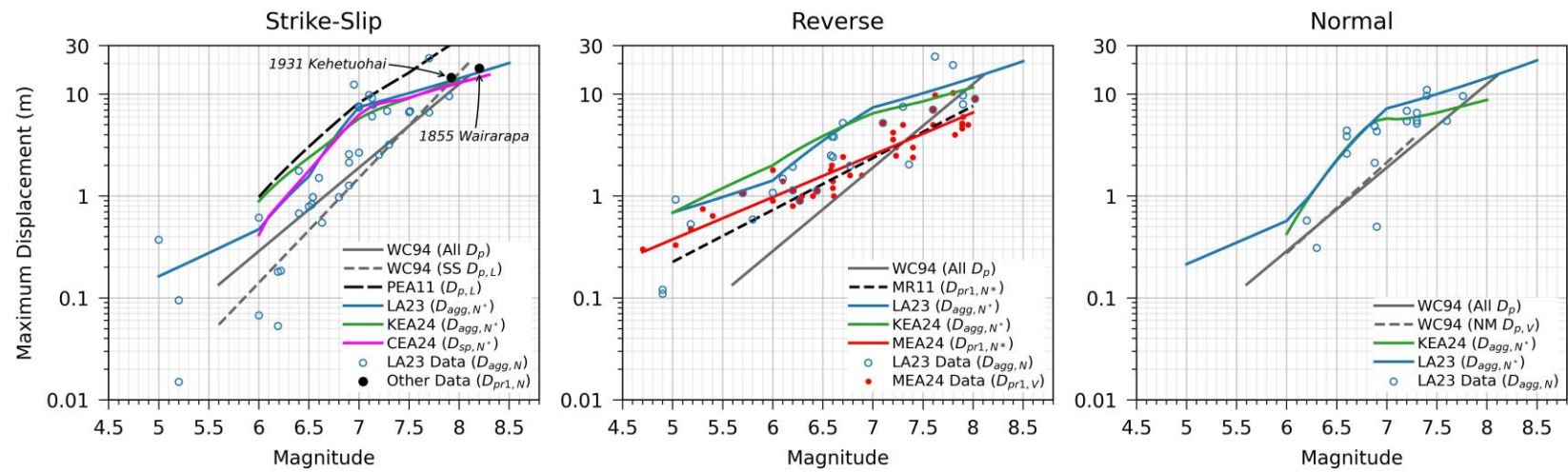


Figure 5.4. Comparison of magnitude scaling using the median prediction for maximum displacement. Results for models denoted with asterisks (PEA11, KEA24, and CEA25) are estimates; see text for discussion on estimation methodology. Results are shown for the recommended magnitude range of each model without extrapolation. Displacement definitions are identified in parentheses per Table 2.1. All data are for non-oceanic shallow crustal earthquakes.

5.4 MEDIAN PREDICTIONS

A series of plots for a broad range of style– M – x/L scenarios is presented in the discussion on aleatory variability in Chapter 5.5.1 (Figures 5.5 through 5.19). The plots include predictions for the median (50th percentile). While some general observations can be made with respect to the median predictions, the details of the comparisons vary significantly across the scenarios, and direct comparisons are complicated by the different definitions of displacement used in among the models (Table 2.1). Nonetheless, we note the following trends:

- The median predictions among the new *strike-slip* models are within a factor of about 1.5 to 2 for almost all magnitudes and locations. The differences are largest where data are sparse, which is for M 6 and at the rupture endpoints for all magnitudes.
- The median predictions among the new *reverse* models are within a factor of about 1.9 for all cases except the rupture endpoints, where the MEA24 median predictions range from about 4.5 to 6 times smaller than the other new models.
- The median predictions among the new *normal* models are within a factor of about 2 for almost all magnitudes and locations. The exception is M 6 (for which data are sparse), where the KEA24 model is about 3 to 6 times smaller than LA23 (aggregate), depending on the location.
- The median predictions in the new *strike-slip* models are generally similar to the PEA11 median predictions, with a few exceptions. For moderate and large magnitudes ($M > 6.5$), the median predictions at the rupture endpoints ($x/L = 0$) in the new models are significantly larger (up to 10x). At the rupture midpoint ($x/L = 0.5$), the median predictions are up to 30% less for M 8.0.
- The median predictions in the new *reverse* models are within a factor of about 2 of the range of the MR11 D/AD and D/MD predictions in most cases, with the exception of the rupture endpoints ($x/L = 0$) for smaller magnitudes, where the new model predictions are up to 4x smaller. The median predictions for M 8.0 at the rupture midpoint ($x/L = 0.5$) in the new models range from about 25% to 60% smaller than in the MR11 D/MD model.
- The median predictions in the new *normal* models are generally similar to the range of the YEA03 D/AD and D/MD predictions, with a few exceptions. At the rupture endpoints ($x/L = 0$), the median predictions in the new models for M 6 are up to 30 times smaller, and up to 4 times smaller at larger magnitudes. For larger magnitudes at the rupture midpoint ($x/L = 0.5$), the median predictions in the new models are reduced by up to 50%.

5.5 ALEATORY VARIABILITY

The aleatory variability is defined through the statistical distribution used in each FDM. As discussed in Chapter 3 and summarized in Table 3.2, the aleatory variability is partitioned into between- and within-event components in most models. The aleatory variability comparisons below focus on x/L -dependent FDMs (Table 3.1). In other words, we do not evaluate the variability on models that predict *AD* or *MD*.

Direct comparisons of the aleatory variability between FDMs are not straightforward because different statistical distributions and data transformations are used among the models (Table 3.2). While multiple FDMs use normal distributions (e.g., PEA11, LA23, KEA24), these models also use different data transformations, so the standard deviations are in different units; although the coefficient of variation could be used to standardize the variability in these models, statistical measures like standard deviation or coefficient of variation are not meaningful for skewed distributions (e.g., Gamma or nEMG). Instead, the aleatory variability is best compared using probability functions or dot charts for specific percentiles.

We present cumulative distribution functions (CDFs) for a set of style- $M-x/L$ scenarios, along with dot charts for various percentiles, to compare the shape and spread of the aleatory variability among the models. Probability of exceedance curves are also provided to demonstrate the impact of the aleatory variability modeling components in hazard space.

5.5.1 Cumulative Distributions and Percentiles

The cumulative displacement probability (CDF) curves compare the shape and variability over the full range of the model predictions, while the dot plots provide a percentile-based measure of the relative size of the aleatory variability among the models. A series of plots on Figures 5.5 through 5.9 show CDF curves (top panel) and percentile dot plots (bottom panel) for models applicable to strike-slip faults for magnitudes 6.0, 6.8, 7.2, 7.7, and 8.0, respectively. Three x/L locations are evaluated on each plot (0, 0.25, and 0.5), and the 5th, 16th, 50th (median), 84th, and 95th percentile predictions are shown. Similar figures for reverse faulting (Figures 5.10 through 5.14) and normal faulting (Figures 5.15 through 5.19) are also provided. For the LA23 results, the probability of zero displacement is not included.

Although the details of the comparisons vary significantly across the scenarios, some general observations can be made for the *strike-slip* models (Figures 5.5 through 5.9), disregarding effects of the different definitions of displacement used in among the models:

- The 95th percentile predictions in the new models are generally smaller than in the PEA11 model. Exceptions include the rupture endpoints ($x/L = 0$), where the new model predictions are significantly larger (up to 9x) and, importantly, at larger magnitudes, where

the new model predictions are significantly smaller. For example, the 95th percentile prediction for M 8 at the rupture midpoint in the PEA11 model is 40 m, but it is only 15 m in KEA24.

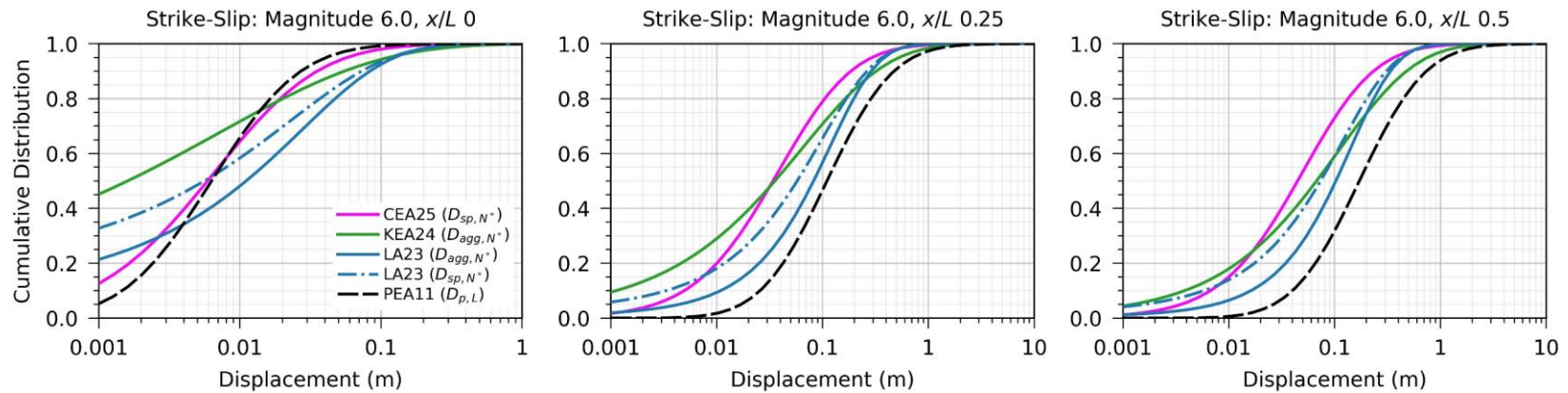
- The 95th percentile predictions among the new models are within a factor of 2.7 for all cases. The predictions are within a factor of 1.1 to 1.2 for moderate and large magnitudes ($M > 6.5$) at locations other than the rupture endpoint.
- The 5th percentile predictions among the new models are within a factor of about 4.5 for most cases. The heavy left tail in the new models leads to 5th percentile predictions that are less than 0.01 m for small magnitudes.

The model predictions for *reverse* faulting are more similar to each other, with the following general observations (Figures 5.10 through 5.14), again disregarding effects of the different definitions of displacement used in among the models:

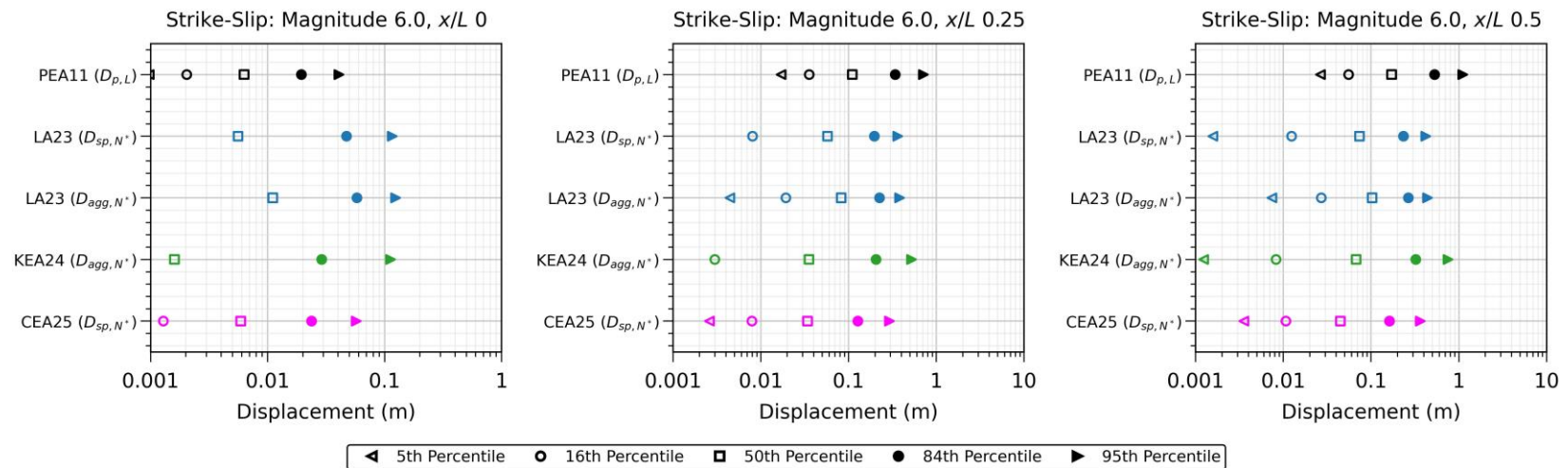
- The 95th percentile predictions in the new models are within a factor of about 2.5 of the range of the MR11 D/AD and D/MD predictions in most cases. The 95th percentile MEA24 predictions are less than MR11 in most cases.
- The 95th percentile predictions among the new models are within a factor of 2 for almost all cases. The exception is the rupture endpoint for moderate and large magnitudes ($M > 6.5$), where the MEA24 95th percentile predictions are roughly 50% to 75% other new models.
- The 5th percentile predictions among the new models are within a factor of about 2.5 for most cases; the exception is the MEA24 D/MD model, for which the 5th percentile rupture endpoint predictions are more than 10 times smaller than the other new models.

Finally, the model predictions for *normal* faulting also vary significantly across the scenarios, with the following general observations (Figures 5.15 through 5.19), again disregarding effects of the different definitions of displacement used in among the models:

- The 95th percentile predictions in the new models are smaller than YEA03 D/AD and D/MD predictions in almost all cases. At larger magnitudes, the new model predictions are significantly smaller. For example, the 95th percentile prediction for M 8 at the rupture midpoint in the YEA03 D/AD model is 37 m, but it is only 9 m in KEA24.
- The 95th percentile predictions among the new models are within a factor of 1.2 to 1.5 for almost all cases except the rupture endpoints, where the KEA24 predictions are generally about 3 times smaller than the LA23 (aggregate) predictions.
- The 5th percentile predictions among the new models are within a factor of about 5 for most cases. The heavy left tail in the new models leads to 5th percentile predictions that are less than 0.01 m for small magnitudes.

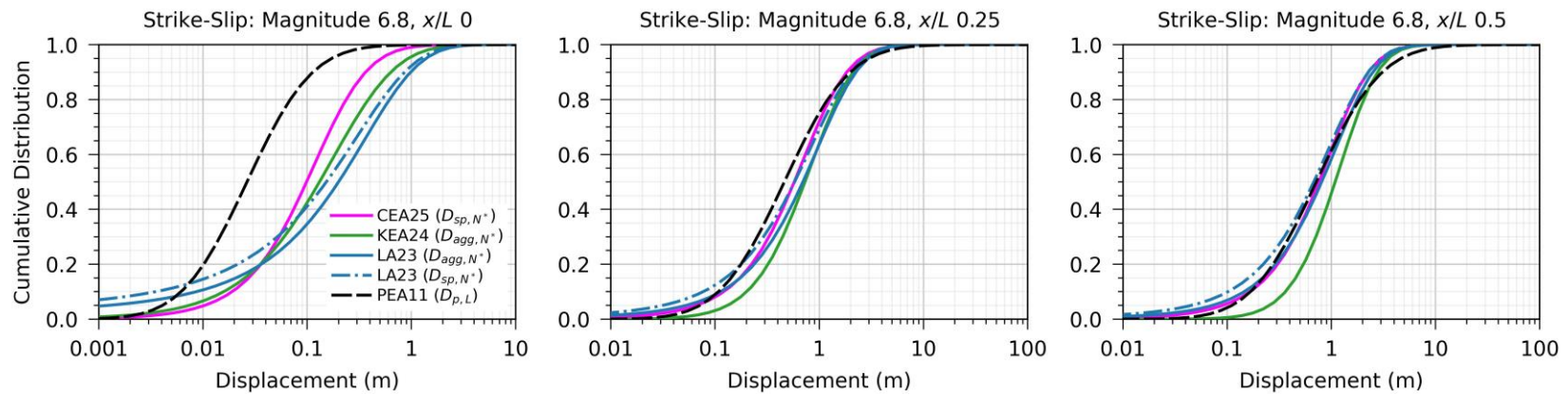


(a) Cumulative displacement probability curves.

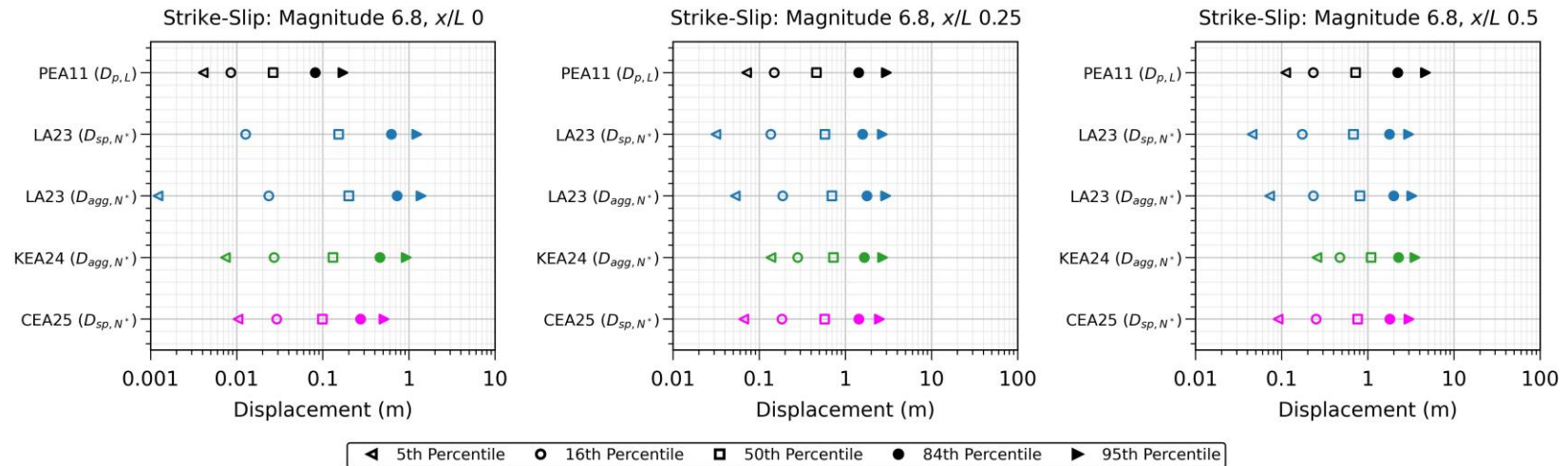


(b) Percentile displacement plots.

Figure 5.5. Comparison of aleatory variability for M 6.0 strike-slip events. Displacement definitions in parentheses are explained in Table 2.1.

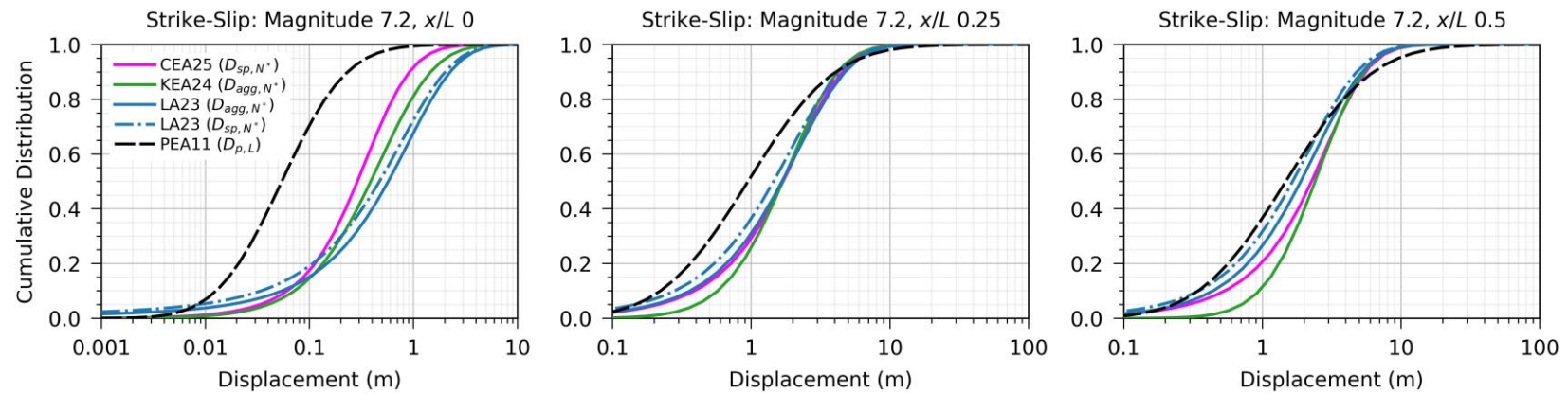


(a) Cumulative displacement probability curves.

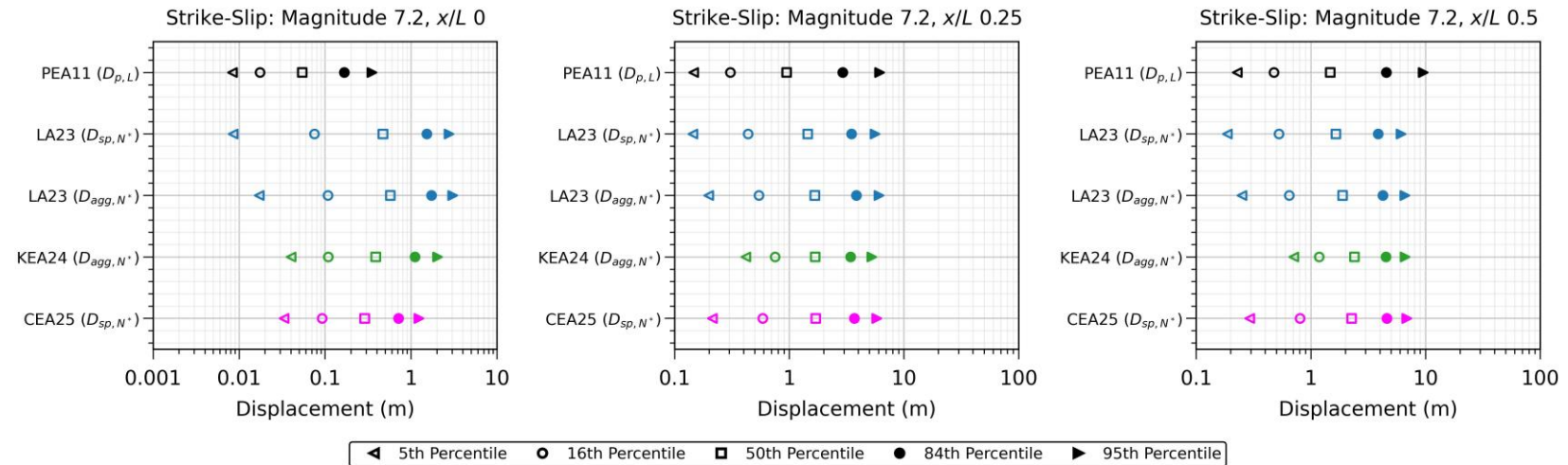


(b) Percentile displacement plots.

Figure 5.6. Comparison of aleatory variability for M 6.8 strike-slip events. Displacement definitions in parentheses are explained in Table 2.1.

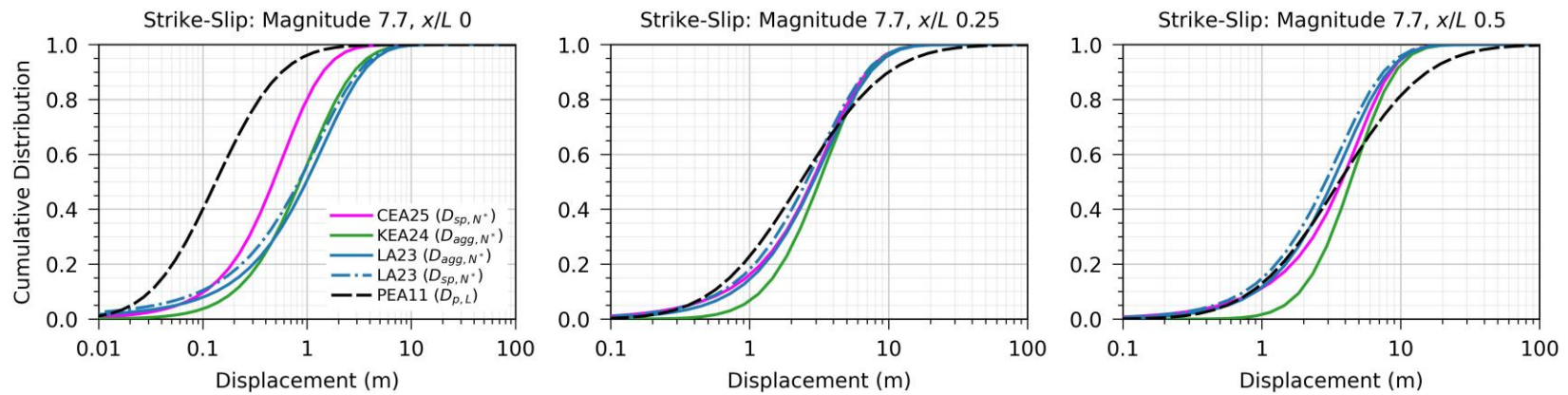


(a) Cumulative displacement probability curves.

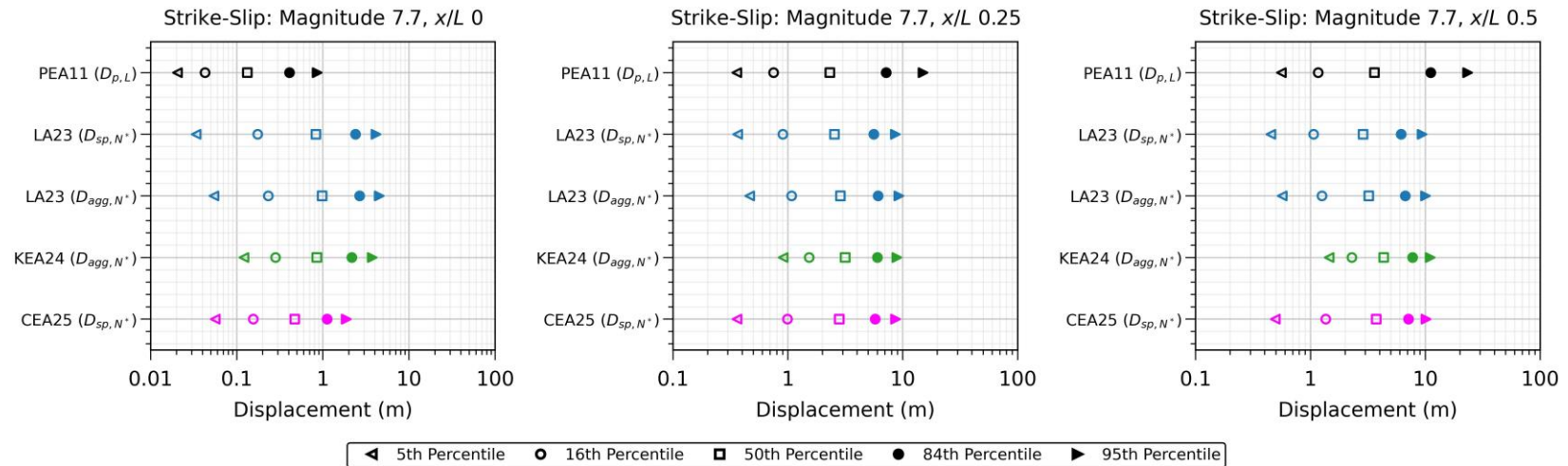


(b) Percentile displacement plots.

Figure 5.7. Comparison of aleatory variability for M 7.2 strike-slip events. Displacement definitions in parentheses are explained in Table 2.1.

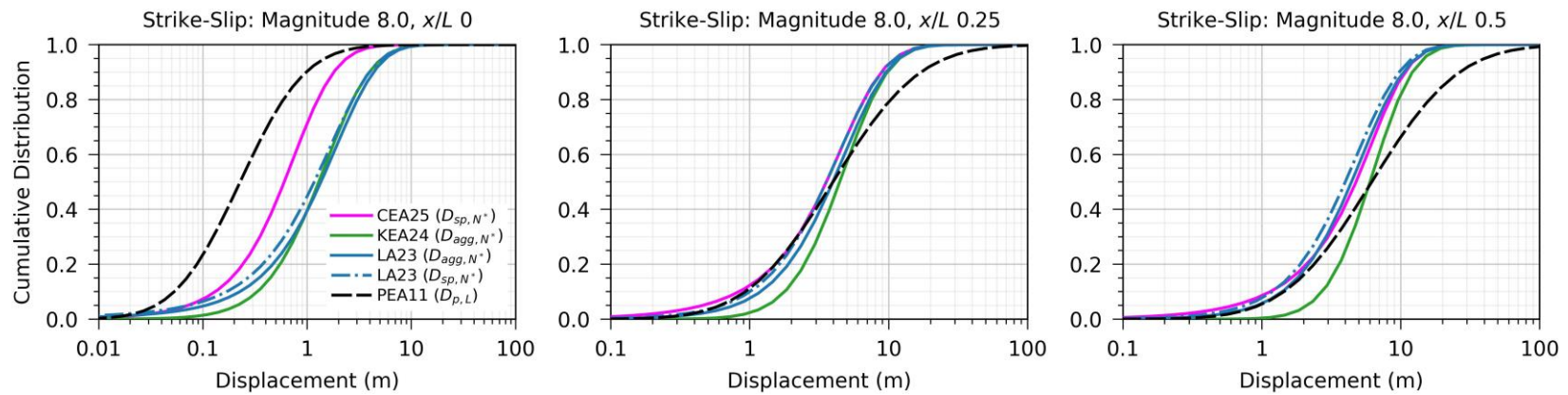


(a) Cumulative displacement probability curves.

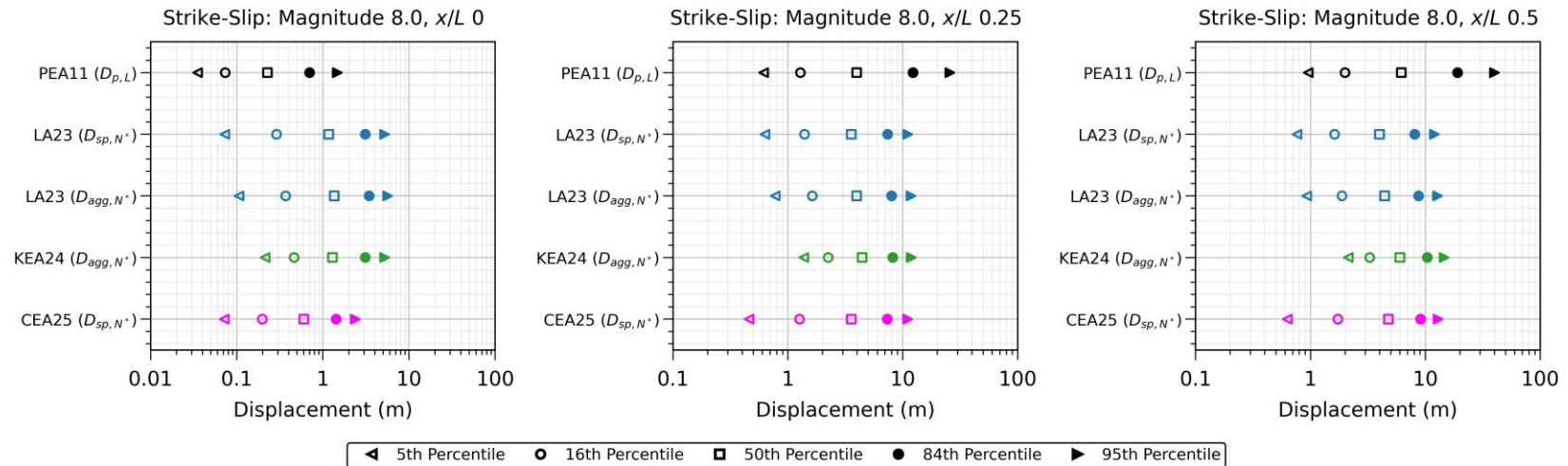


(b) Percentile displacement plots.

Figure 5.8. Comparison of aleatory variability for M 7.7 strike-slip events. Displacement definitions in parentheses are explained in Table 2.1.

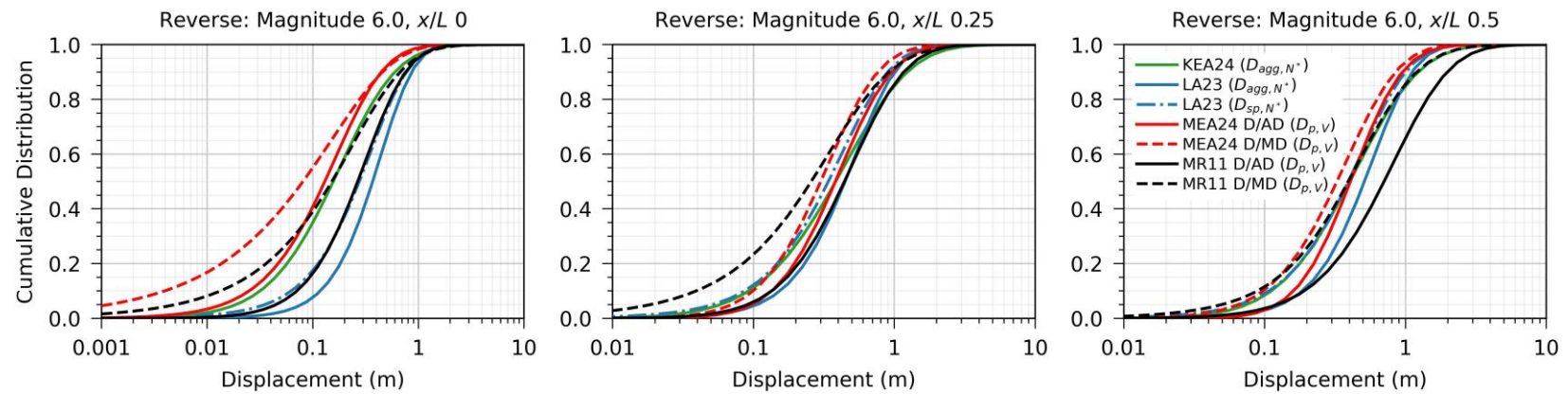


(a) Cumulative displacement probability curves.

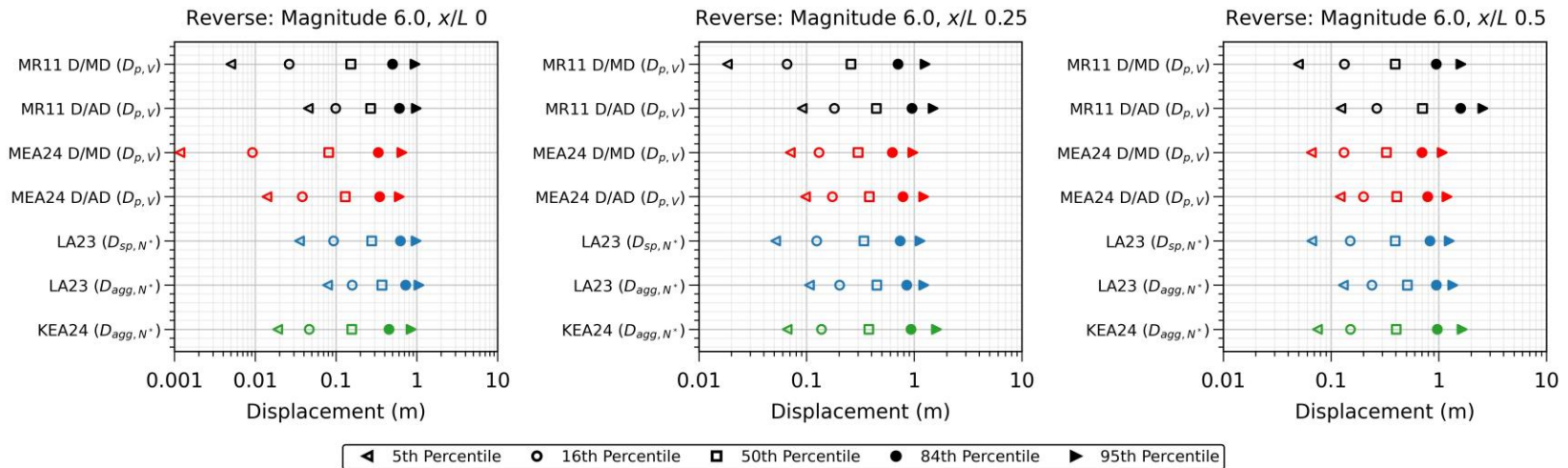


(b) Percentile displacement plots.

Figure 5.9. Comparison of aleatory variability for M 8.0 strike-slip events. Displacement definitions in parentheses are explained in Table 2.1.

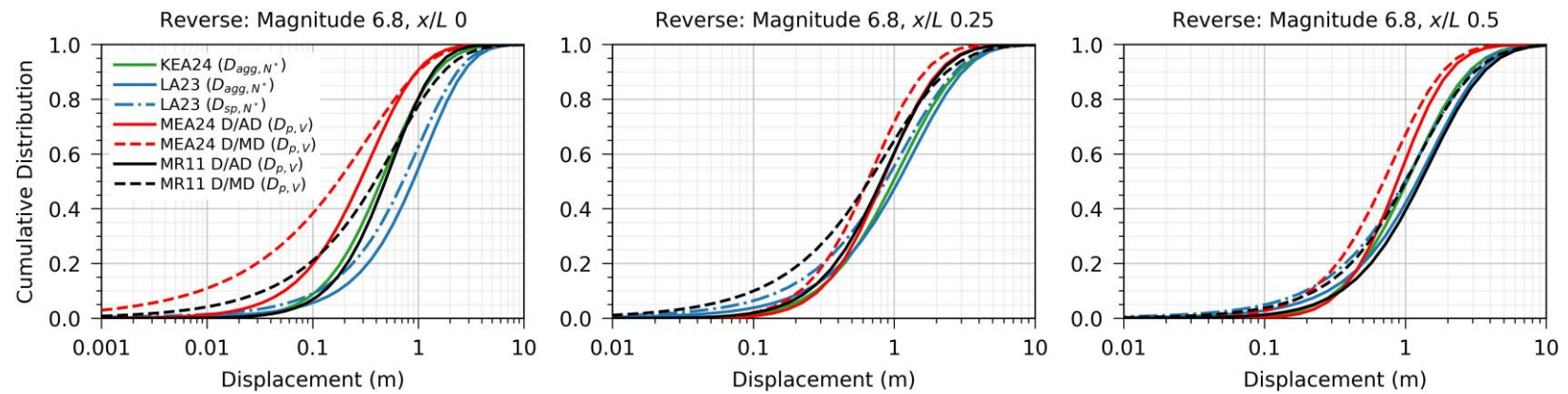


(a) Cumulative displacement probability curves.

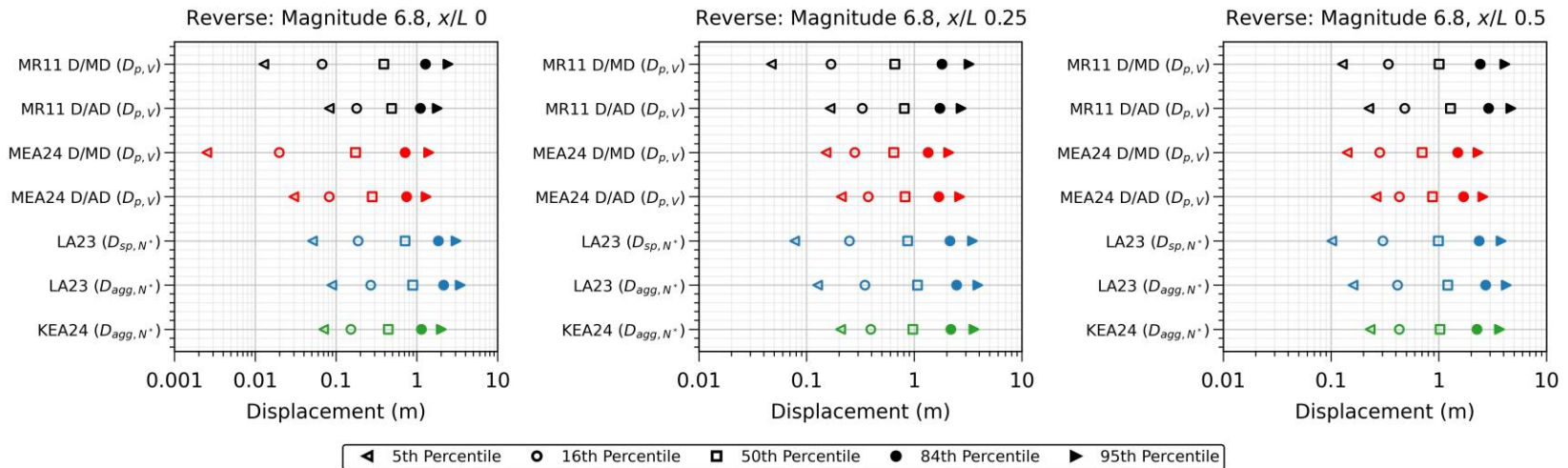


(b) Percentile displacement plots.

Figure 5.10. Comparison of aleatory variability for M 6.0 reverse events. Displacement definitions in parentheses are explained in Table 2.1.

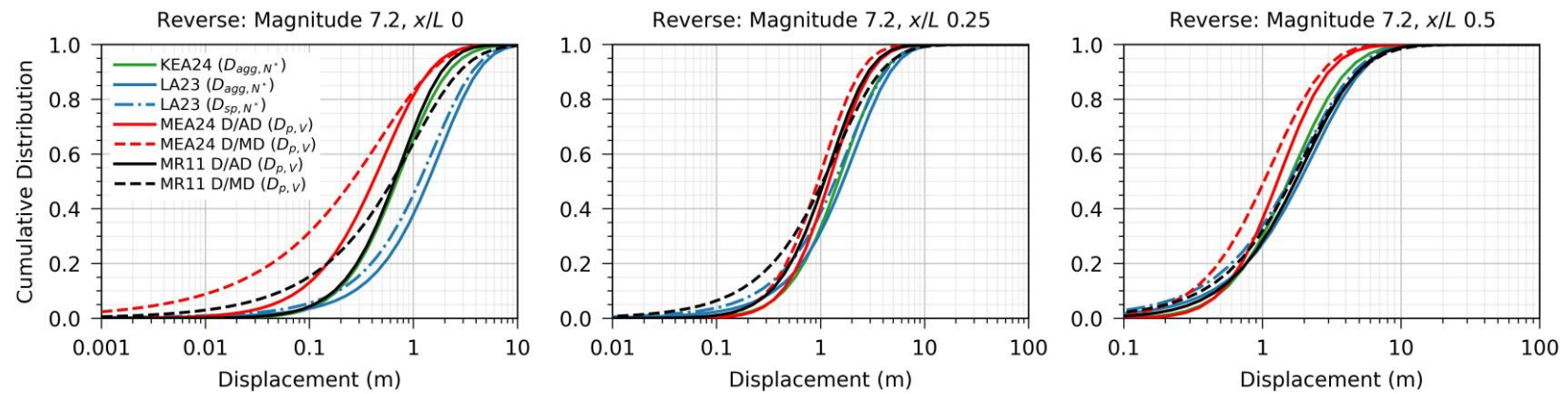


(a) Cumulative displacement probability curves.

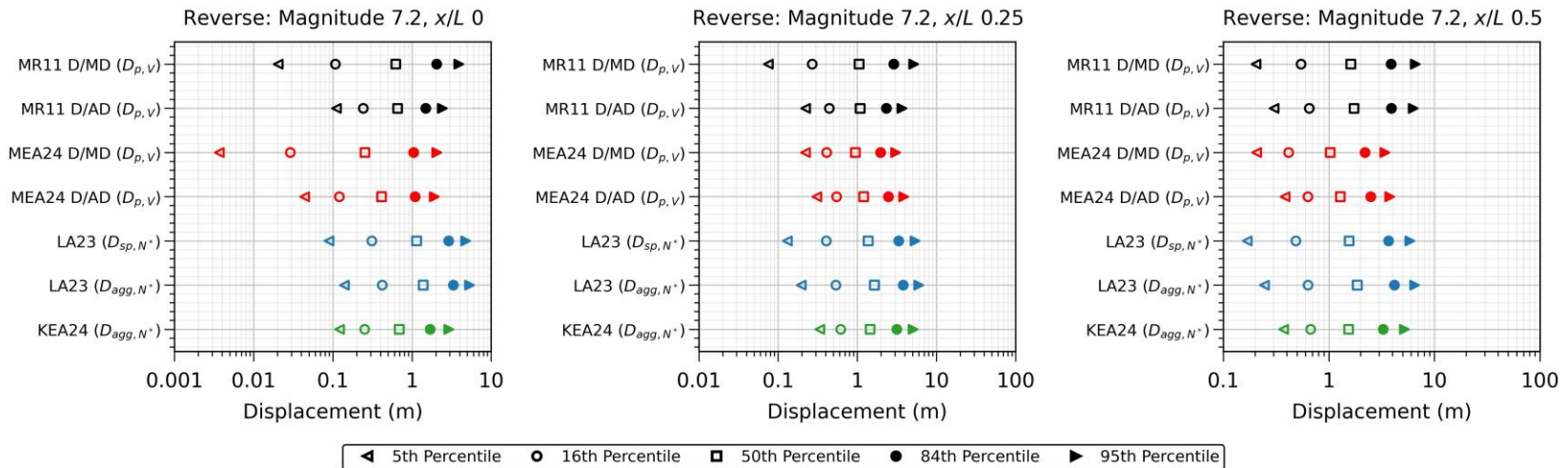


(b) Percentile displacement plots.

Figure 5.11. Comparison of aleatory variability for M 6.8 reverse events. Displacement definitions in parentheses are explained in Table 2.1.

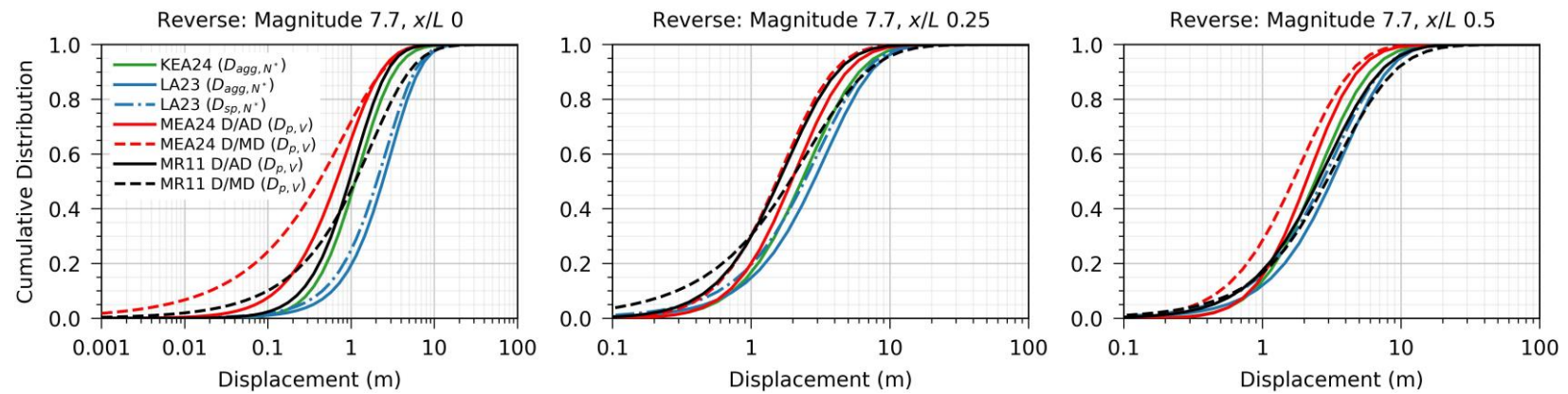


(a) Cumulative displacement probability curves.

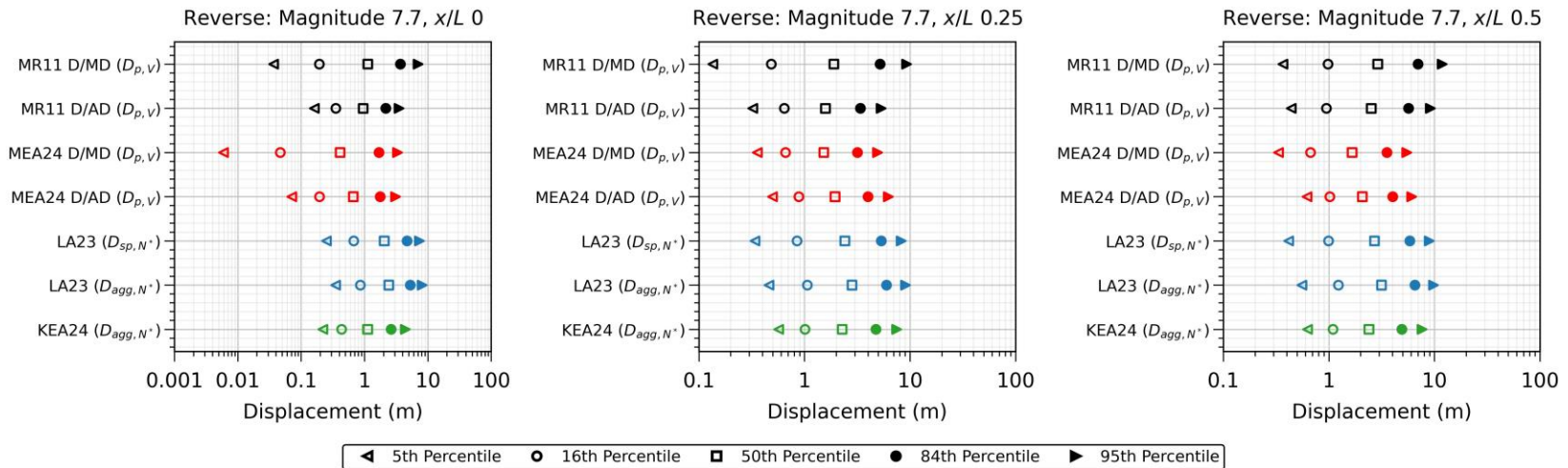


(b) Percentile displacement plots.

Figure 5.12. Comparison of aleatory variability for M 7.2 reverse events. Displacement definitions in parentheses are explained in Table 2.1.

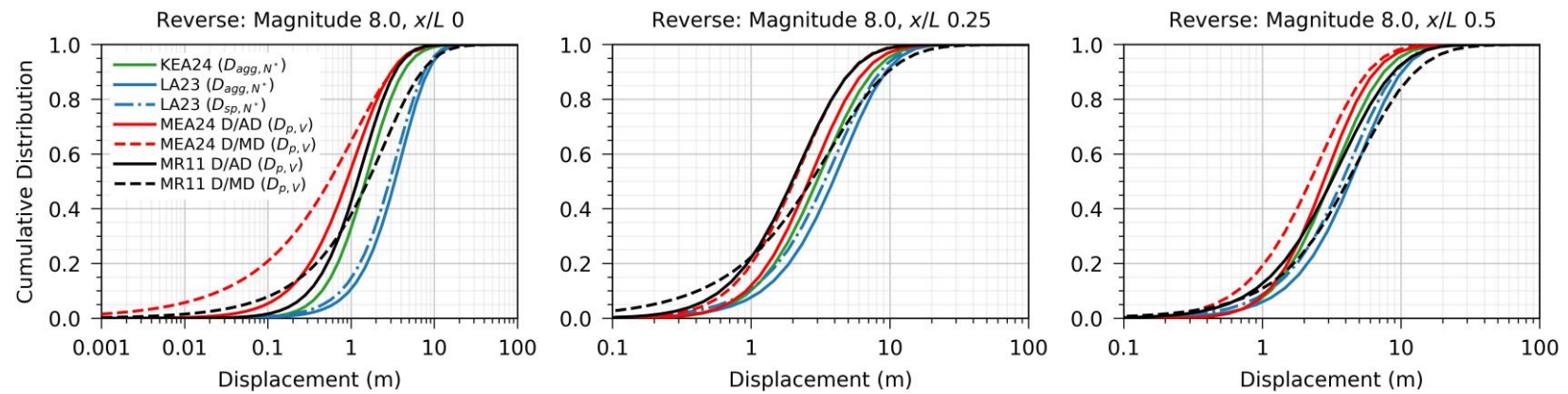


(a) Cumulative displacement probability curves.

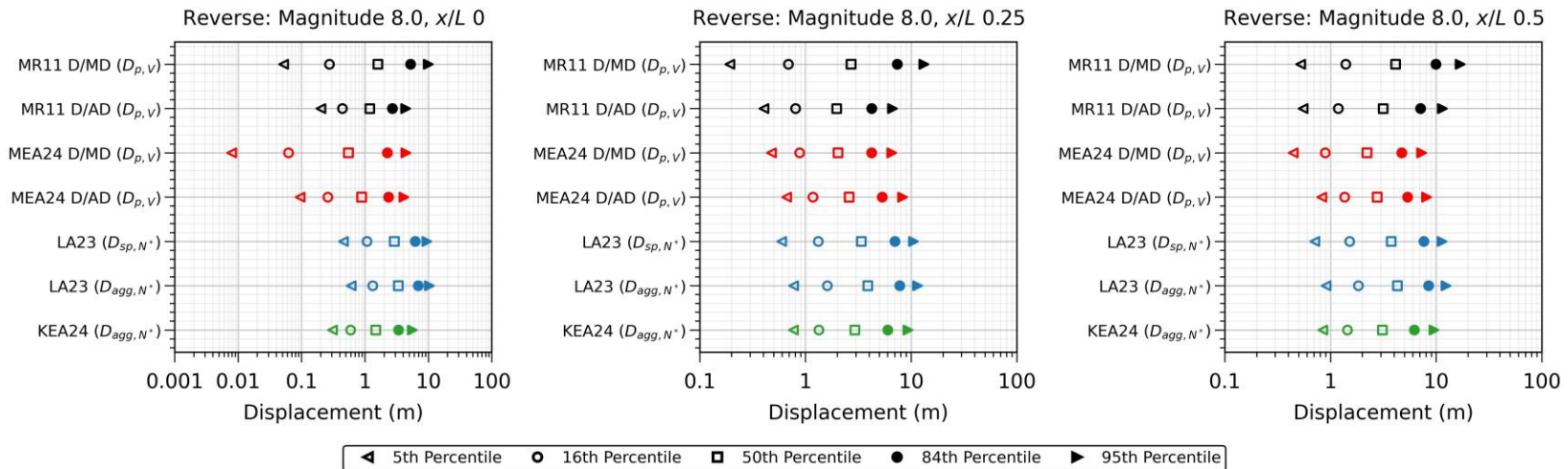


(b) Percentile displacement plots.

Figure 5.13. Comparison of aleatory variability for M 7.7 reverse events. Displacement definitions in parentheses are explained in Table 2.1.

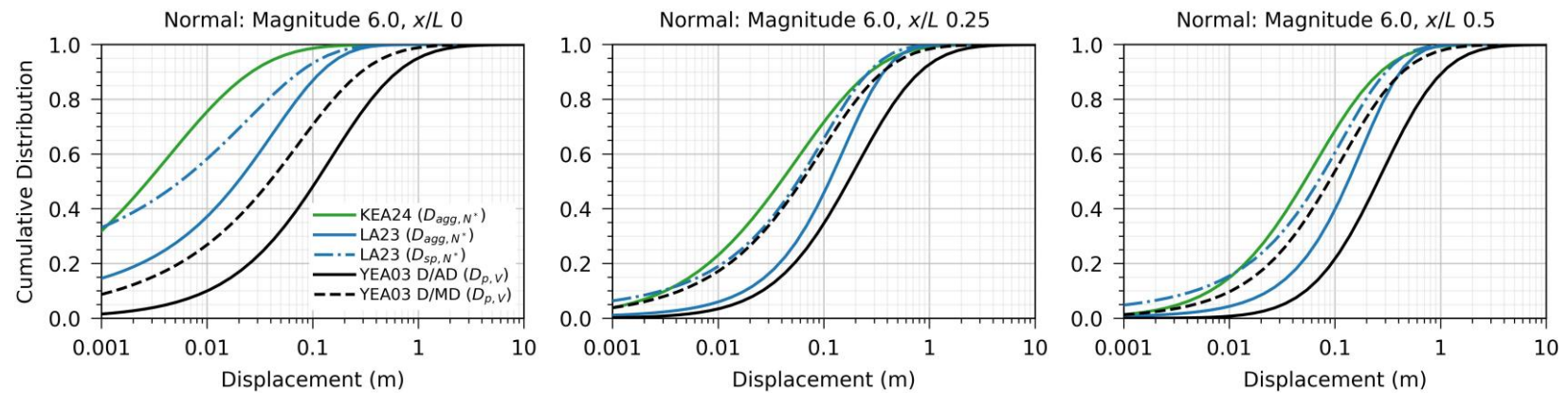


(a) Cumulative displacement probability curves.

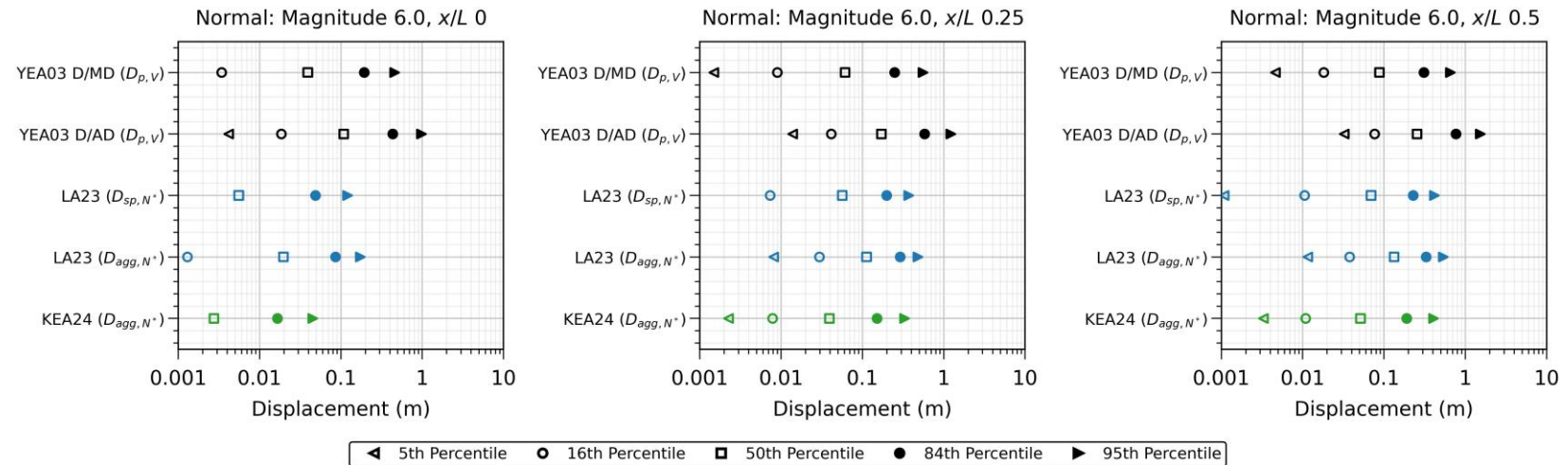


(b) Percentile displacement plots.

Figure 5.14. Comparison of aleatory variability for M 8.0 reverse events. Displacement definitions in parentheses are explained in Table 2.1.

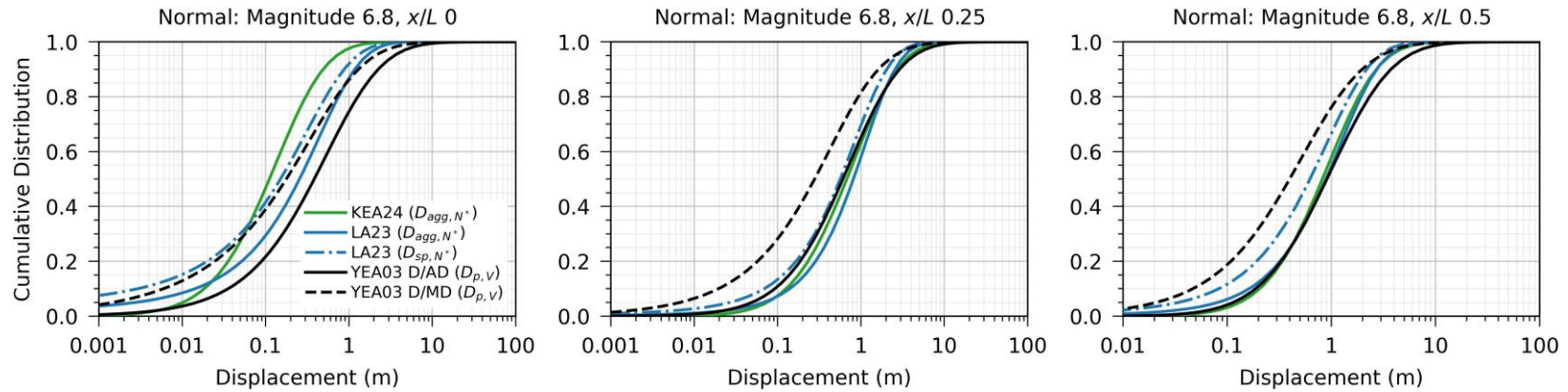


(a) Cumulative displacement probability curves.

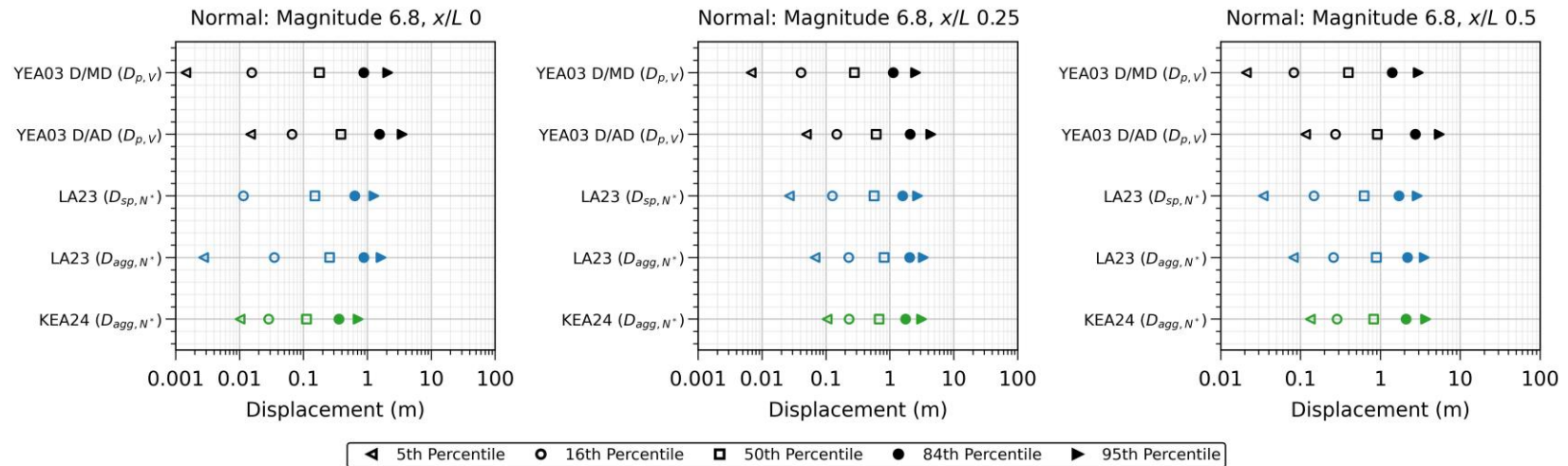


(b) Percentile displacement plots.

Figure 5.15. Comparison of aleatory variability for M 6.0 normal events. Displacement definitions in parentheses are explained in Table 2.1.

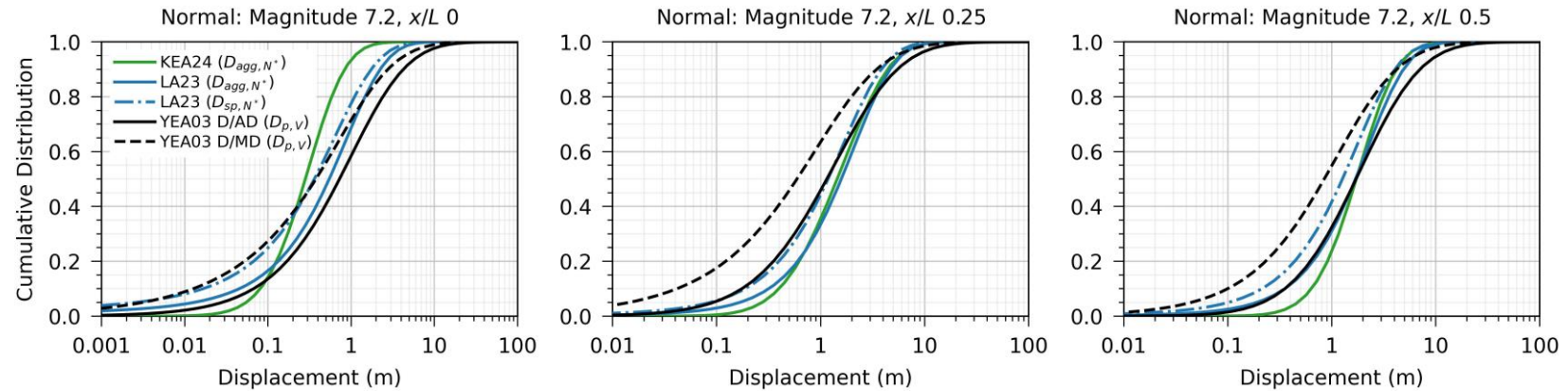


(a) Cumulative displacement probability curves.

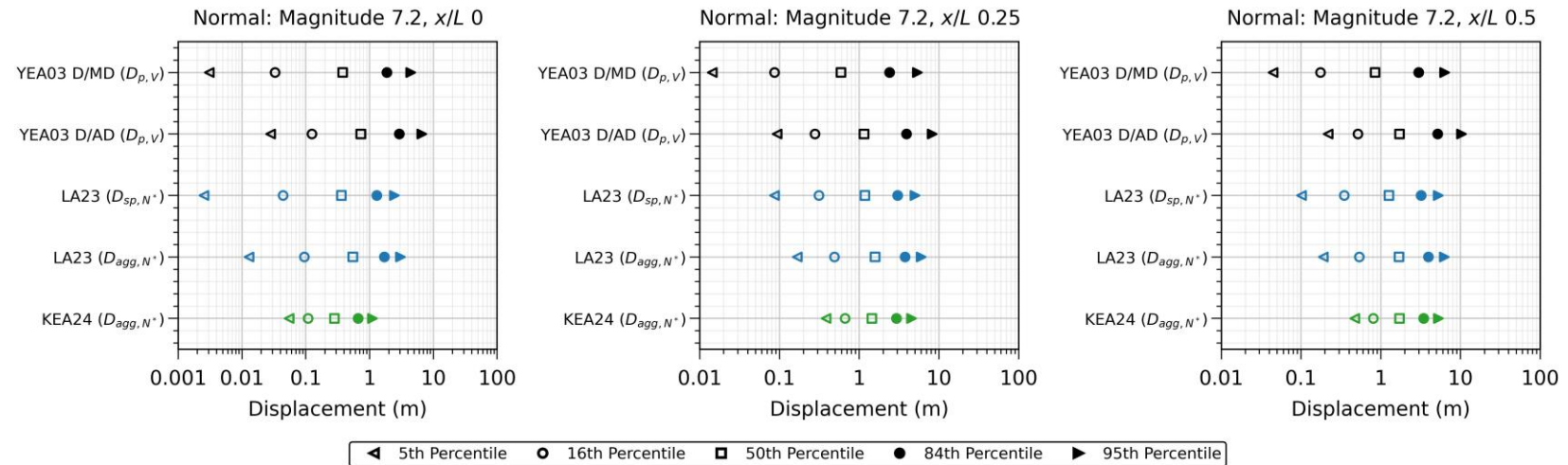


(b) Percentile displacement plots.

Figure 5.16. Comparison of aleatory variability for M 6.8 normal events. Displacement definitions in parentheses are explained in Table 2.1.

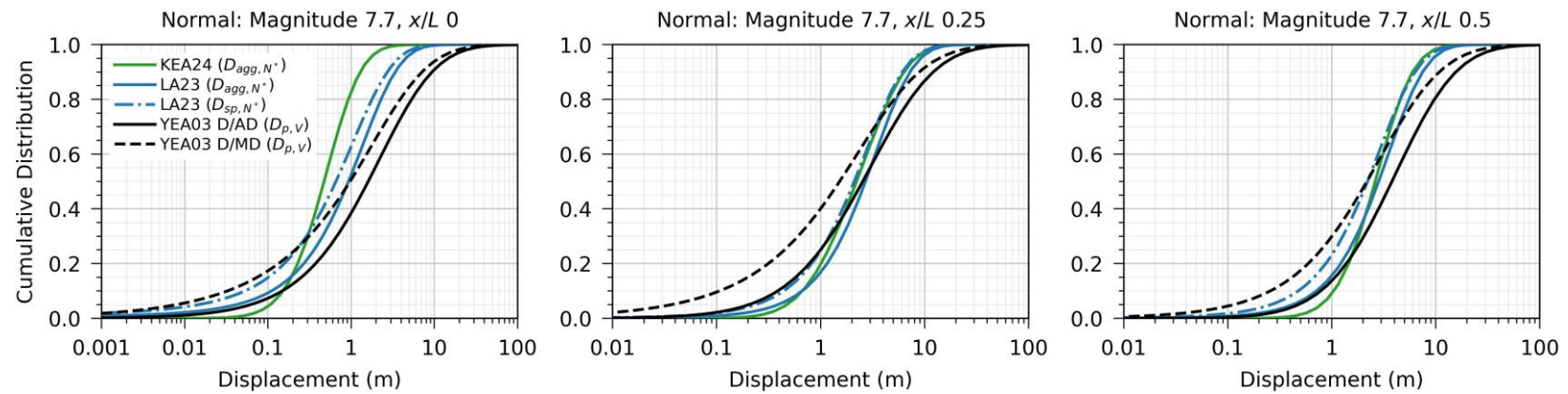


(a) Cumulative displacement probability curves.

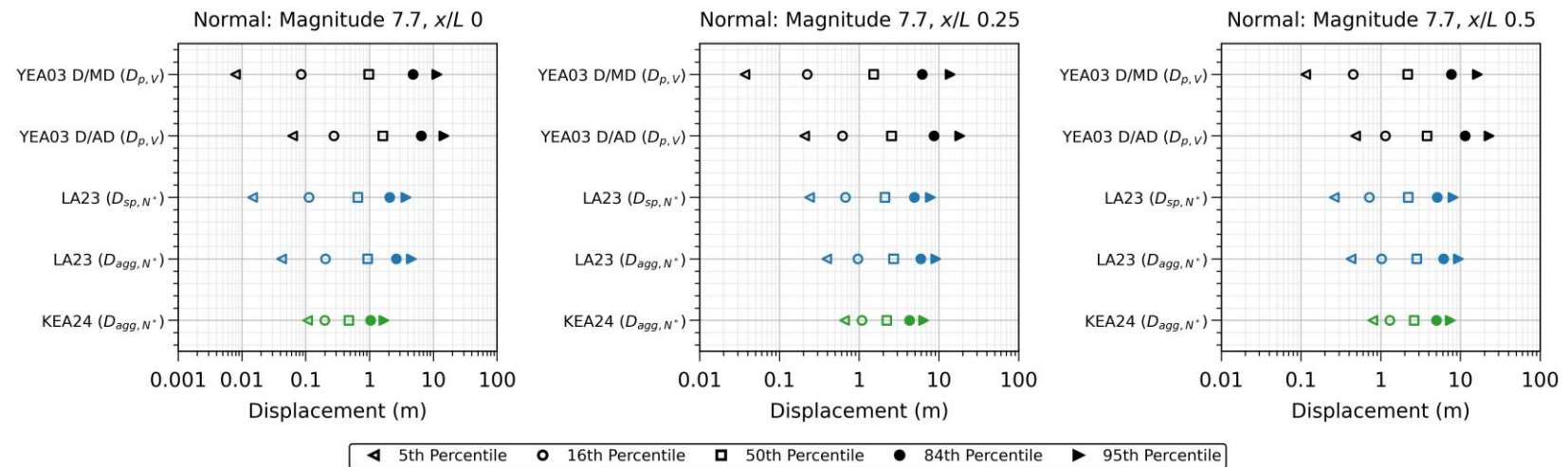


(b) Percentile displacement plots.

Figure 5.17. Comparison of aleatory variability for M 7.2 normal events. Displacement definitions in parentheses are explained in Table 2.1.

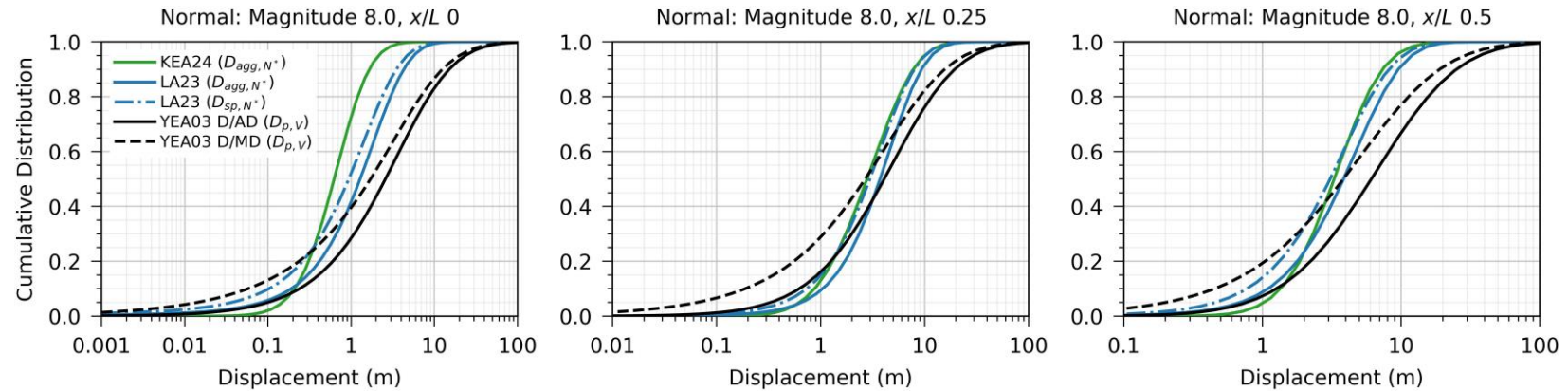


(a) Cumulative displacement probability curves.

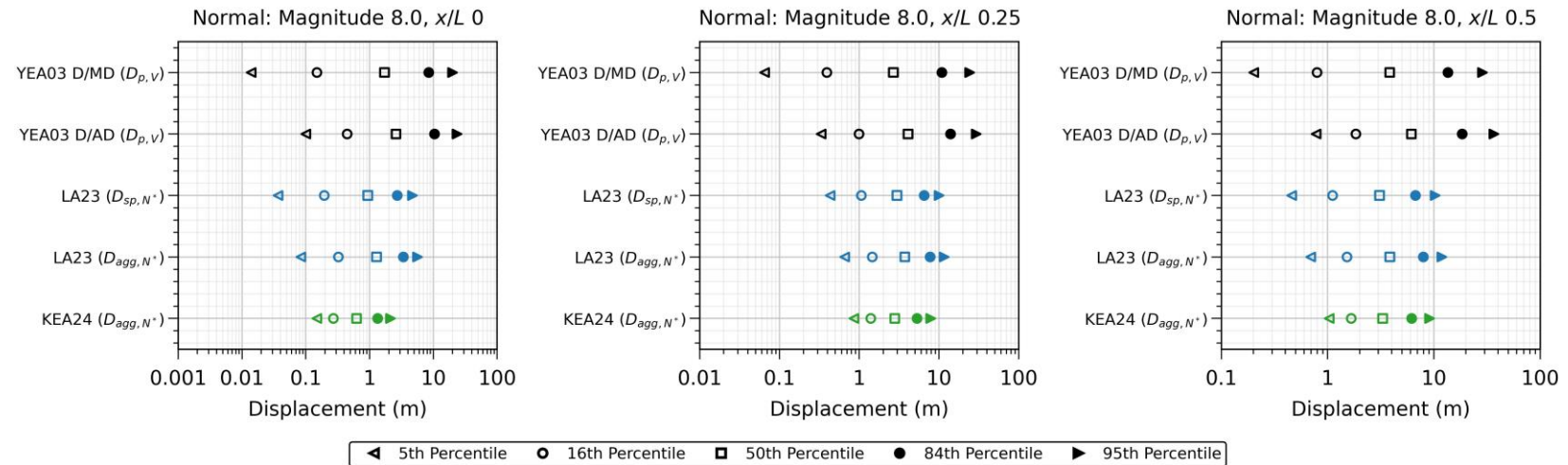


(b) Percentile displacement plots.

Figure 5.18. Comparison of aleatory variability for M 7.7 normal events. Displacement definitions in parentheses are explained in Table 2.1.



(a) Cumulative displacement probability curves.



(b) Percentile displacement plots.

Figure 5.19. Comparison of aleatory variability for M 8.0 normal events. Displacement definitions in parentheses are explained in Table 2.1.

5.5.2 Exceedance Probabilities

Probability of exceedance curves (i.e., complementary cumulative distribution functions) are shown for M 6, 7, and 8 for the rupture midpoint ($x/L = 0.5$; Figure 5.20) and endpoint ($x/L = 0$; Figure 5.21) to demonstrate the impact of the aleatory variability modeling components in hazard space. The LA23 results include the full distribution of displacements (i.e., zero and non-zero displacements). Incorporating zero displacements scales down the probability of exceedance.

While the details of the comparisons vary significantly and are complicated by the different definitions of displacement used in among the models (Table 2.1), some generalizations can be made:

- The FDHI models are most similar for M 7 strike-slip and normal events, and M 8 strike-slip events, where the 99th percentile predictions are within 15% for the rupture midpoint.
- The 99th percentile (10^{-2}) predictions for the rupture midpoint in the new FDHI models are within a factor of about 1.5 in most cases (Figure 5.20). Exceptions include M 6, where the strike-slip and reverse results in the FDHI models span factors of three and two, respectively, and M 7 reverse faulting where the MEA24 results are roughly half of the predictions in the other FDHI models. The MEA24 results are lower due to several factors, including the use of different datasets, modeling approaches, and definitions of displacement in their magnitude scaling models, which produces flatter magnitude scaling (Figures 5.2 and 5.4). Furthermore, the x/L scaling in MEA24 consistently produces lower displacements at the rupture midpoint and endpoint compared to other models (Figure 5.1).
- At the rupture endpoints (Figure 5.21), the 99th percentile predictions in the FDHI models are within a factor of three for strike-slip and normal events and within a factor of about two for reverse faulting.
- Compared to previously published models, the 99th percentile rupture midpoint displacements in the FDHI models for strike-slip and normal faulting are two to six times smaller than in previously PEA11 and YEA03, respectively (Figure 5.20). For reverse faulting, the FDHI model predictions vary from within about 5% to as much as three times less than the MR11 predictions (Figure 5.20).
- Compared to PEA11, the 99th percentile rupture endpoint displacements in the FDHI strike-slip models for are about three to five times larger due to larger mean predictions at the rupture endpoints (Figure 5.1) and up to eight times larger for M 7 due to nonlinear magnitude scaling (Figure 5.2).
- The FDHI models for reverse faulting generally span the range of the MR11 D/AD and D/MD model predictions at the rupture endpoint for the 99th percentile (Figure 5.21).

- The FDHI models for normal faulting produce 99th percentile range at the rupture endpoint that are three to ten times less than YEA03 due to reduced mean predictions at the rupture endpoints (Figure 5.1) and significantly lower between-event aleatory variability.

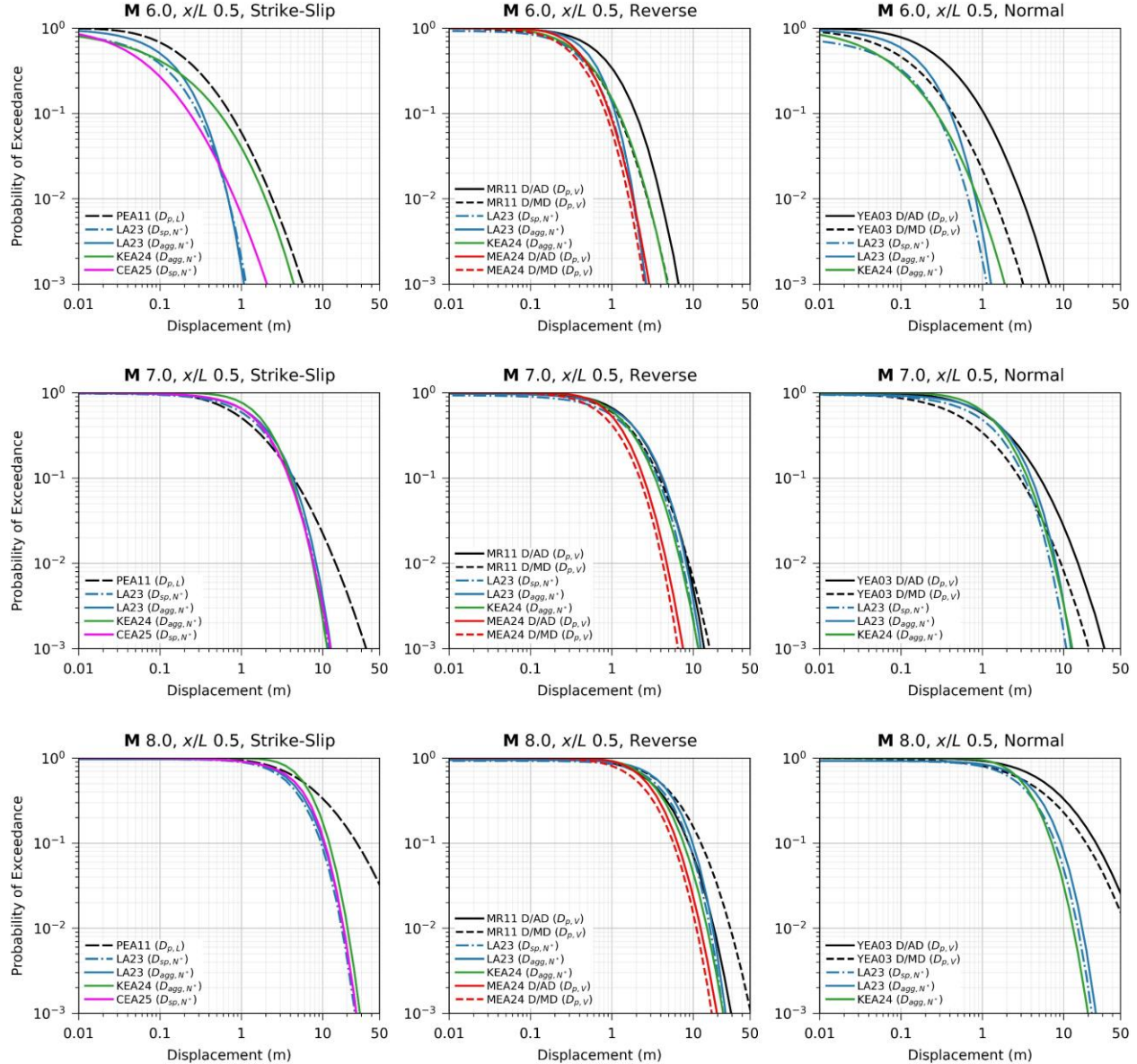


Figure 5.20. Comparison of probability of exceedance curves for **M 6** (top), **M 7** (middle), and **M 8** (bottom) at rupture midpoint ($x/L = 0.5$). Displacement definitions in parentheses are explained in Table 2.1.

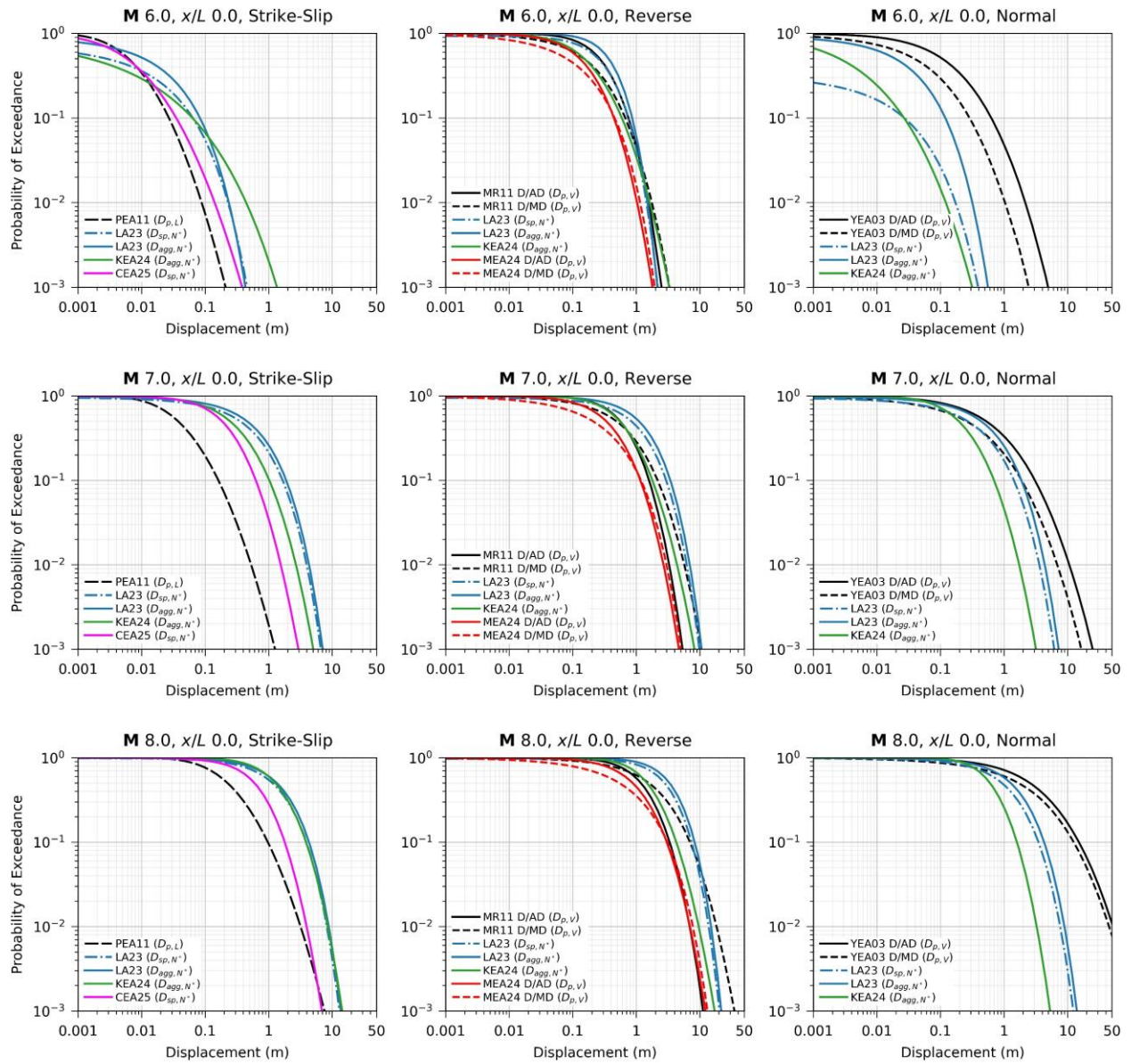


Figure 5.21. Comparison of probability of exceedance curves for **M 6** (top), **M 7** (middle), and **M 8** (bottom) at rupture endpoint ($x/L = 0$). Displacement definitions in parentheses are explained in Table 2.1.

6 Epistemic Uncertainty

This chapter summarizes the within-model epistemic uncertainty in the new FDMs. All models provide methods for evaluating within-model epistemic uncertainty to some extent, and this is a notable feature of the FDHI models. While each model handles epistemic uncertainty differently, it is generally captured with alternative model coefficients or quantified uncertainty on model predictions. Each model is discussed separately below. Comparisons are provided for broad range of scenarios (M 6, 7, and 8 at the rupture midpoint and endpoint) in the form of exceedance probabilities to demonstrate the impact of the epistemic uncertainty in hazard space.

We note that incorporating additional epistemic uncertainty (beyond what is currently provided in the models) may be warranted in some applications. Although the FDHI models were developed independently using different modeling approaches, and all models provide methods to capture at least some within-model epistemic uncertainty, the total uncertainty may still be underestimated. Future work evaluating between-model epistemic uncertainty could address these limitations.

6.1 LA23 MODEL

The LA23 model provides a parametric model for the epistemic uncertainty on the median aggregate displacement (μ_{agg}). Specifically, they provide a magnitude- and style-dependent standard deviation for the median aggregate displacement (in transformed units; $\sigma_{\mu-agg}$), as shown on Figure 6.1. The epistemic uncertainty is largest for small magnitudes and normal faulting events, smallest at $M > 7.1$, and independent of style at $M > 7.1$.

Figures 6.2 through 6.7 compare the epistemic uncertainty on the median aggregate displacement for the rupture endpoint ($x/L = 0$) and midpoint ($x/L = 0.5$), respectively, for M 6, 7, and 8 in the form of probability of exceedance curves for strike-slip, reverse, and normal events. Curves corresponding to the 5th and 95th percentile predictions for the median aggregate displacement are shown, along with the 50th percentile (i.e., without epistemic uncertainty). The median aggregate displacement adjusted for epistemic uncertainty is calculated as:

$$\mu_{agg-epi} = \mu_{agg} + \Phi^{-1}(p) \times \sigma_{\mu-agg} \quad (6.1)$$

where $\Phi^{-1}(p)$ is the inverse standard normal cumulative distribution function for the percentile p (i.e., the number of standard deviations corresponding to the percentile) and the exceedance probabilities are evaluated for $D^{0.3} \sim N(\mu_{agg-epi}, \sigma_{agg})$. The results include the full distribution of displacements (i.e., $P(Gap)$ is included to capture the probability of zero displacement). Incorporating zero displacements scales down the probability of exceedance. Uncertainty in the gap probability is not provided, so the 5th, 95th, and median (50th) percentile curves are scaled down by the same amount.

The impact of including epistemic uncertainty is largest for small magnitudes (Figure 6.1). For the **M** 6 cases, the 5th/95th percentiles span a factor of about two to five at a 10⁻² probability of exceedance, depending on style of faulting and x/L location. For the **M** 7 and 8 cases, the span ranges from about 1.25 to 1.4.

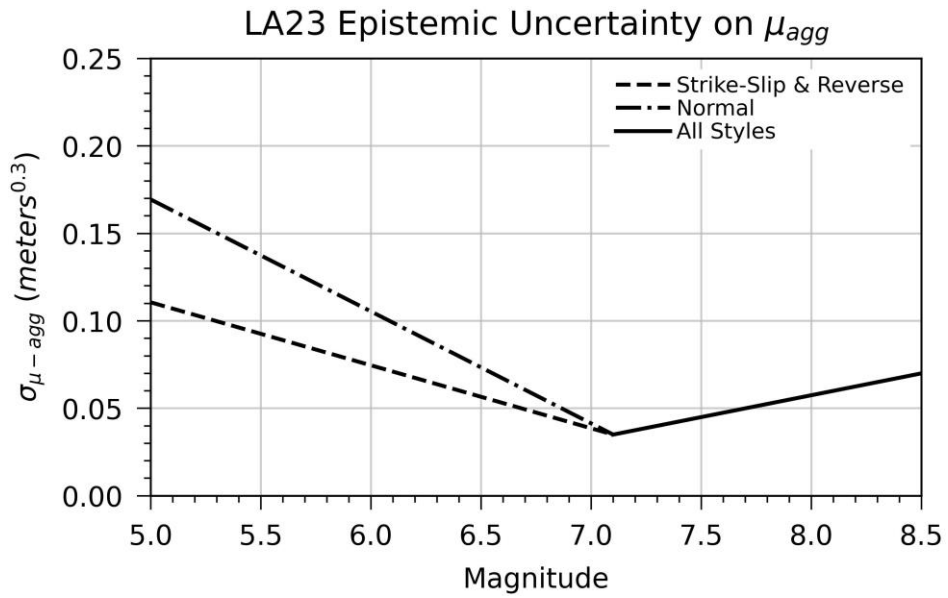


Figure 6.1. LA23 epistemic uncertainty model for the predicted median aggregate displacement in transformed units (μ_{agg}).

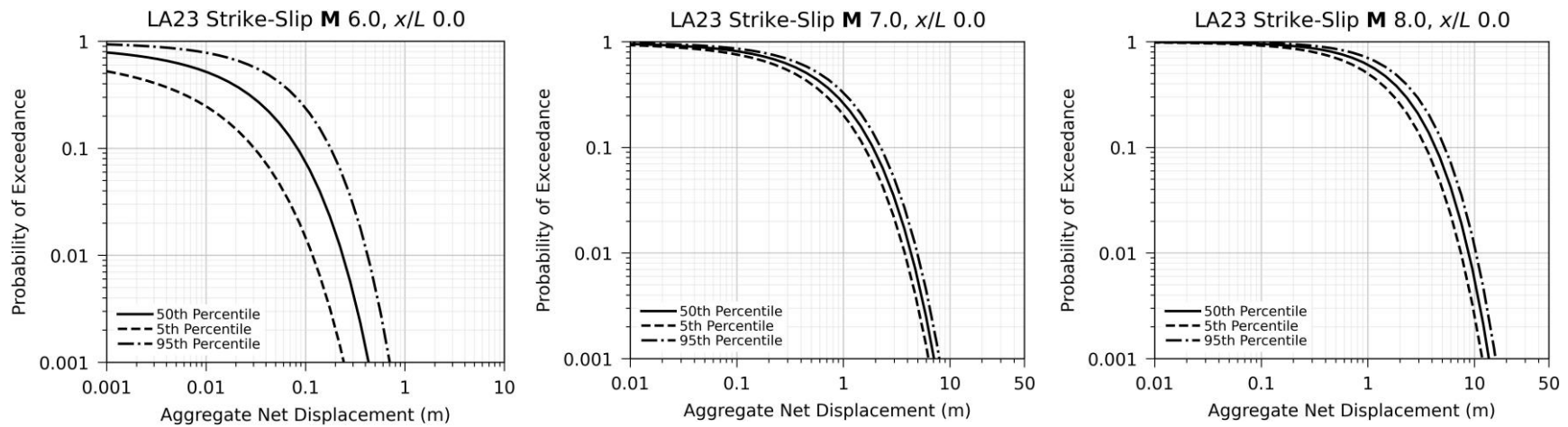


Figure 6.2. Comparison of LA23 within-model epistemic uncertainty at rupture endpoints for strike-slip events.

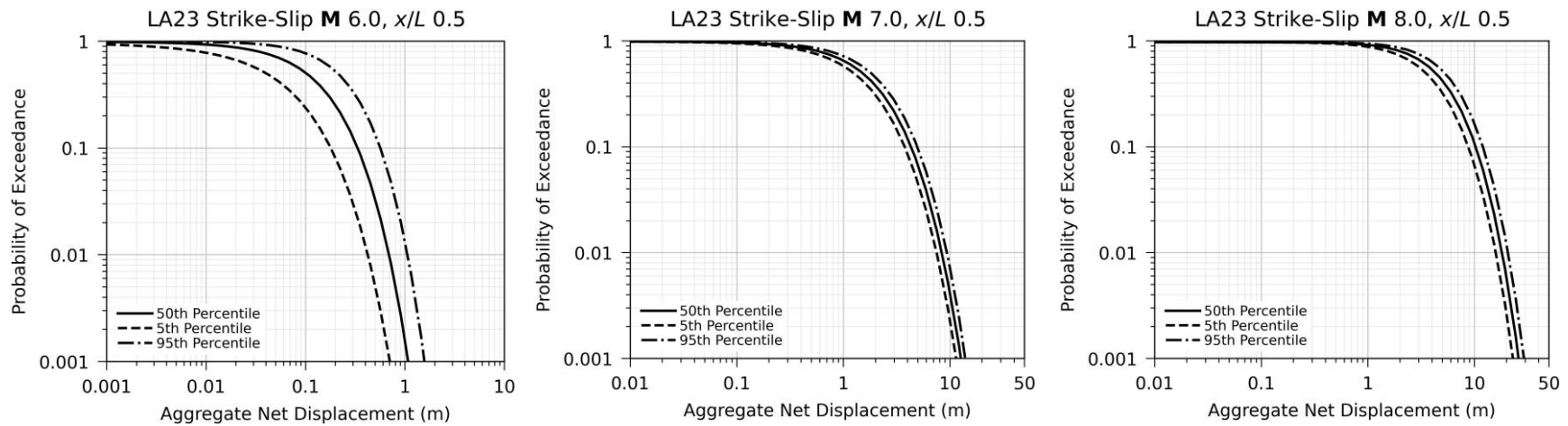


Figure 6.3. Comparison of LA23 within-model epistemic uncertainty at rupture midpoints for strike-slip events.

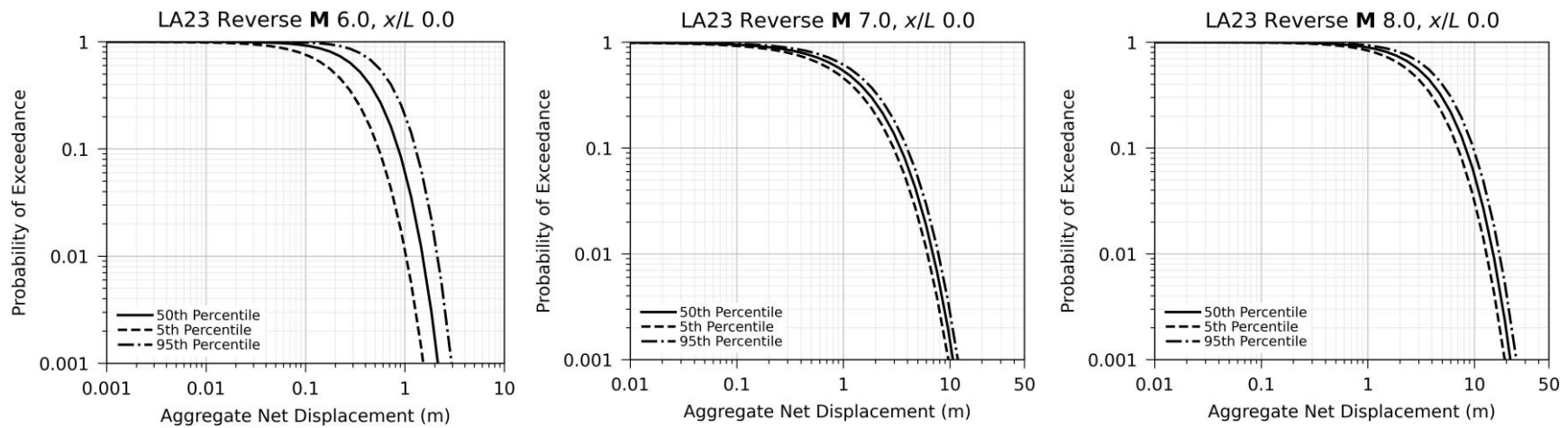


Figure 6.4. Comparison of LA23 within-model epistemic uncertainty at rupture endpoints for reverse events.

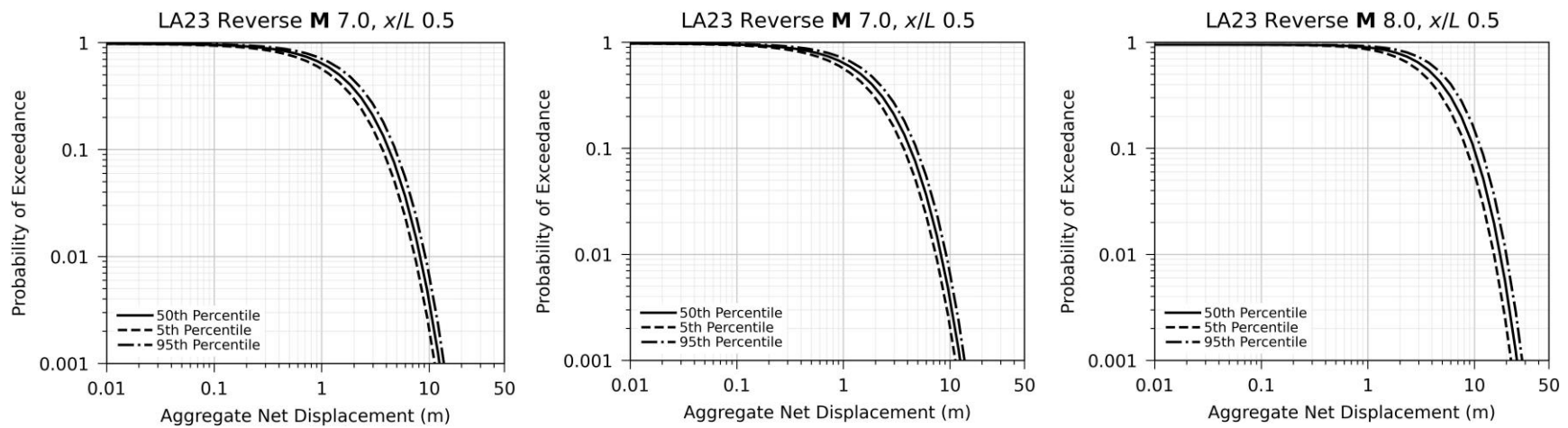


Figure 6.5. Comparison of LA23 within-model epistemic uncertainty at rupture midpoints for reverse events.

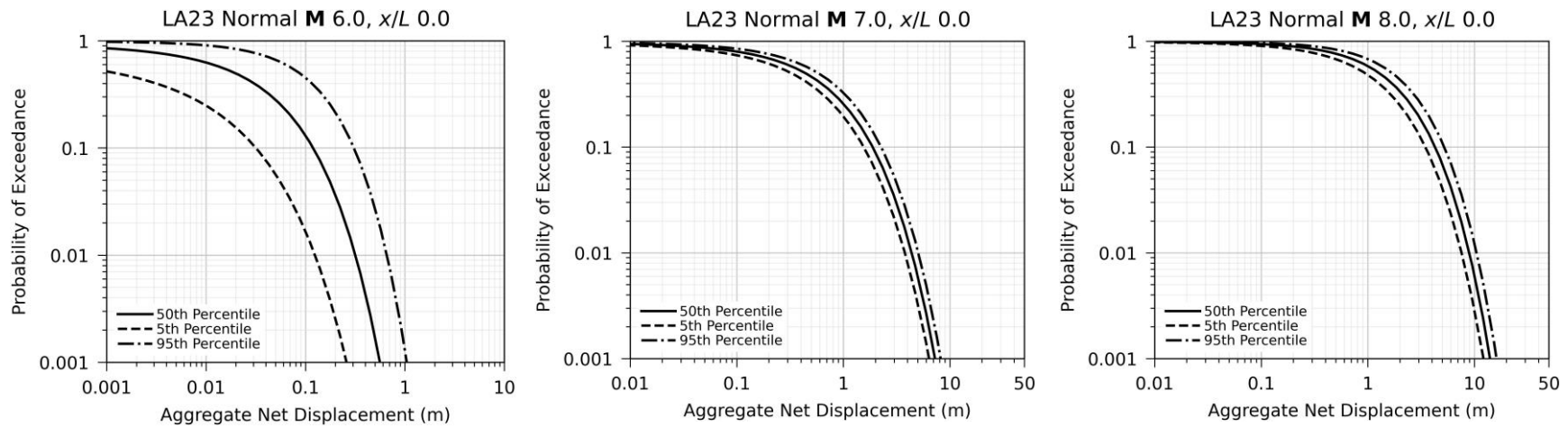


Figure 6.6. Comparison of LA23 within-model epistemic uncertainty at rupture endpoints for normal events.

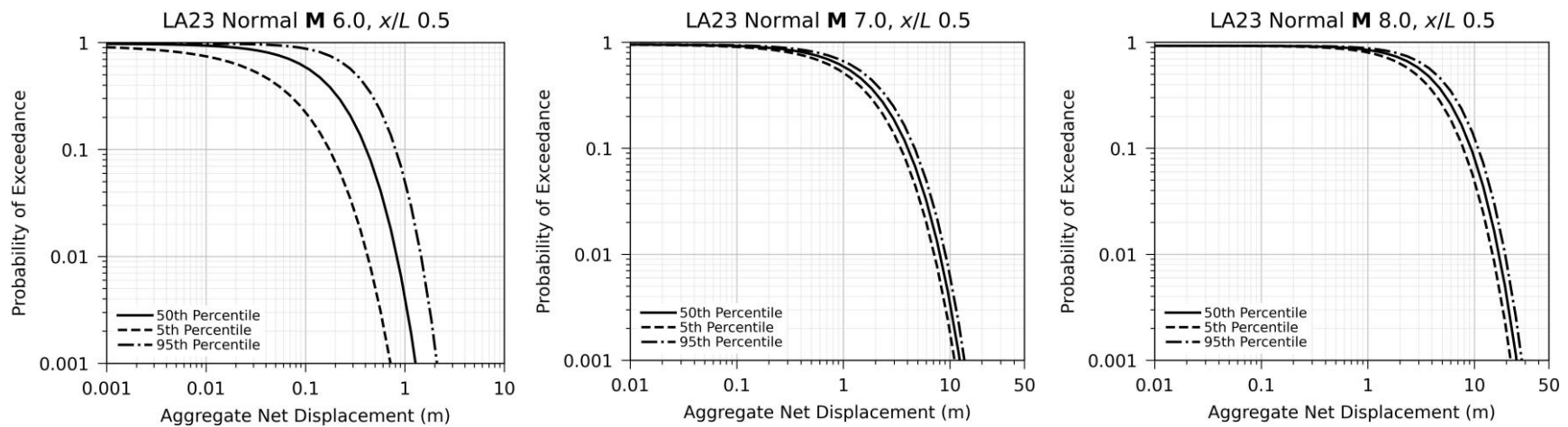


Figure 6.7. Comparison of LA23 within-model epistemic uncertainty at rupture midpoints for normal events.

6.2 MEA24 MODEL

MEA24 provide alternative regression coefficients for their *AD* and *MD* models, which are compared in detail in Moss et al. (2022). Their *D/AD* and *D/MD* models provide between-model epistemic uncertainty. The alternative regression coefficients in their *AD* and *MD* models are based on their full empirical dataset and a subset of the data that correspond to datasets considered to be more complete. Both complete subsets have lower aleatory variability.

Figures 6.8 and 6.9 compare the epistemic uncertainty in the MEA24 model for the rupture endpoint ($x/L = 0$) and midpoint ($x/L = 0.5$), respectively, for M 6, 7, and 8 in the form of probability of exceedance curves. The *D/AD* median predictions (i.e., a 0.5 probability of exceedance) are similar for both *AD* models and higher than the *D/MD* median predictions for all magnitudes and both x/L locations. The *D/MD* median predictions using the “complete” *MD* subset are about two to three times higher than with the “full” dataset.

With respect to the within-model epistemic uncertainty, the 99th percentile (i.e., a 10⁻² probability of exceedance) predictions for the *D/AD* alternatives are closer than the *D/MD* alternatives. In both cases, spread increases with magnitude and the spread is larger at rupture midpoint. The results for the *D/AD* alternatives are within about 8% (M 6, $x/L = 0$) to about 17% (M 8, $x/L = 0.5$). The results for the *D/MD* alternatives are within about 7% (M 6, $x/L = 0$) to about 29% (M 8, $x/L = 0.5$).

With respect to the between-model epistemic uncertainty, the *D/MD* 99th percentile predictions for the rupture endpoint about 10% higher than *D/AD* for all magnitudes, regardless of the *MD* and *AD* model used. At the rupture midpoint, regardless of magnitude, the *D/MD* and *D/AD* 99th percentile results are nearly identical for when the full *MD* or *AD* dataset is used, and the *D/MD* results are about 10% lower than *D/AD* results when the complete subset is used.

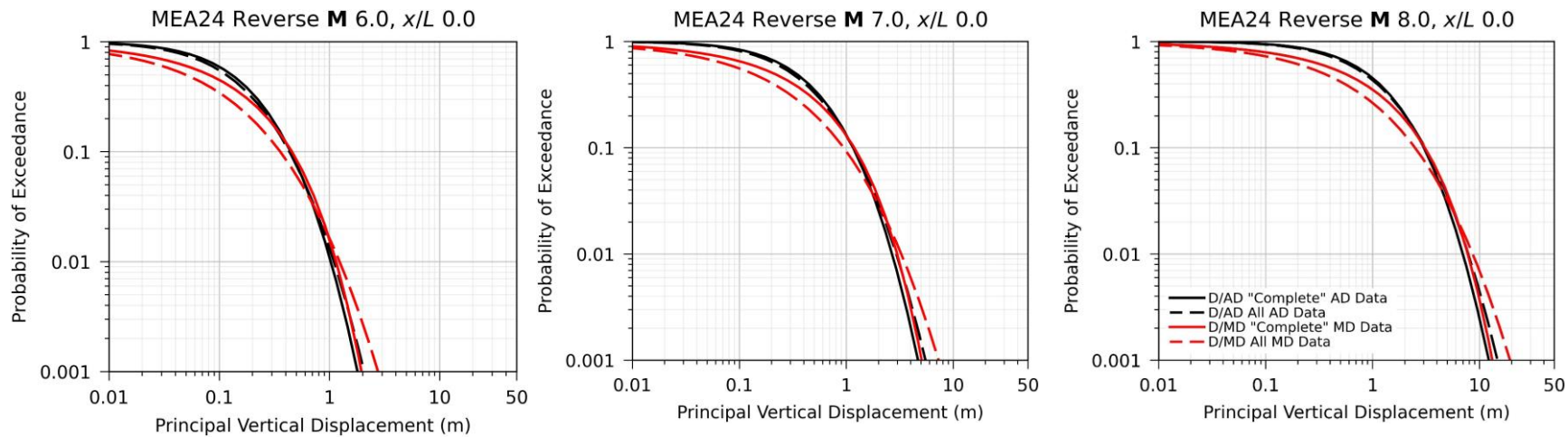


Figure 6.8. Comparison of MEA24 within- and between-model epistemic uncertainty at rupture endpoints. Legend applies to all.

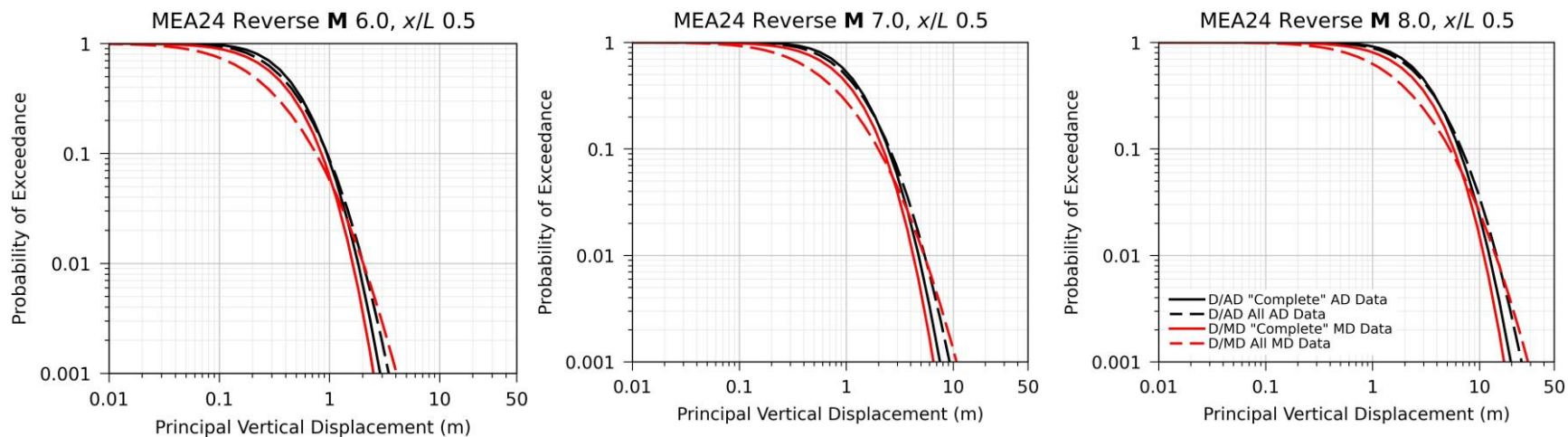


Figure 6.9. Comparison of MEA24 within- and between-model epistemic uncertainty at rupture midpoints. Legend applies to all.

6.3 KEA24 MODEL

The KEA24 model was developed using Bayesian regression. As a result, the model coefficients are defined by posterior distributions, which provide the full within-model epistemic uncertainty. The KEA24 developers provide 1000 sets of correlated coefficients sampled from the posterior distributions for each style of faulting. The full epistemic uncertainty can be evaluated by computing the hazard for each set.

The KEA24 developers also provide a simplified approach to estimate the within-model epistemic uncertainty by numerically estimating the uncertainty on the predictions for the median (μ) and standard deviation (σ_T). Pre-computed standard deviations on the median and standard deviation (σ_μ and σ_{σ_T} , respectively) are provided by KEA24 for a set of scenarios (style, M , x/L), and linear interpolation is used for other scenarios. The pre-computed standard deviations are shown on Figure 6.10 (σ_μ) and Figure 6.11 (σ_{σ_T}). The values are largest where data are sparse, such as small magnitude strike-slip and normal faulting events. In forward application, these standard deviations can be used to generate a scaled backbone model, and the epistemic uncertainty can be captured in a logic tree by using a three-point discrete approximation for a normal distribution (Al Atik and Youngs, 2014; Keefer and Bodily, 1983). Figure 6.12 shows the logic tree implementation.

Figures 6.13 through 6.18 show the within-model epistemic uncertainty for the rupture endpoint ($x/L = 0$) and midpoint ($x/L = 0.5$), respectively, for M 6, 7, and 8 in the form of probability of exceedance curves for strike-slip, reverse, and normal events. Each figure shows the full epistemic uncertainty by evaluating 1000 sets of correlated model coefficients and the estimated epistemic uncertainty using the scaled backbone approach. The mean for each method is shown, along with the mean without any epistemic uncertainty (using median coefficients). As discussed in the Electronic Supplement to Kuehn et al. (2024), the mean curve developed from the scaled backbone approach captures the full epistemic uncertainty very well for most cases.

While the impact of including epistemic uncertainty is largest for small magnitude strike-slip and normal events and smallest for $M \sim 7$ reverse and strike-slip events, the details vary significantly across the scenarios. For example, the full epistemic uncertainty spans a factor of over 300 at a 10^{-2} probability of exceedance for a M 6 strike-slip at the rupture endpoint ($x/L = 0$; Figure 6.13) but only a factor of about 2.5 at the midpoint of a M 7 strike-slip event ($x/L = 0.5$; Figure 6.14). The full epistemic uncertainty is narrowest for reverse events, spanning a factor of roughly 3 to 5 at a 10^{-2} probability of exceedance regardless of magnitude or x/L location (Figures 6.15 and 6.16). The full epistemic uncertainty is widest for normal events, spanning a factor of almost 1000 at a 10^{-2} probability of exceedance for a M 6 at the rupture endpoint (Figure 6.17) and more than four at the midpoint of a M 7 event (Figure 6.18).

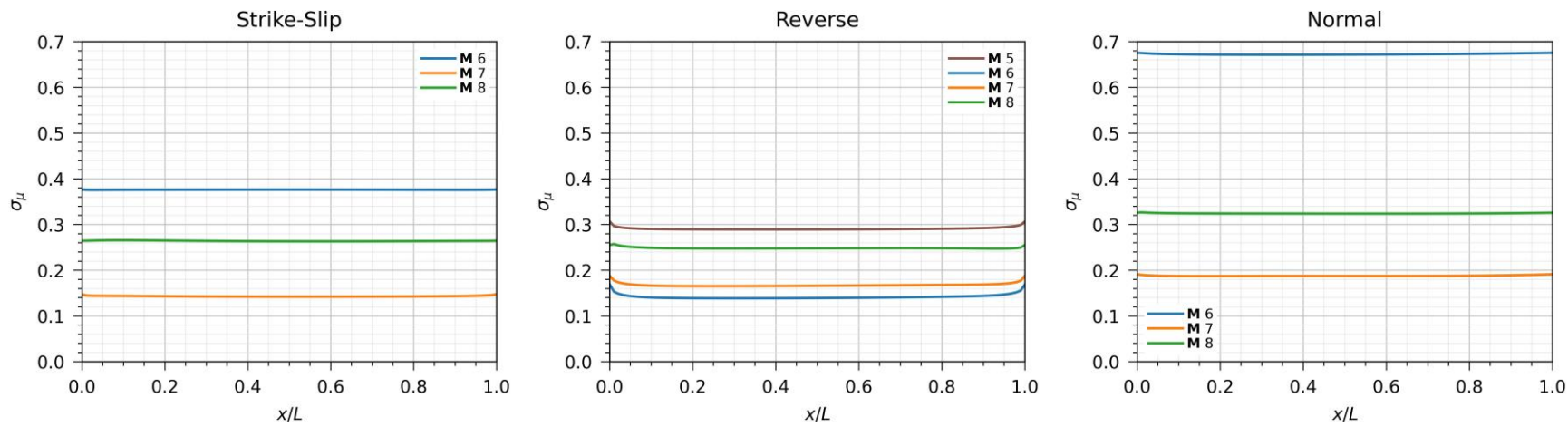


Figure 6.10. KEA24 estimated epistemic uncertainty on the predicted median (μ) in Box-Cox transformation units.

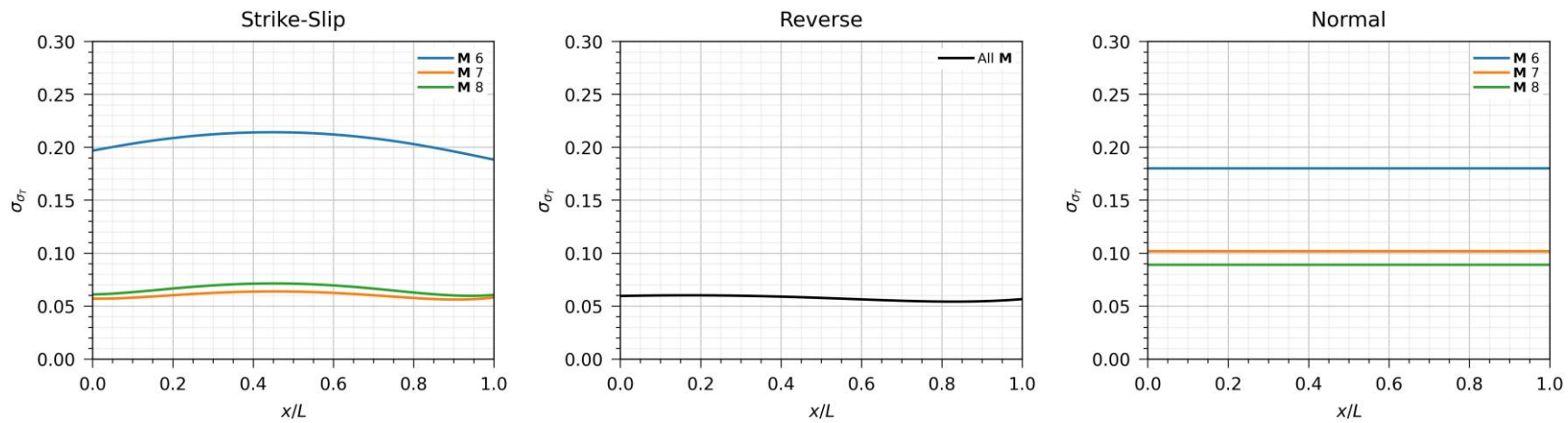


Figure 6.11. KEA24 estimated epistemic uncertainty on the predicted standard deviation (σ_T) in Box-Cox transformation units.

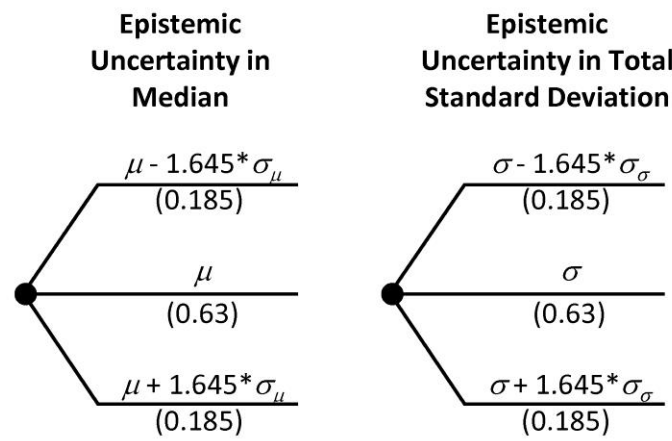


Figure 6.12. Logic tree for capturing epistemic uncertainty in median prediction μ and standard deviation σ_T in KEA24 model.

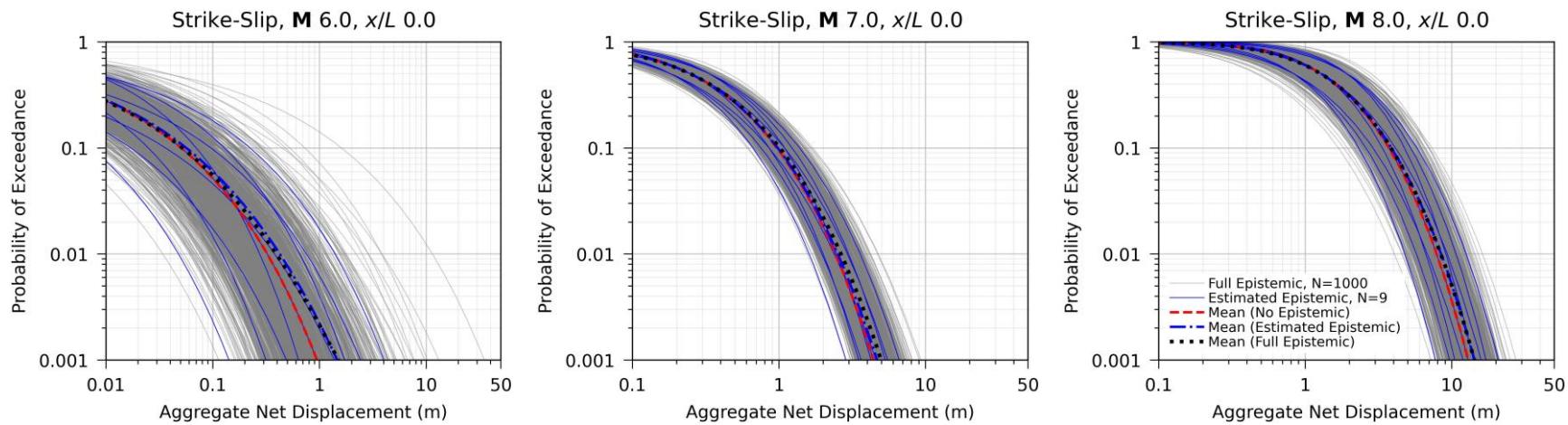


Figure 6.13. Comparison of KEA24 within-model epistemic uncertainty at rupture endpoints for strike-slip events. Legend applies to all.

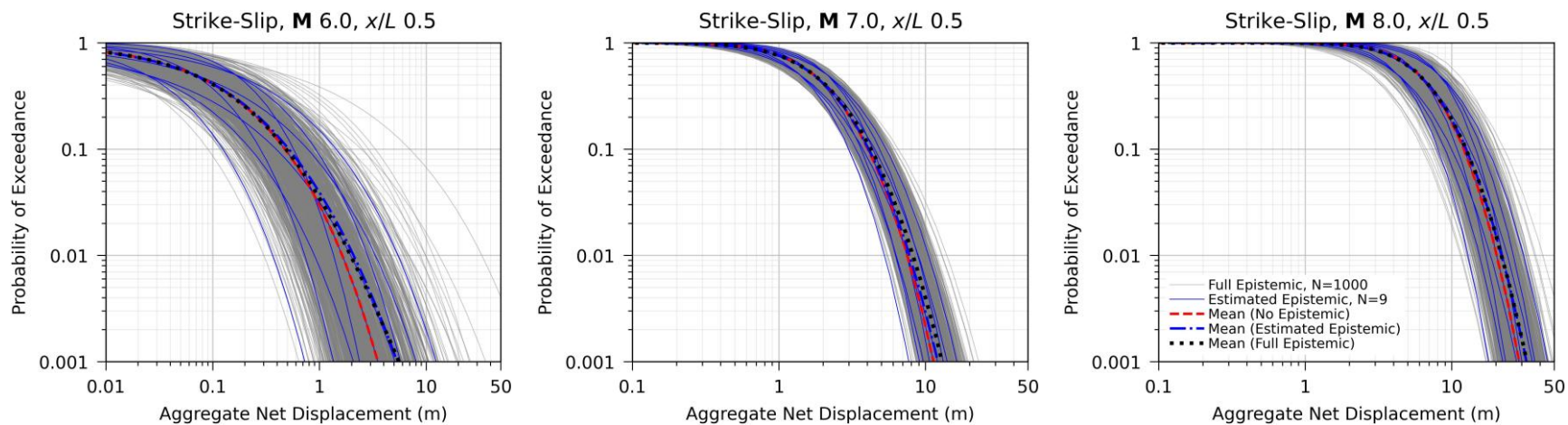


Figure 6.14. Comparison of KEA24 within-model epistemic uncertainty at rupture midpoints for strike-slip events. Legend applies to all.

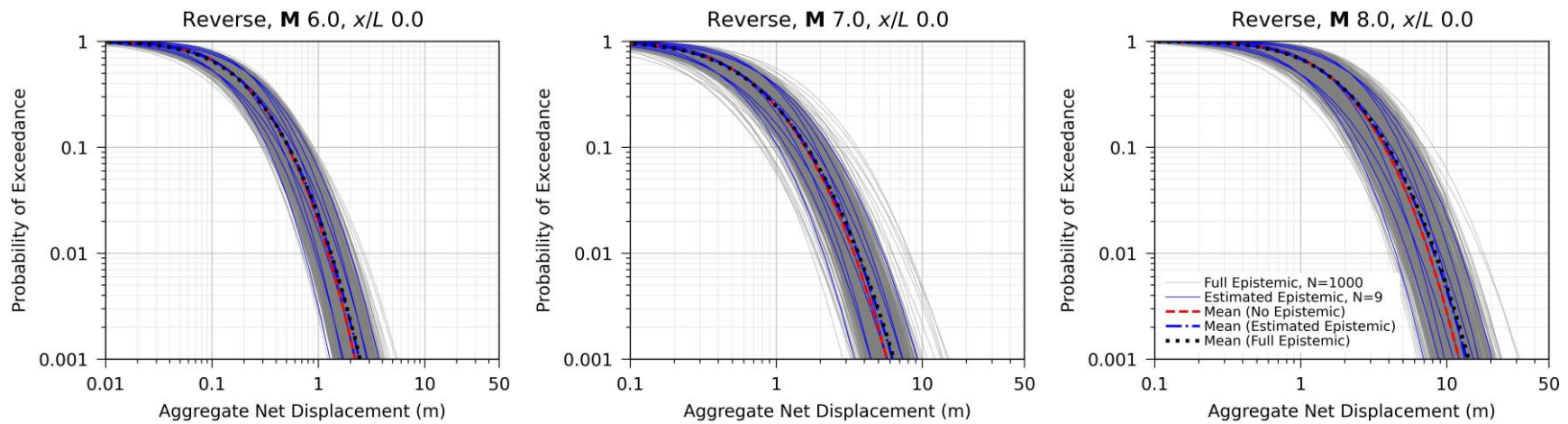


Figure 6.15. Comparison of KEA24 within-model epistemic uncertainty at rupture endpoints for reverse events. Legend applies to all.

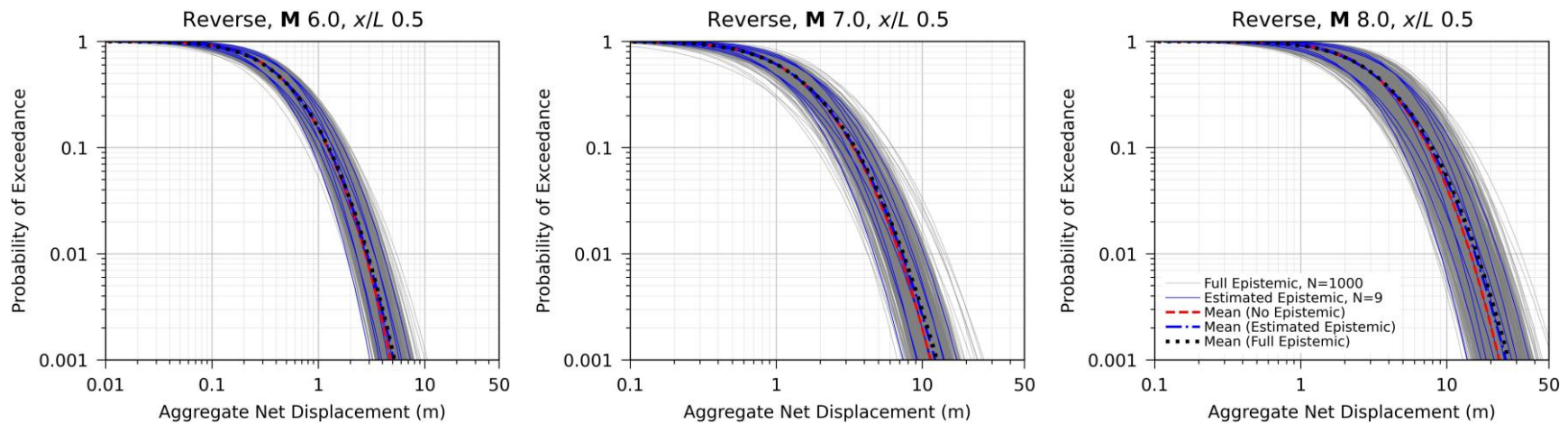


Figure 6.16. Comparison of KEA24 within-model epistemic uncertainty at rupture midpoints for reverse events. Legend applies to all.

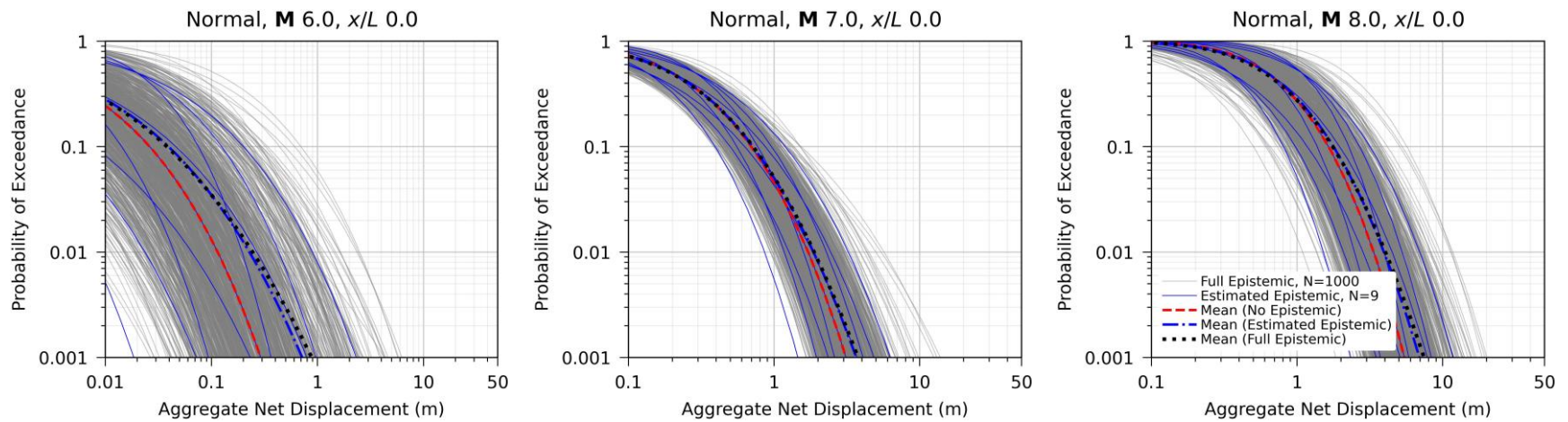


Figure 6.17. Comparison of KEA24 within-model epistemic uncertainty at rupture endpoints for normal events. Legend applies to all.

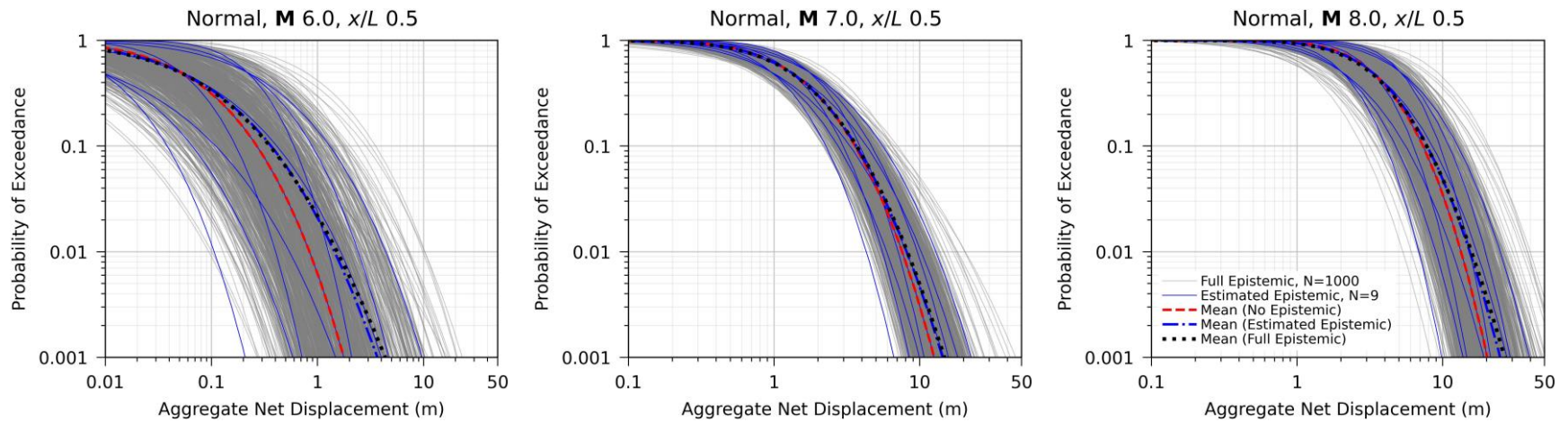


Figure 6.18. Comparison of KEA24 within-model epistemic uncertainty at rupture midpoints for normal events. Legend applies to all.

6.4 CEA25 MODEL

The CEA25 model provides alternative model coefficients based on the statistical uncertainty for the magnitude scaling breakpoint (m_b) in their model. Specifically, they provide correlated model coefficients for four magnitude breakpoints. Their preferred model places the breakpoint at M 7.1, and the three alternatives use breakpoints at M 6.4, 6.75, and 7.32. Recommendations on epistemic weighting for the alternatives are not provided by CEA25. In addition to alternatives for the nEMG distribution, the CEA25 team also developed models for using other statistical distributions (Chiou et al., 2023). The nEMG distribution is preferred by the CEA25 model developers and the others are not evaluated here.

Figures 6.19 and 6.20 compare the predictions from each alternative magnitude scaling model for the rupture endpoint ($x/L = 0$) and midpoint ($x/L = 0.5$), respectively, for M 6, 7, and 8 in the form of probability of exceedance curves. The impact of the different models varies by magnitude and is independent of location. Specifically, the smaller magnitude breakpoints produce higher hazard for larger magnitude events, and vice-versa. At the 99th percentile (i.e., a 10^{-2} probability of exceedance) the displacements in the different models vary by factors of about 1.25, 1.1, and 2.15 for M 6, 7, and 8, respectively.

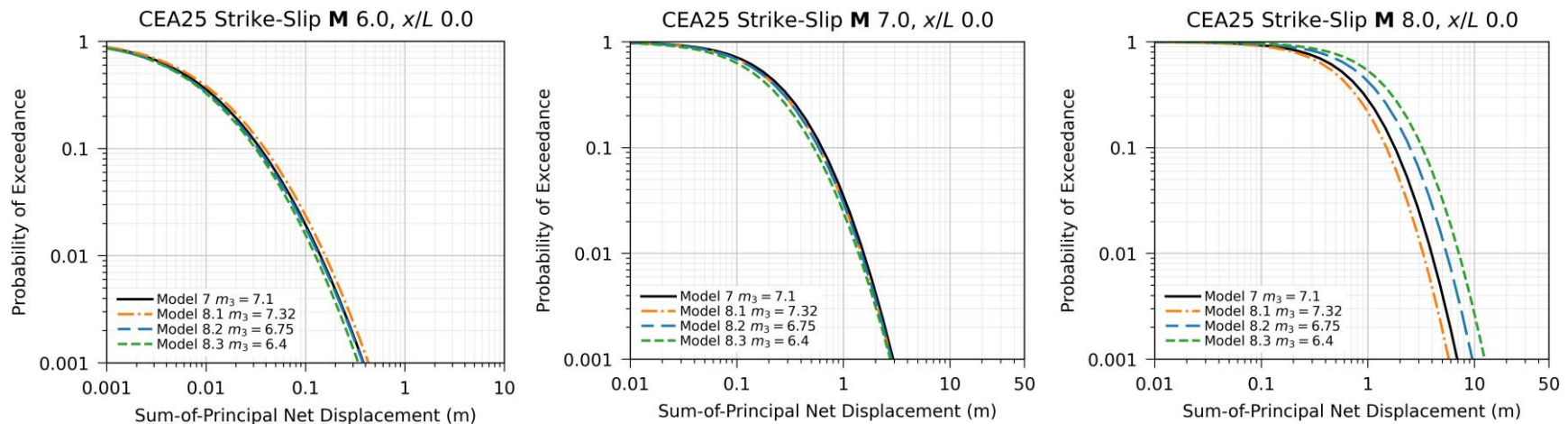


Figure 6.19. Comparison of CEA25 within-model epistemic uncertainty at rupture endpoints.

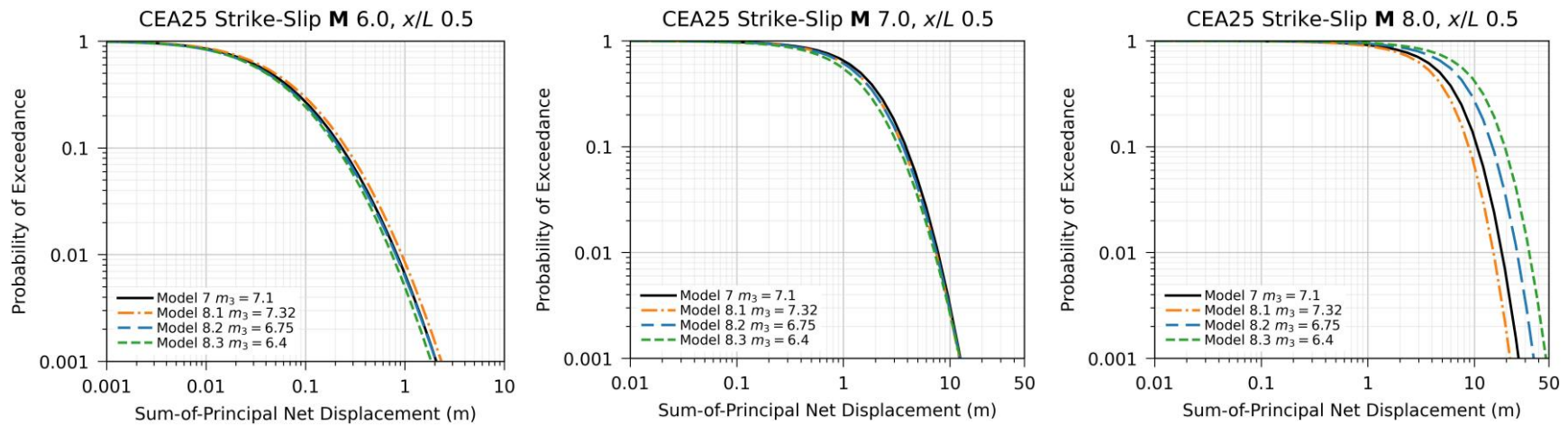


Figure 6.20. Comparison of CEA25 within-model epistemic uncertainty at rupture midpoints.

7 Summary

Four new fault displacement models (FDMs) were developed for principal ruptures through the FDHI Project. The models provide probability distributions for principal or aggregate displacement as a function of moment magnitude (M), normalized location along rupture length (x/L), and style of faulting. All models are applicable between M 6.0 and 8.0, where most of the empirical data exist, but some are applicable to lower or higher magnitudes. Two models are applicable to all styles of faulting (LA23 and KEA24), whereas the MEA24 and CEA25 models are applicable to reverse and strike-slip faulting, respectively. Additionally, a new surface rupture length model by Lavrentiadis et al. (2023) can be used to convert normalized rupture locations to absolute lengths for practical applications.

The new FDMs are a significant improvement over previously published models in several ways:

1. The models use a new, project-specific database developed from an extensive and systematic data quality review in coordination with the model developers. The use of a common and comprehensive database makes individual models more stable and comparisons between models more meaningful.
2. The models include magnitude scaling breakpoints to capture nonlinear magnitude scaling where supported by the data. Previously published models used loglinear scaling.
3. The aleatory variability modeling is significantly improved. For example, most new models partition the aleatory variability into between- and within-event components, which avoids bias towards better-sampled events. The aleatory variability models are magnitude- or x/L -dependent, which improves hazard estimates because data dispersion is not constant for all magnitudes or locations along the rupture. Non-lognormal statistical distributions are supported by the data and are used in all new models.
4. Upper-trail displacement predictions in the new models are in better agreement with empirical observations of maximum displacement, which is driven by a combination of an expanded database and improvements to the aleatory variability modeling and magnitude scaling in the FDHI models.
5. All new models provide methods to capture within-model epistemic uncertainty. The LA23 model estimates the statistical uncertainty on the median prediction. MEA24 provides

alternative coefficients for their magnitude scaling models, and they also offer two different x/L -dependent FDMs (which is a form of between-model epistemic uncertainty). KEA24 provides the full epistemic uncertainty in their model with the posterior distributions of the coefficients. The CEA25 model provides alternative coefficients based on different magnitude scaling models.

6. Finally, developing models through a coordinated research program allowed for extensive interaction and fruitful technical discussions between modeling teams and database developers that improved individual models and would otherwise be unavailable on an isolated team.

This report provides a comparison of the four new FDMs and four previously published FDMs. Model information and predictions are presented in several ways in this report to provide a comprehensive comparison of the FDMs. For example, tabulated summaries of the predictor variables and aleatory variability modeling are provided in Chapter 3. Predicted displacement profiles and magnitude scaling with average displacement are shown in Chapter 5. Maximum displacements are also addressed. Because the new models use different statistical distributions, aleatory variability is compared with probability functions and dot charts for specific percentiles in Chapter 5.5. A broad range of style, magnitude, and x/L scenarios are evaluated. The spread of the 5th/95th percentile predictions on the dot charts shows the relative size of the aleatory variability among the models. Probability of exceedance curves are also provided in Chapter 5.5 to show the results in hazard space. Finally, the impact of within-model epistemic uncertainty is evaluated in Chapter 6 for each new model with exceedance probability curves for a range of scenarios.

Each FDM consists of three key elements: (1) the prescribed shape of the median profile; (2) scaling of the displacement with magnitude; and (3) the aleatory variability model. These are technical decisions made by the model developers that lead to differences in the model results. For example, the end-of-rupture tapering in the profile shape can lead to significant differences in predictions within ~15% of the rupture endpoints. The nonlinear magnitude scaling in the new models for strike-slip and normal faulting leads to significantly lower median displacements at the magnitude extremes (i.e., M 5.0 and 8.5) relative to the previously published models that use loglinear scaling. All new FDMs use non-lognormal distributions with broad lower tails and narrow upper tails that lead to larger model-to-model variation at lower percentiles.

The median predictions among the new FDHI models are within a factor of about 2 for most styles, magnitudes, and x/L locations. For small magnitudes at the rupture endpoints, where data are sparse, the new models differ by up to a factor of about 6. The smallest differences correspond with styles and magnitudes that are best represented in the FDHI Database.

Improved aleatory variability modeling in the new FDMs captures the upper tails of the data distributions better than previously published models. For example, the 95th percentile prediction for M 8 at the rupture midpoint of a strike-slip fault is 40 m in the PEA11 model, but it

is only 15 m in KEA24. Upper-tail predictions for large magnitude reverse and normal events are also significantly smaller in the new models.

The new FDMs use different definitions of displacement (as elaborated in Chapter 2), and we recommend hazard analysts and other end-users carefully consider the definitions and related modeling assumptions when applying the new models. Methods for adjusting model results for different participating ruptures (i.e., aggregate, sum-of-principal, and single principal) are generally not available, and displacement vector decomposition is not provided in the new FDMs that predict net displacement. Models that predict net displacement may need to be adjusted for fault dip because the fault-normal and dip-slip components are systematically underreported in the FDHI Database. Parameters that are not captured in the metrics and definitions used by a specific model may need to be estimated in site-specific fault displacement hazard evaluations.

The four FDMs summarized in this report represent the state-of-the-art in fault displacement model development, and we anticipate widespread implementation of these models by hazard analysts. The comparisons in this report span a range of scenarios defined by style of faulting, magnitude, along-strike location, and percentile. While the range is sufficiently broad to provide end-users with an understanding of the performance of each model, it is not exhaustive, and some similarities and differences are obscured by the different definitions of displacement used in the models. We recommend hazard analysts evaluate the impact of the new models in their specific application.

REFERENCES

- Abrahamson, N., Atkinson, G., Boore, D., Bozorgnia, Y., Campbell, K., Chiou, B., Idriss, I., Silva, W., and Youngs, R. (2008). “Comparisons of the NGA ground-motion relations.” *Earthquake Spectra*, 24(1), 45–66.
- Al Atik, L. and Youngs, R. R. (2014). “Epistemic uncertainty for NGA-West2 models.” *Earthquake Spectra*, 30(3), 1301–1318.
- Biasi, G. P. and Weldon, R. J. (2006). “Estimating surface rupture length and magnitude of paleoearthquakes from point measurements of rupture displacement.” *Bulletin of the Seismological Society of America* 96(5): 1612–1623. DOI: 10.1785/0120040172.
- Bonilla, M. G., Mark, R. K., and Lienkaemper, J. J. (1984). “Statistical relations among earthquake magnitude, surface rupture length, and surface fault displacement.” *Bulletin of the Seismological Society of America* 74(6), 2379–2411.
- Chiou, B., Chen, R., Thomas, K., Milliner, C., Dawson, T., and Petersen, M. D. (in review). “Fault displacement model for surface principal rupture of strike-slip faults.” *Earthquake Spectra*.
- Chiou, B. S.-J., Chen, R., Thomas, K., Milliner, C. W. D., Dawson, T., and Petersen, M. D. (2023). “Surface Fault Displacement Models for Strike-Slip Faults.” Report No. GIRS-2022-07, Revision in progress, *The B. John Garrick Institute for the Risk Sciences at UCLA Engineering*, <<https://www.risksciences.ucla.edu/girs-reports/2022/07>>.
- Coppersmith, K. and Youngs, R. (2000). “Data needs for probabilistic fault displacement hazard analysis.” *Journal of Geodynamics*, 29(3-5), 329–343.
- Gregor, N., Abrahamson, N. A., Atkinson, G. M., Boore, D. M., Bozorgnia, Y., Campbell, K.W., Chiou, B. S.-J., Idriss, I., Kamai, R., Seyhan, E., et al. (2014). “Comparison of NGA-West2 GMPEs.” *Earthquake Spectra*, 30(3), 1179–1197.
- Gregor, N., Addo, K., Abrahamson, N. A., Al Atik, L., Atkinson, G. M., Boore, D. M., Bozorgnia, Y., Campbell, K.W., Chiou, B. S., Gürlerce, Z., et al. (2022). “Comparisons of the NGA-subduction ground motion models.” *Earthquake Spectra*, 38(4), 2580–2610.

- Hemphill-Haley, M. A. and Weldon, R. J. (1999). "Estimating prehistoric earthquake magnitude from point measurements of surface rupture." *Bulletin of the Seismological Society of America*, 89(5), 1264–1279.
- Keefer, D. L. and Bodily, S. E. (1983). "Three-point approximations for continuous random variables." *Management Science*, 29(5), 595–609.
- Kuehn, N. M., Kottke, A. R., Sarmiento, A. C., Madugo, C. M., and Bozorgnia, Y. (2024). "A fault displacement model based on the FDHI database." *Earthquake Spectra*. Epub ahead of print. DOI: 10.1177/87552930241291077.
- Kuehn, N., Kottke, A., Madugo, C., Sarmiento, A., and Bozorgnia, Y. (2022). "UCLA-PG&E Fault Displacement Model." Report No. GIRS-2022-06, Revision in progress, *The B. John Garrick Institute for the Risk Sciences at UCLA Engineering*, <<https://www.risksciences.ucla.edu/girs-reports/2022/06>>.
- Lavrentiadis, G. and Abrahamson, N. (2023). "Fault-displacement models for aggregate and principal displacements." *Earthquake Spectra*. Epub ahead of print, <<https://doi.org/10.1177/87552930231201531>>.
- Lavrentiadis, G. and Abrahamson, N. (2019). "Generation of surface-slip profiles in the wavenumber domain." *Bulletin of the Seismological Society of America*, 109(3), 888-907.
- Lavrentiadis, G., Abrahamson, N., and Sarmiento, A. (2024). Event coordinate system for surface fault rupture: Release v0.1. Zenodo, <<https://doi.org/10.5281/zenodo.12610853>>.
- Lavrentiadis, G., Wang, Y., Abrahamson, N. A., Bozorgnia, Y., and Goulet, C. (2023). "A Seismologically Consistent Surface Rupture Length Model for Unbounded and Width-Limited Events." *Earthquake Spectra*. Epub ahead of print, <<https://doi.org/10.1177/87552930231205871>>.
- Manighetti, I., Perrin, C., Gaudemer, Y., Dominguez, S., Stewart, N., Malavieille, J., and Garambois, S. (2020). "Repeated giant earthquakes on the Wairarapa fault, New Zealand, revealed by Lidar-based paleoseismology." *Scientific Reports*, 10(1), 2124.
- Manighetti, I., Campillo, M., Sammis, C., Mai, P. M., and King, G. (2005). "Evidence for self-similar, triangular slip distributions on earthquakes: Implications for earthquake and fault mechanics." *Journal of Geophysical Research: Solid Earth*, 110(B5).
- McCalpin, J. P. and Slemmons, D. B. (1998). "Statistics of Paleoseismic Data: Final Technical Report Submitted to US Geological Survey." Report No. USGS-NEHRP Contract 1434-HQ-96-GR-02752, GEO-HAZ Consulting, Inc.
- Moss, R. E. S., Thompson, S. C., Kuo, C.-H., Younesi, K., and Baumont, D. (2024). "New probabilistic fault displacement hazard models for reverse faulting." *Earthquake Spectra*. Epub ahead of print. DOI: 10.1177/87552930241288560.

- Moss, R., Thompson, S., Kuo, C.-H., Younesi, K., and Baumont, D. (2022). “Reverse Fault PFDHA.” Report No. GIRS-2022-05, Revised 17 January 2024, *The B. John Garrick Institute for the Risk Sciences at UCLA Engineering*, <<https://www.risksciences.ucla.edu/girs-reports/2022/05>>.
- Moss, R. E. S. and Ross, Z. E. (2011). “Probabilistic Fault Displacement Hazard Analysis for Reverse Faults.” *Bulletin of the Seismological Society of America*, 101(4), 1542–1553.
- Petersen, M. D., Dawson, T. E., Chen, R., Cao, T., Wills, C. J., Schwartz, D. P., and Frankel, A. D. (2011). “Fault displacement hazard for strike-slip faults.” *Bulletin of the Seismological Society of America*, 101(2), 805–825.
- Sarmiento, A., Lavrentiadis, G., Bozorgnia, Y., Chen, R., Chiou, B., Dawson, T., Kottke, A., Kuehn, N., Madugo, C., Moss, R., Thompson, S., and Zandieh, A. (in review). “Comparisons of FDHI fault displacement models for principal and aggregate displacement.” *Earthquake Spectra*.
- Sarmiento, A., Madugo, D., Bozorgnia, Y., Shen, A., Mazzoni, S., Lavrentiadis, G., Dawson, T., Madugo, C., Kottke, A., Thompson, S., Baize, S., Milliner, C., Nurminen, F., Boncio, P., and Visini, F. (2021). “Fault Displacement Hazard Initiative Database.” Report No. GIRS-2021-08, Revision 3.3 dated 29 May 2024, *The B. John Garrick Institute for the Risk Sciences at UCLA Engineering*, <<https://www.risksciences.ucla.edu/girs-reports/2021/08>>.
- Spudich, P. and Chiou, B. (2015). “Strike-Parallel and Strike-Normal Coordinate System Around Geometrically Complicated Rupture Traces – Use by NGA-West2 and Further Improvements.” Report No. OFR 2015-1028, US Department of the Interior, *US Geological Survey*.
- Stepp, J. C., Wong, I., Whitney, J., Quittmeyer, R., Abrahamson, N., Toro, G., Youngs, R., Coppersmith, K., Savy, J., Sullivan, T., and Yucca Mountain PSHA Project Members (2001). “Probabilistic seismic hazard analyses for ground motions and fault displacement at Yucca Mountain, Nevada.” *Earthquake Spectra*, 17(1), 113–151.
- Takao, M., Tsuchiyama, J., Annaka, T., and Kurita, T. (2013). “Application of probabilistic fault displacement hazard analysis in Japan.” *Journal of Japan Association for Earthquake Engineering* 13: 17–36. DOI: 10.5610/jaee.13.17.
- Takao, M., Kaneto, T., and Kurita, T. (2018). “Outline of the PFDHA method and recent studies on PFDHA in Japan.” In: *Best Practices in Physics-based Fault Rupture Models for Seismic Hazard Assessment of Nuclear Installations*, Cadarache-Château, France, 14-16 May 2018.
- Thomas, K., Milliner, C. W., Chen, R., Chiou, B. S.-J., Dawson, T., and Petersen, M. D. (2024). “Least Cost Path Analysis as an Objective and Automated Method to Define the Primary

Fault Trace for Probabilistic Fault Displacement Hazard Analysis.” *Earthquake Spectra*. Epub ahead of print, <<https://doi.org/10.1177/87552930231205878>>.

Valentini, A., Fukushima, Y., Contri, P., Ono, M., Sakai, T., Thompson, S. C., Viallet, E., Annaka, T., Chen, R., Moss, R. E., et al. (2021). “Probabilistic fault displacement hazard assessment (PFDHA) for nuclear installations according to IAEA safety standards.” *Bulletin of the Seismological Society of America*, 111(5), 2661–2672.

Wells, D. L. and Coppersmith, K. J. (1994). “New empirical relationships among magnitude, rupture length, rupture width, rupture area, and surface displacements.” *Bulletin of the Seismological Society of America*, 84(4), 974–1002.

Wells, D. L. and Coppersmith, K. J. (1993). “Likelihood of surface rupture as a function of magnitude.” *Seismological Research Letters*, 64(1), 54.

Wesnousky, S. G. (2008). “Displacement and geometrical characteristics of earthquake surface ruptures: Issues and implications for seismic-hazard analysis and the process of earthquake rupture.” *Bulletin of the Seismological Society of America*, 98(4), 1609–1632.

Youngs, R. R., Arabasz, W. J., Anderson, R. E., Ramelli, A. R., Ake, J. P., Slemmons, D. B., McCalpin, J. P., Doser, D. I., Fridrich, C. J., Swan, F. H., Rogers, A. M., Yount, J. C., Anderson, L. W., Smith, K. D., Bruhn, R. L., Knuepfer, P. L. K., Smith, R. B., DePolo, C. M., O’Leary, D. W., Coppersmith, K. J., Pezzopane, S. K., Schwartz, D. P., Whitney, J. W., Olig, S. S., and Toro, G. R. (2003). “A Methodology for Probabilistic Fault Displacement Hazard Analysis (PFDHA).” *Earthquake Spectra*, 19(1), 191–219.

Appendix A:

Preliminary Comparisons of Results from Different Displacement Summation Approaches

1 Introduction

This Appendix documents the results of an FDHI Working Group tasked with understanding the impact of different displacement summation methodologies. Three of the four new FDHI models (KEA24, CEA25, and LA23) predict displacements summed across multiple (sub)parallel ruptures. Summed displacements were considered to be a more stable metric by some developers to better account for displacement on complex surface rupture patterns that are not captured in the modeling. All three models use a summation approach that accounts for irregular spacing of displacement measurement sites. Each team (KEA24, CEA25, and LA23) used their own method to sum the displacements based on data in the FDHI Database.

The CEA25 model sums displacements on principal ruptures, which is abbreviated D_{sp} in this Appendix. The KEA24 model sums displacements across principal and distributed ruptures, which is referred to as *aggregate* displacement and is abbreviated D_{agg} . The LA23 model provides formulations for both D_{sp} and D_{agg} .

The KEA24 model applies a custom algorithm that computes an aggregated displacement value for each principal measurement in the database (referred to as “seed” measurement herein), using an hourglass-shaped search window and linearly interpolating displacements on the same rupture. The LA23 model computes the summed displacements on a segment basis. They used geologic judgment to determine key rupture segments and applies the ECS algorithm to create a Segment Coordinate System (SCS) for each key segment. The SCS ordinates are used to identify (sub)parallel ruptures, and the displacements on each (sub)parallel rupture are linearly interpolated at the location of interest and summed. The CEA25 model sums principal displacements based on geologic judgment and limited linear interpolation between measurement sites. More information on the summation approach used in each model can be found in the accompanying reports and journal publications cited in the main report.

A Working Group convened in early 2021 to review different summation approaches by evaluating data from six earthquakes:

- 1992 **M** 7.28 Landers, California (FDHI EQ_ID =1)
- 1999 **M** 7.13 Hector Mine, California (FDHI EQ_ID =2)
- 1987 **M** 6.54 Superstition Hills, California (FDHI EQ_ID =8)
- 2019 **M** 6.4 Ridgecrest-1, California (FDHI EQ_ID =42)

- 2019 M 7.1 Ridgecrest-2, California (FDHI EQ_ID =43)
- 1995 M 7.0 Neftegorsk, Russia (FDHI EQ_ID =65)

These events were selected to capture a range of surface rupture complexity (i.e., overlapping or parallel segments) and measurement site density and spacing. All are strike-slip earthquakes because the CEA25 model did not consider dip-slip events. Section 2 of this Appendix presents the plots and discussion for each event, and the Section 3 provides summarizes the results.

2 Evaluations

The results from the evaluations for each earthquake (Landers, Hector Mine, Superstition Hills, Ridgecrest-1, Ridgecrest-2, and Neftegorsk) are presented separately below. Four figures were used to qualitatively compare aggregate or sum-of-principal results from different modeling teams for each event. The first figure shows the spatial distribution and amplitude of observations (measurement sites) from the FDHI Database. The observations are color-coded based on classification or rank (i.e., cumulative, principal, or distributed). Marginal density plots are shown for each model to visually compare the spatial distribution and amplitude of displacements between each model. Although natural log transformations are not used in the new models, the observations span a broad range, so the y-axis uses natural log units to improve readability. In the second figure, aggregate or sum-of-principal values for the same "seed" measurement site are compared directly on pair plots with 1:1 identity lines. The third figure shows model-to-model differences between aggregate or sum-of-principal values (in natural log units) with surface rupture maps to better understand how differences relate to rupture patterns. The last figure presents seed-to-summed log ratios as a function of seed displacement understand how aggregate or sum-of-principal amplitude depends on seed amplitude.

Results from a new wide-aperture fault displacement model (i.e., discrete displacement and inelastic deformation) by Milliner et al. (2020 and in prep.)¹ were also available to the Working Group for several of the events considered in this Appendix. For the purposes of this discussion, the wide-aperture results are omitted from the plots because the displacements include continuous deformation components such as warping and thus are not equivalent to the aggregate or sum-of-principal values in the other models.

¹ Milliner, C., Avouac, J.-P., Chen, R., Aati, S., Chiou, B., Donnellan, A., Dawson, T., Madugo, C., and Dolan, J. F. (2020). "Development of a geodetic-based probabilistic fault displacement hazard analysis using near-field geodetic imaging data." *AGU Fall Meeting Abstracts*, Vol. 2020, T042–07.

2.1 LANDERS

The 1992 M 7.28 Landers, California event was selected because it is a complex and well-documented event in the FDHI Database. Additionally, preliminary results from a new dynamic rupture model validation study by Wang and Goulet (2021)² were available.

The results of the SCEC simulations (Wang and Goulet, 2021) are shown on Figure A.1. Their results are provided with uniform spacing along the rupture; accordingly, the results are not readily correlated with the FDHI Database measurement sites and are therefore omitted from the other plots.

The marginal density plot (Figure A.1) shows strong agreement in the spatial distribution of measurements along the rupture length (top axis), suggesting the different summation approaches do not significantly down-sample the number of measurements. (An exception is the SCEC model, which provides uniformly-sampled locations.) The displacement amplitude densities for the KEA, CEA, and SCEC models are in good agreement. The LA results are generally similar but show more contribution from smaller values (right axis).

Generalized model comparisons can be made from the pair plots (Figure A.2) and are consistent with the trends in the displacement density plots. For example, the KEA and CEA values are generally higher than the comparable LA values (i.e., D_{agg} and D_{sp} , respectively).

Visual inspection of the differences in values between models as a function of mapped ruptures (Figure A.3) reveals the largest differences are spatially associated with rupture complexity. The results are consistent with the pair plots; for example, values in the KEA and CEA models are generally higher than in the comparable LA model.

The seed-to-summed log ratios (Figure A.4) reveal some consistent trends. The ratios decrease as the seed (single-site measurement) increases. We infer this is due to a combination of spatial concentration of displacement for larger displacements (i.e., less complex rupture patterns) and the (numerically) relatively reduced effect of including smaller, distributed displacements. Additionally, the KEA ratios are systematically lower than the others, which we infer is due to inclusion of more distributed displacements and the use of an hourglass-shaped search window.

² Wang, Y., and Goulet, C. (2021). "Validation of fault displacements from dynamic rupture simulations against the observations from the 1992 Landers earthquake." *Bulletin of the Seismological Society of America*, 111(5), 2574-2594.

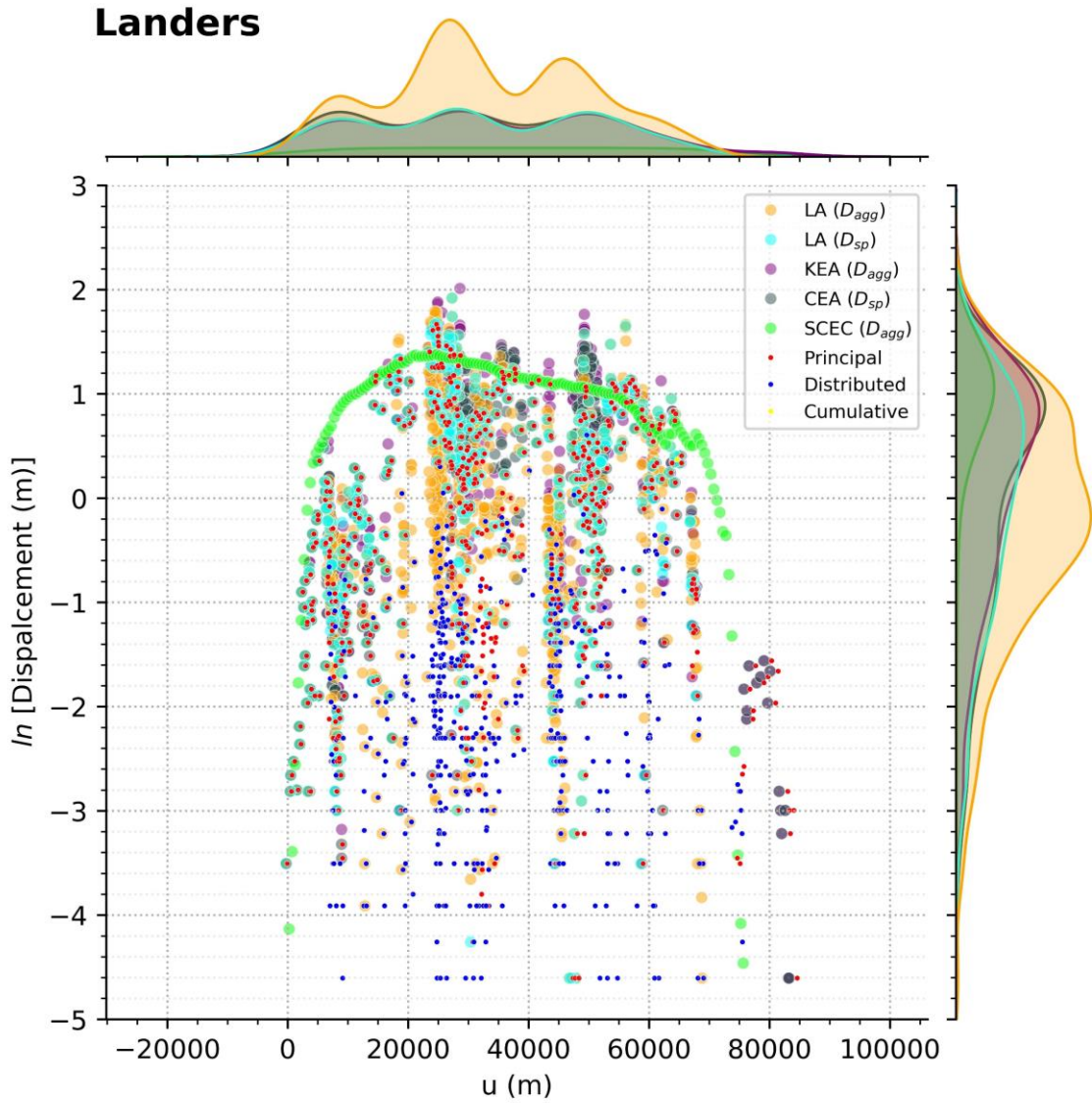


Figure A.1. Displacement measurements (Cumulative, Principal, and Distributed rank) from FDHI Database for 1992 M 7.28 Landers, California (FDHI EQ_ID =1) earthquake and summed displacements from KEA24, CEA25, and LA23 models. Marginal density plots shown for each model.

Landers, Displacement (m)

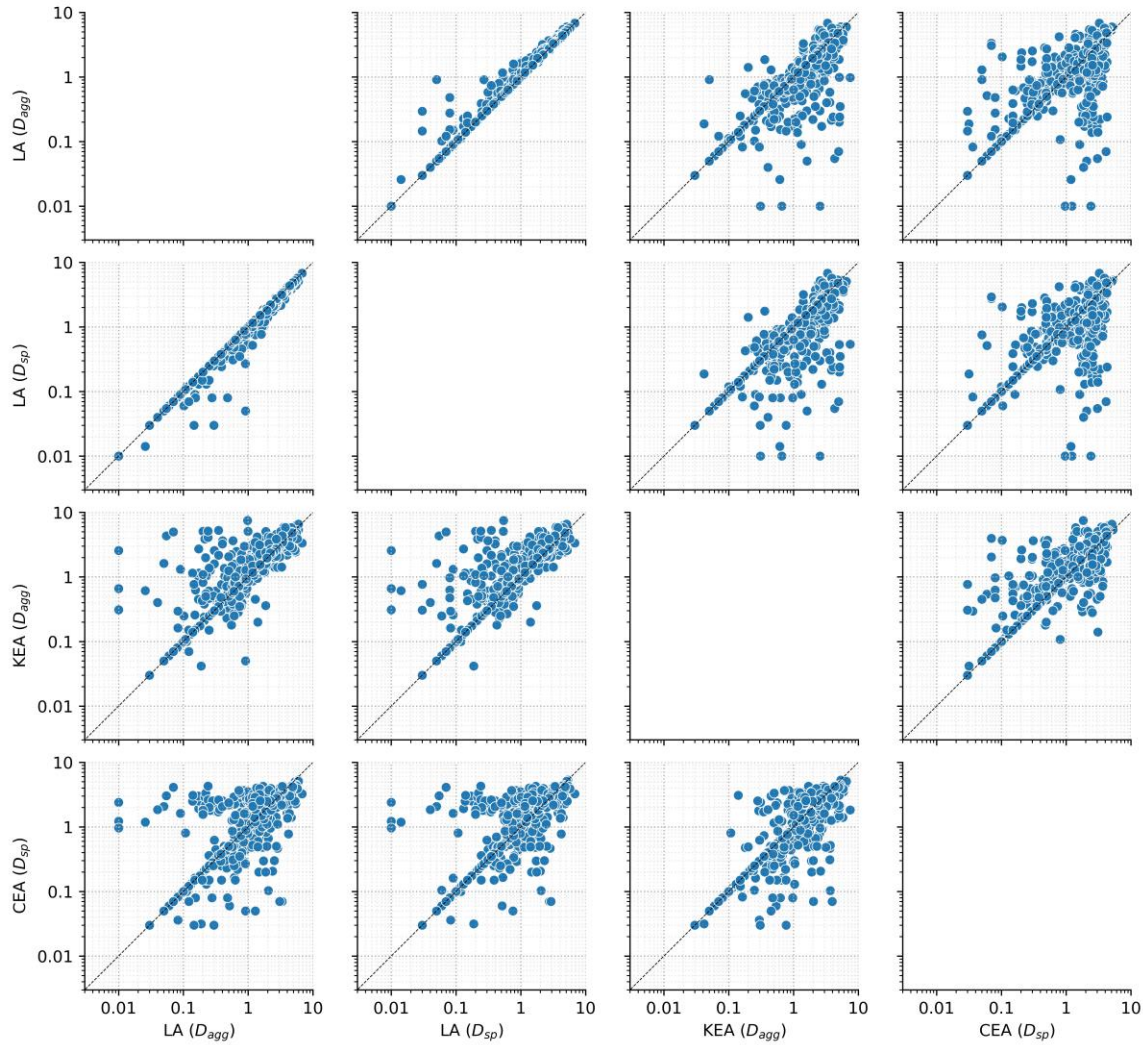


Figure A.2. Comparison of summed displacement results for each model (KEA24, CEA25, and LA23) based on measurement site for 1992 M 7.28 Landers, California earthquake.

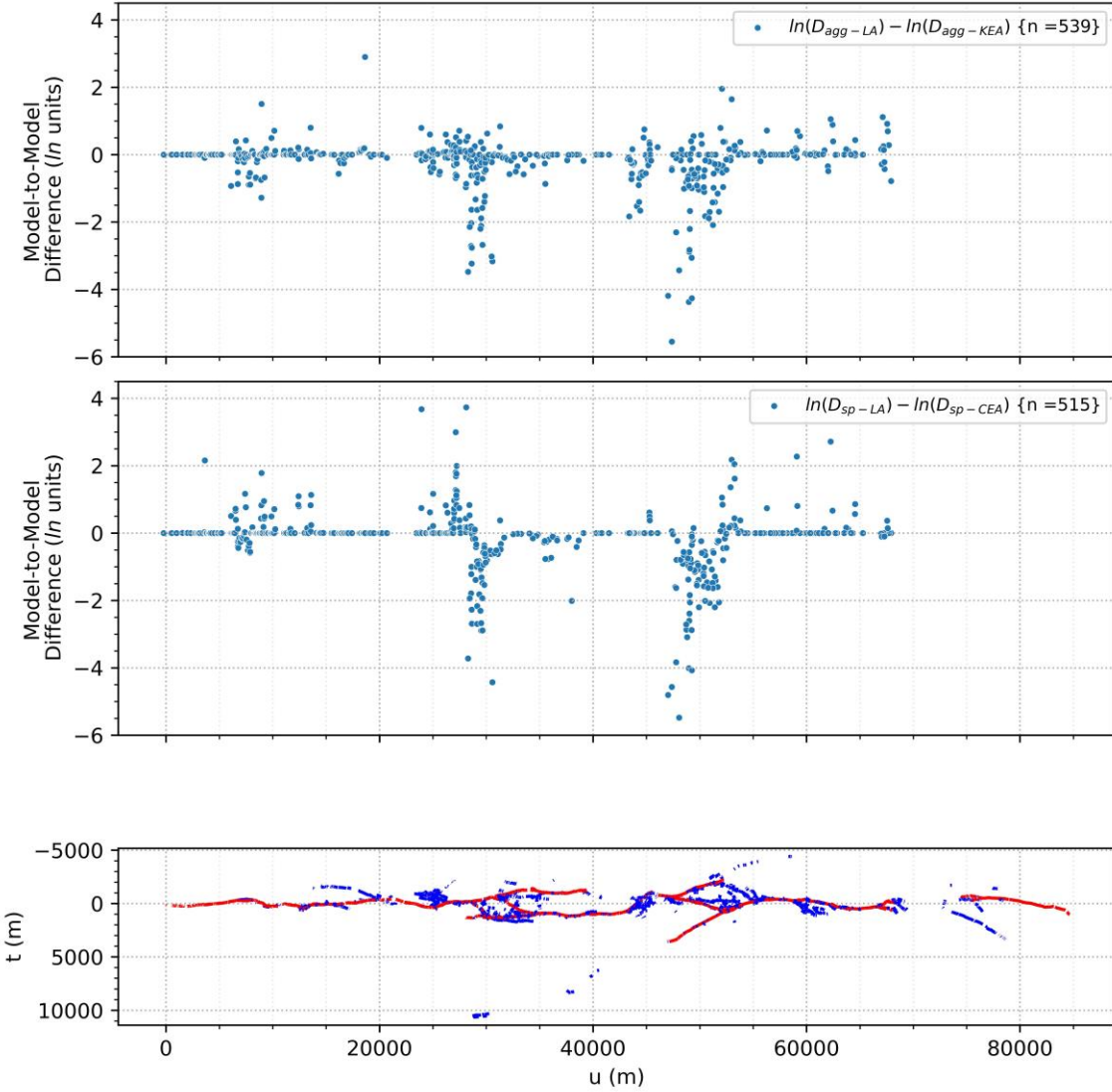


Figure A.3. Comparison of summed displacement results for D_{agg} and D_{sp} among the models as a function of rupture length for 1992 M 7.28 Landers, California earthquake. Principal (red) and distributed (blue) ruptures shown in projected (ECS) coordinates in bottom panel.

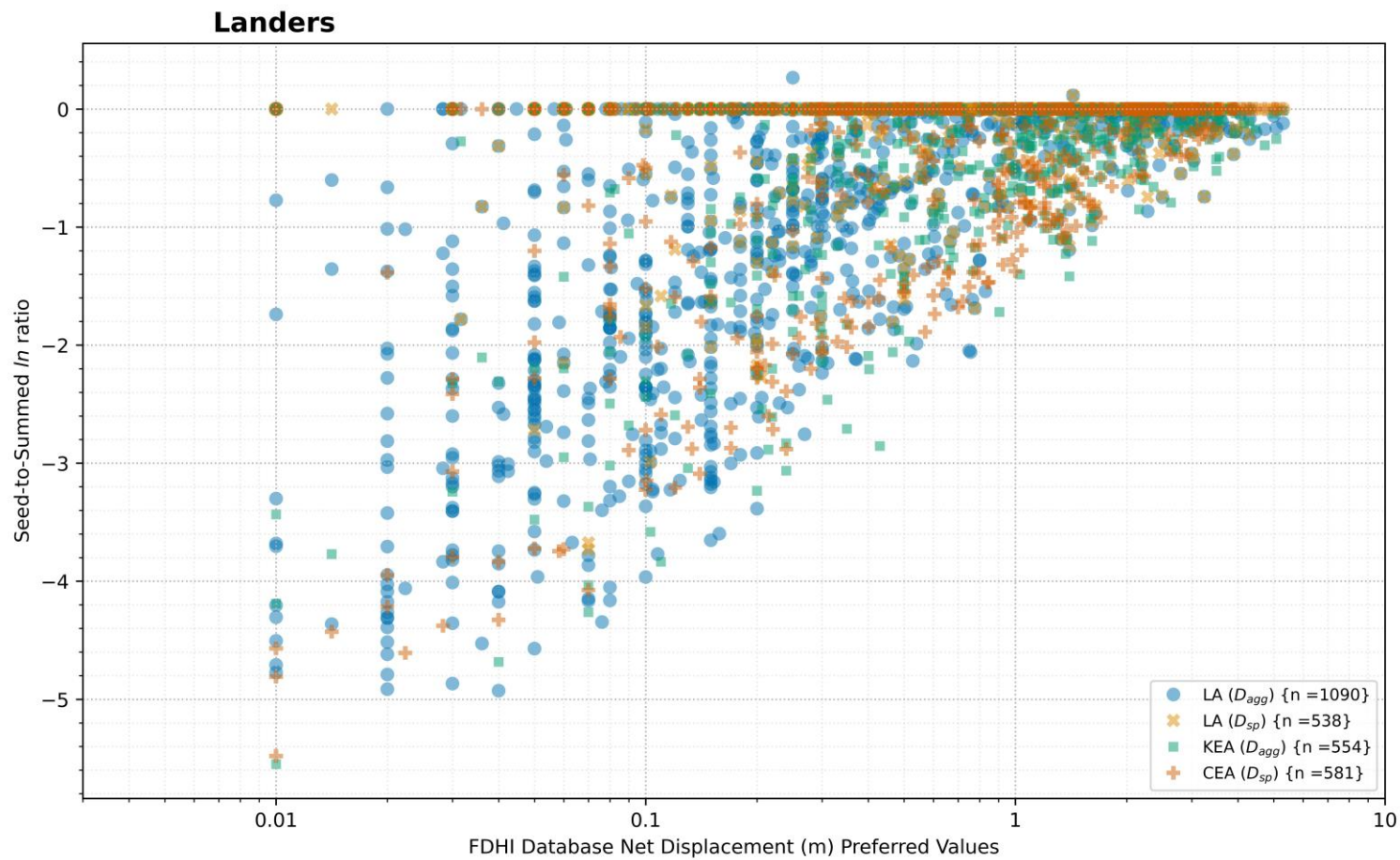


Figure A.4. Comparison of summed displacement results for each model (KEA24, CEA25, and LA23) as a function of seed measurement for 1992 M 7.28 Landers, California earthquake.

2.2 HECTOR MINE

The 1999 M 7.13 Hector Mine, California event was selected because it is a well-documented event with some rupture complexity. Additionally, Dr. Beth Arcos from Wood, PLC provided sum-of-principal results for this event based on a manual geologic assessment performed for the California High Speed Rail (HSR) project.

The marginal density plot (Figure A.5) shows strong agreement in the spatial distribution of measurements along the rupture length for the KEA and LA models (top axis). The CEA and HSR models have more contribution from the southern end of the rupture (larger u -axis values) because both teams treated the Mesquite Lake Fault as a principal rupture. This is a technically defensible alternative interpretation of the rankings in the FDHI Database. The displacement amplitude densities are in strong agreement for all models. The HSR results show a slightly higher contribution from smaller values is due to treating the Mesquite Lake Fault as a principal rupture. Over a dozen measurements are available on this fault and they are all relatively low, which affects the displacement amplitude density distribution.

Generalized model comparisons can be made from the pair plots (Figure A.6) and are consistent with the trends in the displacement density plots. For example, the KEA, CEA, and HSR values are systematically higher than the comparable LA values (i.e., D_{agg} or D_{sp}). The HSR results are generally higher than the CEA and LA results.

Visual inspection of the differences in values between models as a function of mapped ruptures (Figure A.7) reveals the largest differences are spatially associated with principal rupture complexity (particularly the bifurcation of the Bullion Fault near $u = 34,000$). Other key differences are at the southern end of the rupture ($u > 40,000$) where the CEA and HSR models treated the Mesquite Lake Fault as a principal rupture and therefore have more measurements in this area. The results are consistent with the pair plots; for example, values in the HSR model are systematically higher than the CEA and LA models.

The seed-to-summed log ratios (Figure A.8) reveal some consistent trends. The ratios decrease as the seed (single-site measurement) increases. Additionally, the KEA ratios are generally lower than the others. Both of these trends were observed for the Landers evaluation and are discussed in more detail at the end of Section 2.1.

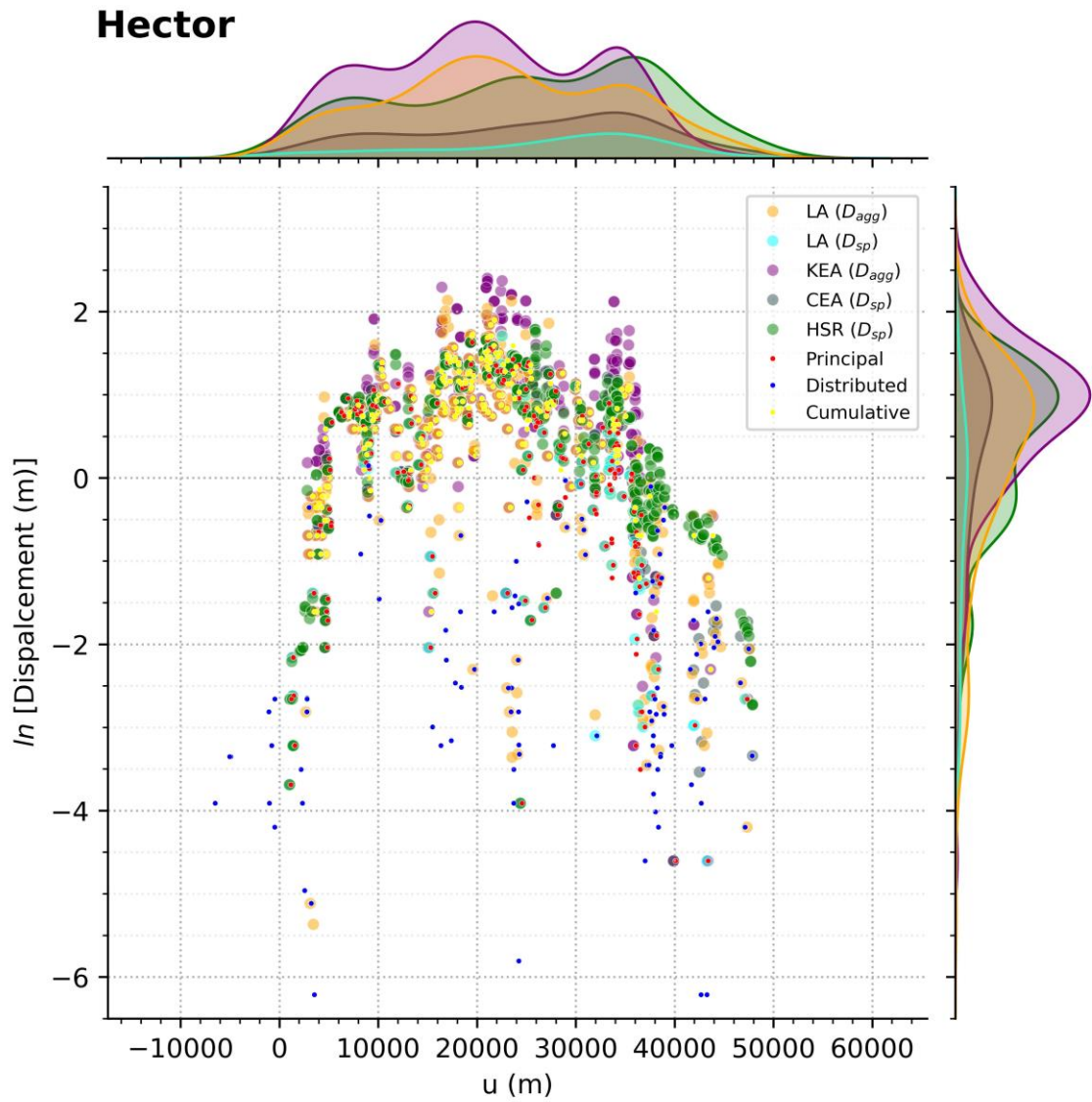


Figure A.5. Displacement measurements (Cumulative, Principal, and Distributed rank) from FDHI Database for 1999 M 7.13 Hector Mine, California (FDHI EQ_ID =2) earthquake and summed displacements from KEA24, CEA25, and LA23 models. Marginal density plots shown for each model.

Hector, Displacement (m)

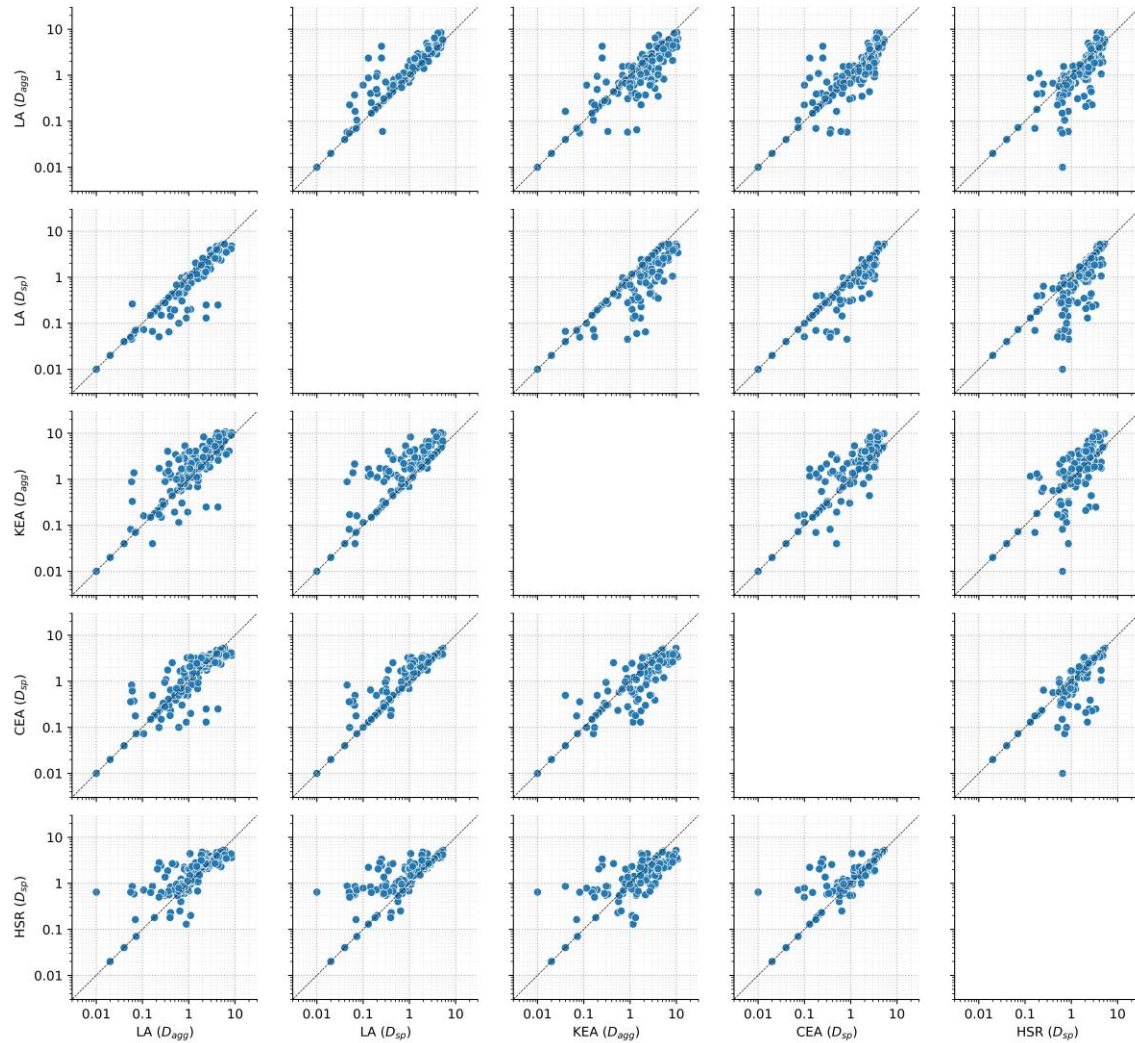


Figure A.6. Comparison of summed displacement results for each model (KEA24, CEA25, and LA23) based on measurement site for 1999 M 7.13 Hector Mine, California earthquake.

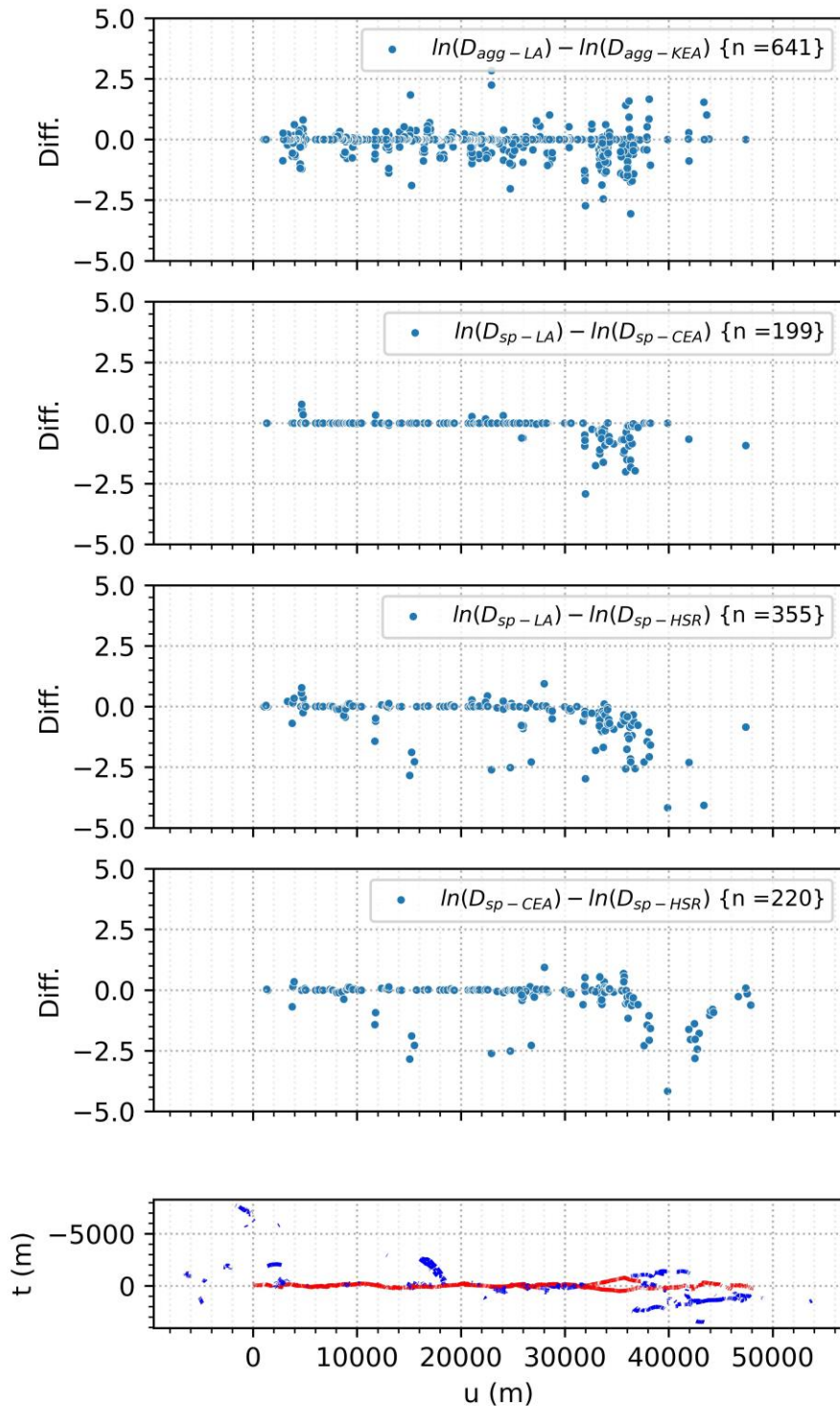


Figure A.7. Comparison of summed displacement results for D_{agg} and D_{sp} among the models as a function of rupture length for 1999 M 7.13 Hector Mine, California earthquake. Principal (red) and distributed (blue) ruptures shown in projected (ECS) coordinates in bottom panel.

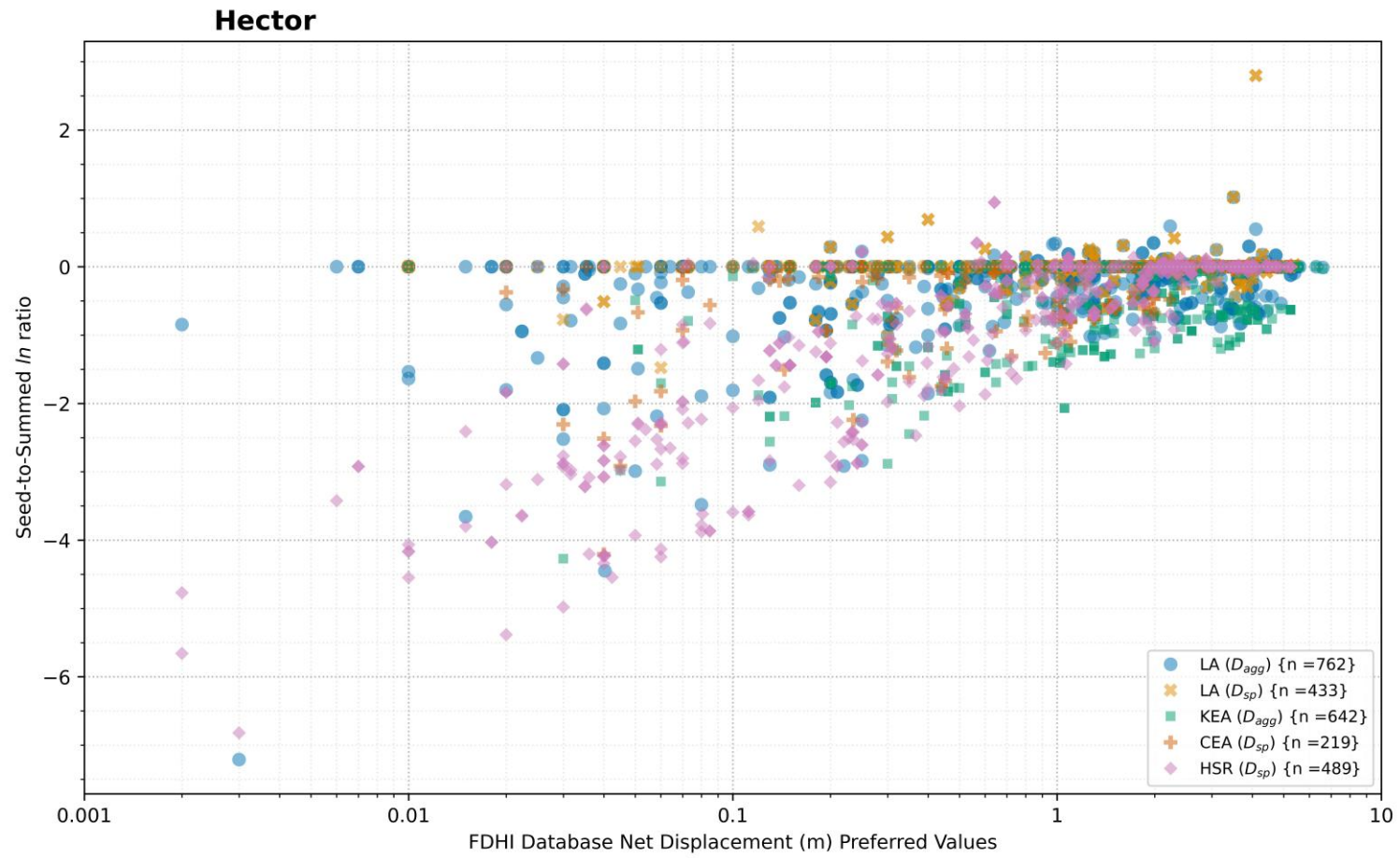


Figure A.8. Comparison of summed displacement results for each model (KEA24, CEA25, and LA23) as a function of seed measurement for 1999 M 7.13 Hector Mine, California earthquake.

2.3 SUPERSTITION HILLS

The 1987 M 6.54 Superstition Hills, California event was selected because it is a well-documented event with relatively simple but multi-stranded ruptures.

The marginal density plot (Figure A.9) shows strong agreement in the spatial distribution of measurements along the rupture length for the KEA, CEA, and LA D_{sp} models. Differences in the LA D_{agg} model, relative to KEA, spatially correspond with areas containing distributed displacements and are likely due to choices in the interpolation approach for incorporating distributed displacement measurements. The displacement amplitude densities are in strong agreement for all models.

Generalized model comparisons can be made from the pair plots (Figure A.10) and are consistent with the trends in the displacement density plots. For example, most of the values fall on the 1:1 equality line for each comparison. Where they differ, the CEA results are generally higher than the LA and KEA results for both D_{agg} and D_{sp} , and the LA D_{agg} results are generally higher than KEA.

Visual inspection of the differences in values between models as a function of mapped ruptures (Figure A.11) reveals that the largest differences are spatially associated with rupture complexity, particularly at the southern end of the rupture ($u > 21,000$). Consistent with the pair plots, the CEA results are higher than LA, and LA is higher than KEA, in the few areas where differences occur.

The seed-to-summed log ratios (Figure A.12) reveal some consistent trends. The ratios decrease as the seed (single-site measurement) increases (as observed for other events; see discussion at the end of Section 2.1). The LA ratios are generally lower than the others.

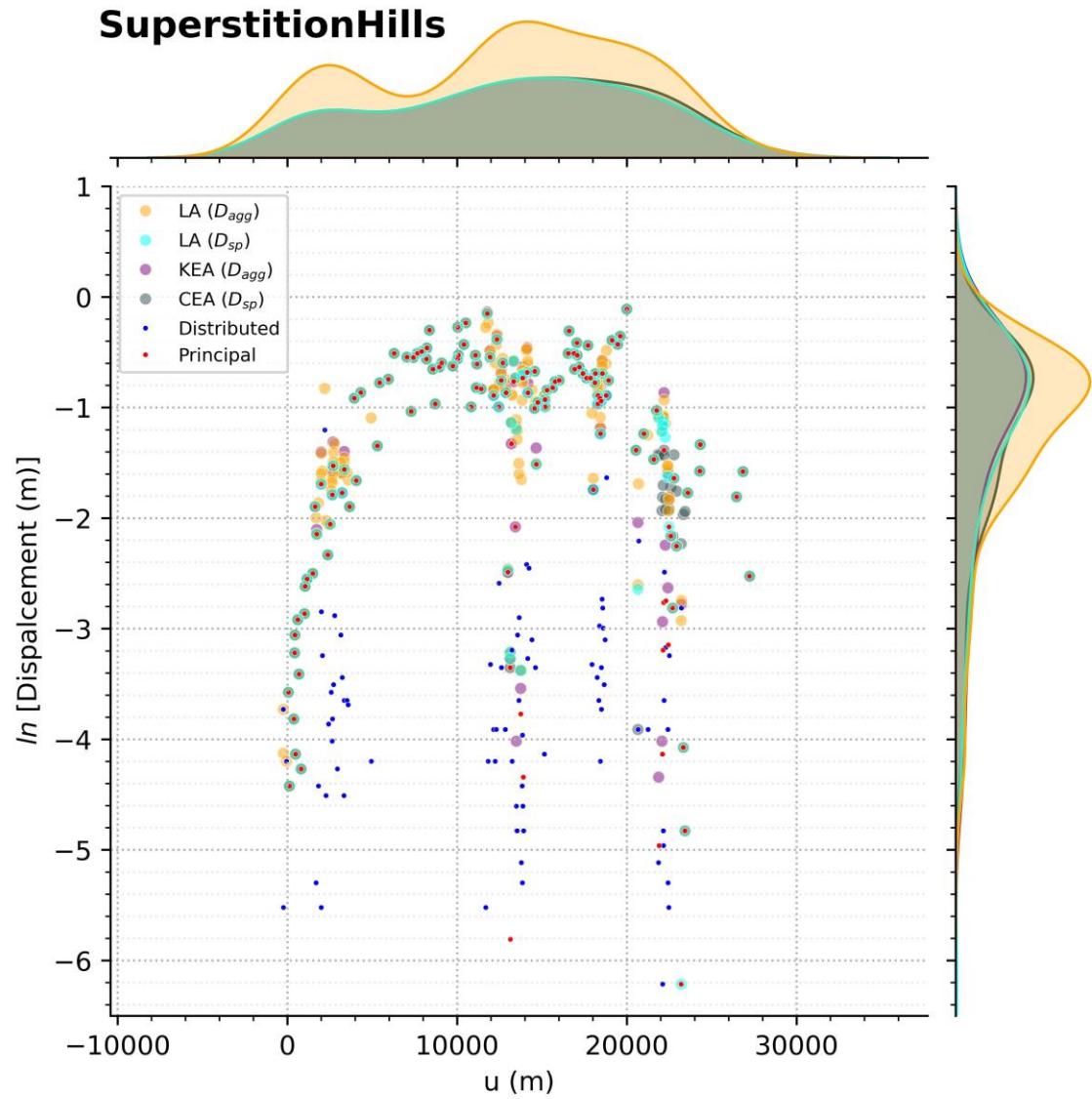


Figure A.9. Displacement measurements (Cumulative, Principal, and Distributed rank) from FDHI Database for 1987 M 6.54 Superstition Hills, California (FDHI EQ_ID =8) earthquake and summed displacements from KEA24, CEA25, and LA23 models. Marginal density plots shown for each model.

SuperstitionHills, Displacement (m)

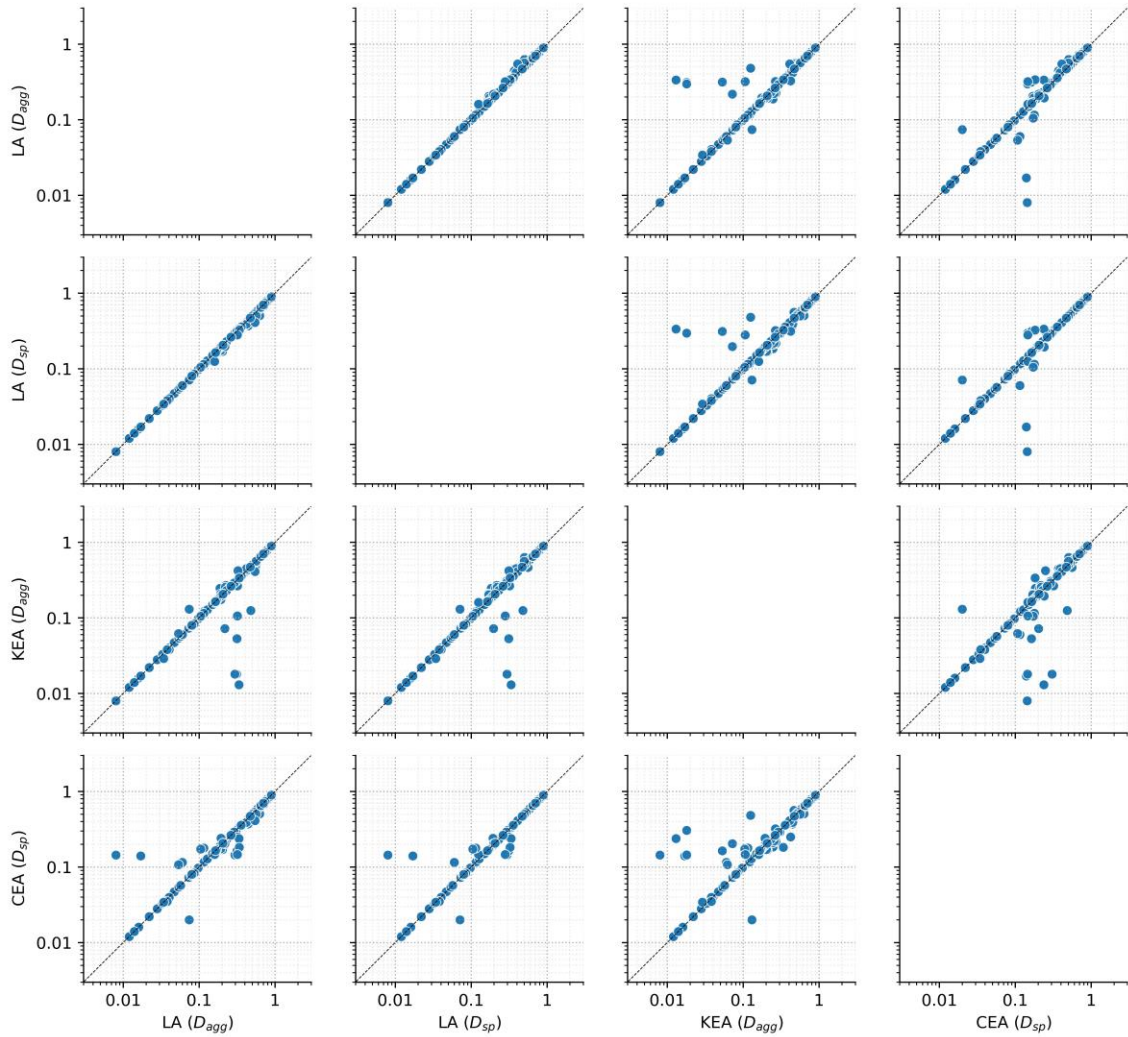


Figure A.10. Comparison of summed displacement results for each model (KEA24, CEA25, and LA23) based on measurement site for 1987 M 6.54 Superstition Hills, California earthquake.

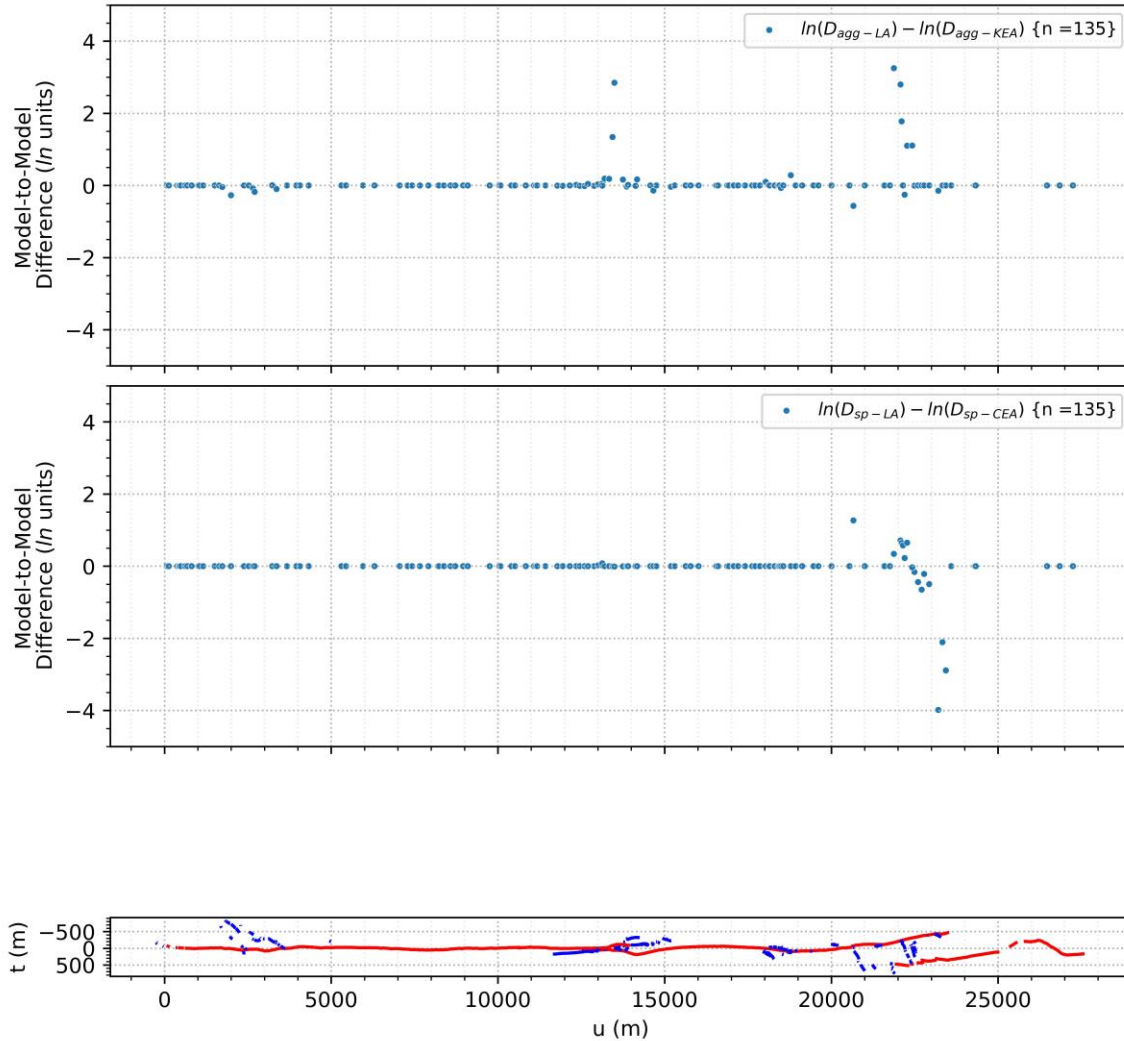


Figure A.11. Comparison of summed displacement results for D_{agg} and D_{sp} among the models as a function of rupture length for 1987 M 6.54 Superstition Hills, California earthquake. Principal (red) and distributed (blue) ruptures shown in projected (ECS) coordinates in bottom panel.

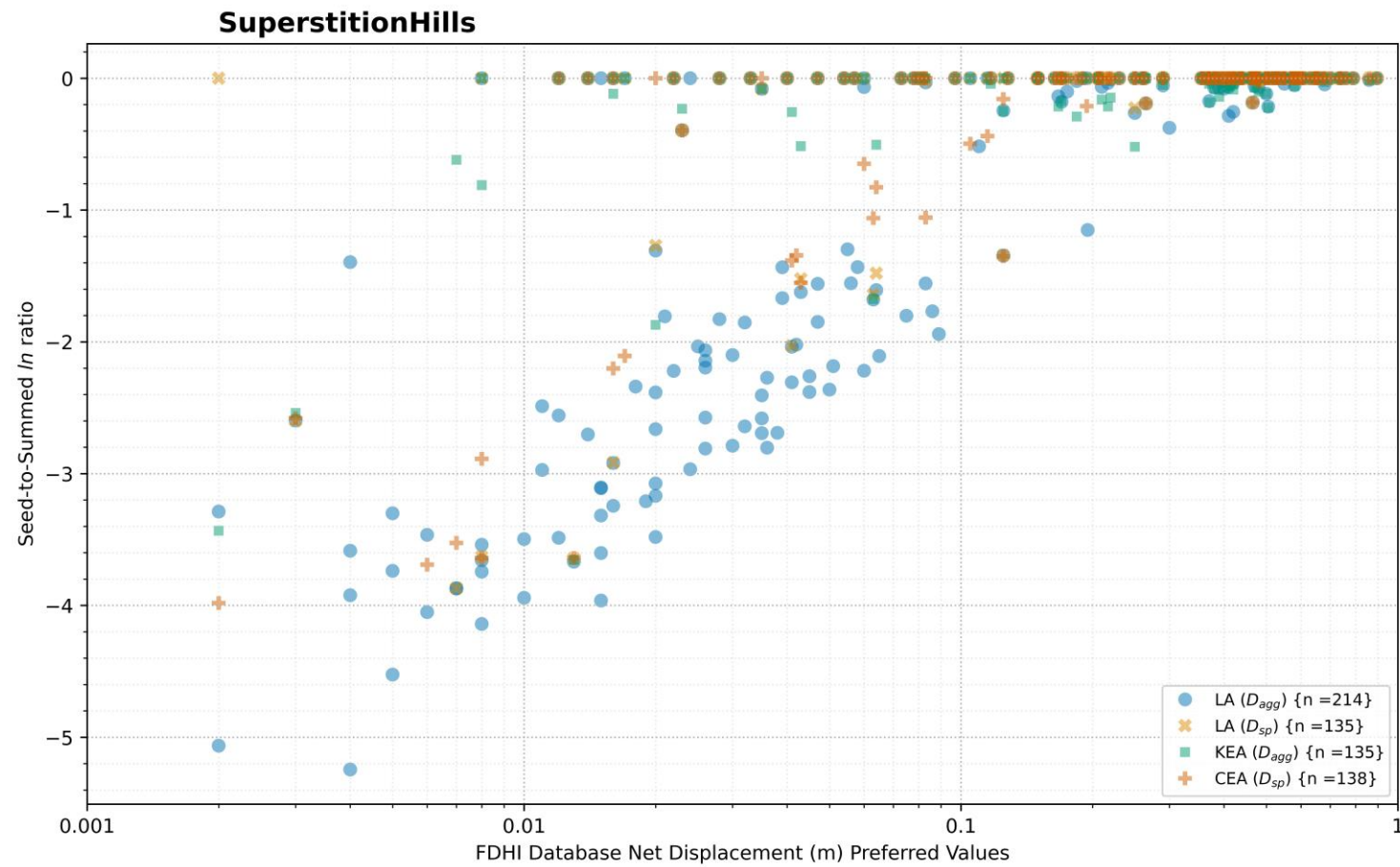


Figure A.12. Comparison of summed displacement results for each model (KEA24, CEA25, and LA23) as a function of seed measurement for 1987 M 6.54 Superstition Hills, California earthquake.

2.4 RIDGECREST-1

The 2019 M 6.4 Ridgecrest-1, California event was selected because it is a well-documented event.

The marginal density plot (Figure A.13) shows strong agreement in the spatial distribution of measurements along the rupture length for all models. The displacement amplitude densities span a broad range in all models and are in reasonable agreement.

Generalized model comparisons can be made from the pair plots (Figure A.14) and are consistent with the trends in the displacement density plots. Most of the values fall on the 1:1 equality line for each comparison. Where they differ, the LA D_{agg} results are slightly higher than KEA, and the CEA results are generally higher than the LA and KEA results for both D_{agg} and D_{sp} . CEA treated some of the northern ruptures as principal instead of distributed, which is a technically defensible alternative interpretation of the rankings in the FDHI Database. We infer that their approach for linear interpolation between measurement sites is contributing to the differences because both the KEA and LA models include distributed measurements.

Visual inspection of the differences in values between models as a function of mapped ruptures (Figure A.15) reveals the largest differences are spatially associated with the northeast reach of the rupture ($u < 2,500$), where the CEA model treated some of the ruptures as principal instead of distributed.

The seed-to-summed log ratios (Figure A.16) reveal some consistent trends. The ratios decrease as the seed (single-site measurement) increases (as observed for other events; see discussion at the end of Section 2.1). The KEA and CEA ratios are generally lower than the LA ratios.

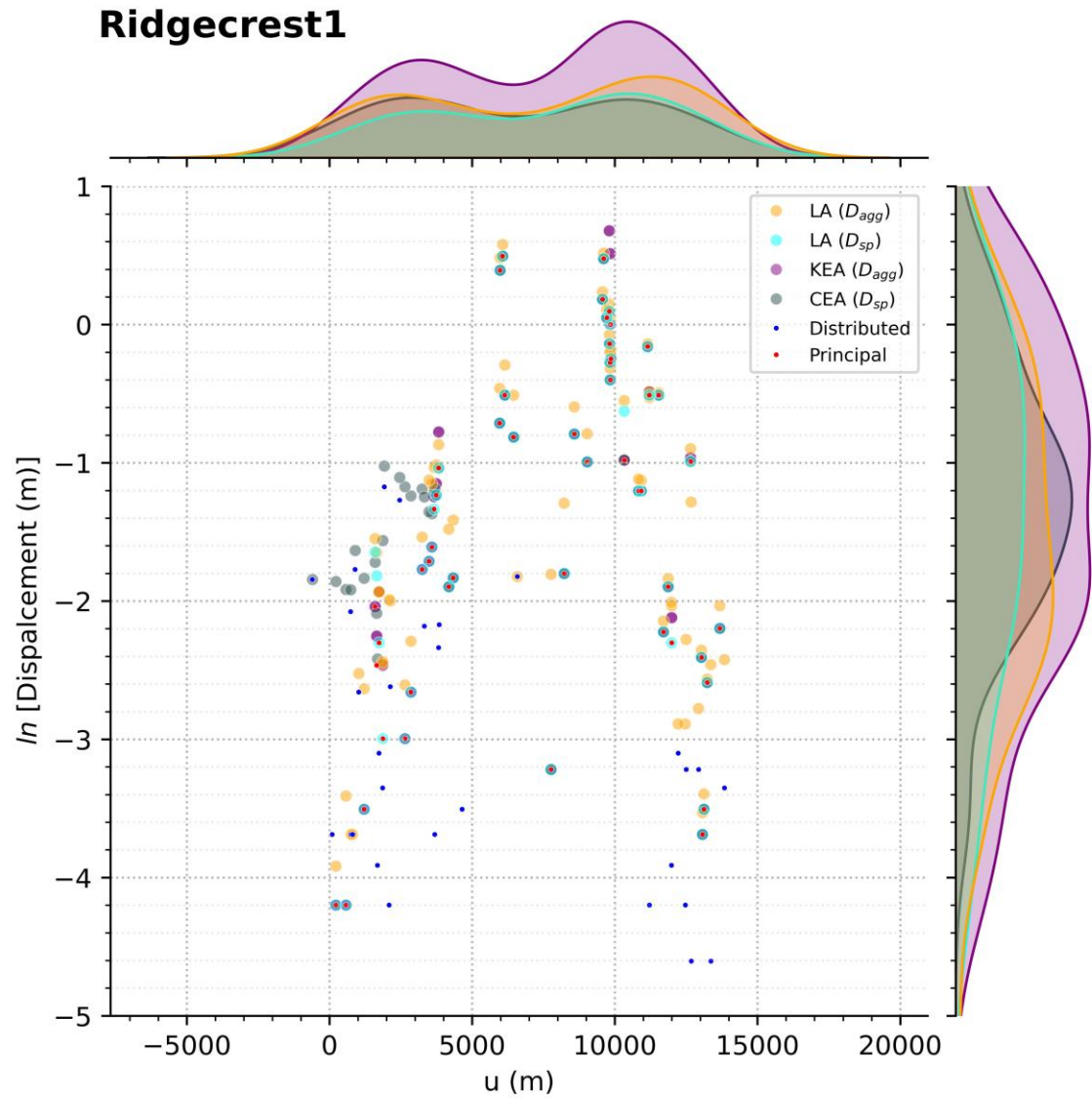


Figure A.13. Displacement measurements (Cumulative, Principal, and Distributed rank) from FDHI Database for 2019 M 6.4 Ridgecrest-1, California (FDHI EQ_ID =42) earthquake and summed displacements from KEA24, CEA25, and LA23 models. Marginal density plots shown for each model.

Ridgecrest1, Displacement (m)

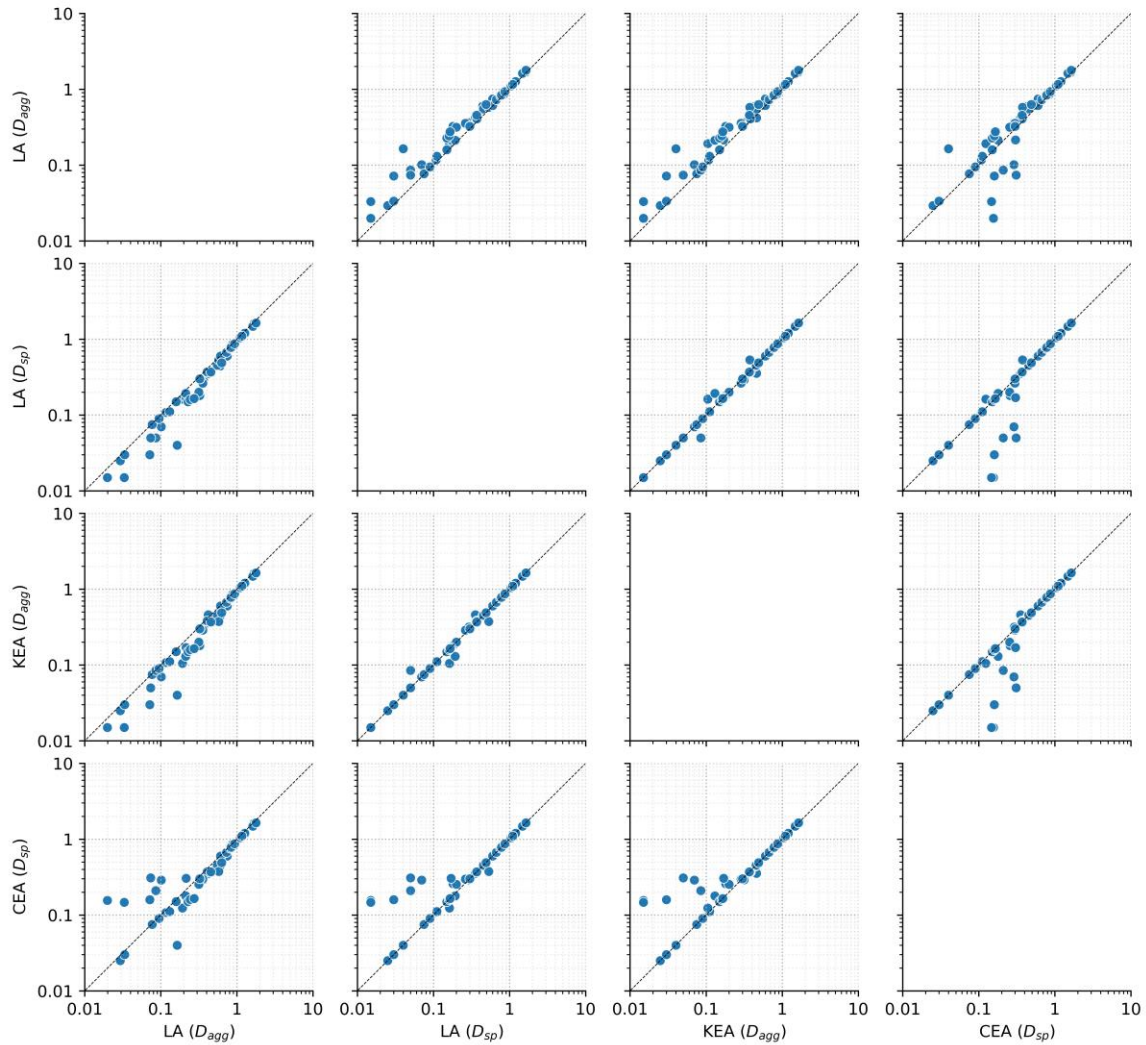


Figure A.14. Comparison of summed displacement results for each model (KEA24, CEA25, and LA23) based on measurement site for 2019 M 6.4 Ridgecrest-1, California earthquake.

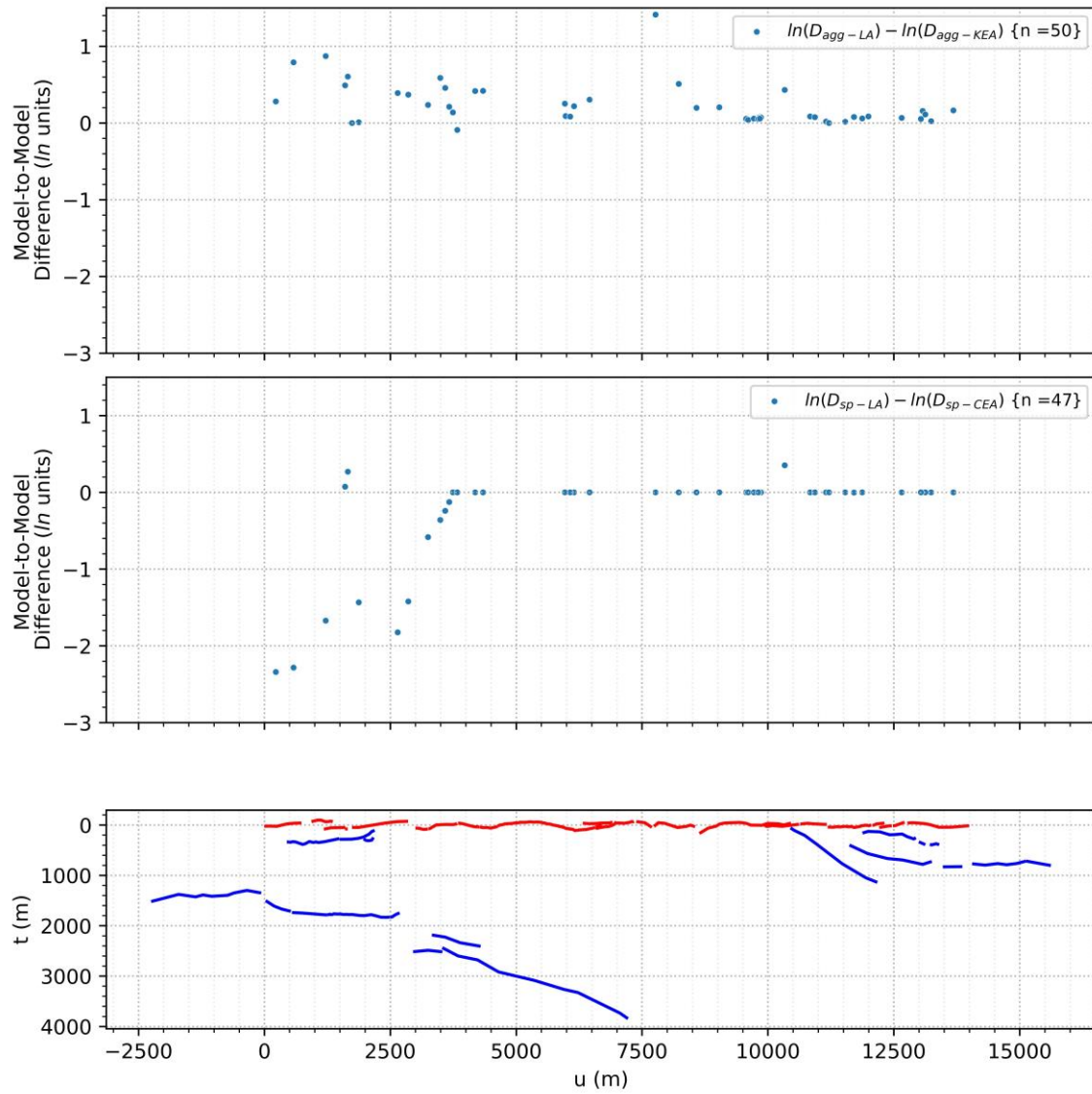


Figure A.15. Comparison of summed displacement results for D_{agg} and D_{sp} among the models as a function of rupture length for 2019 M 6.4 Ridgecrest-1, California earthquake. Principal (red) and distributed (blue) ruptures shown in projected (ECS) coordinates in bottom panel.

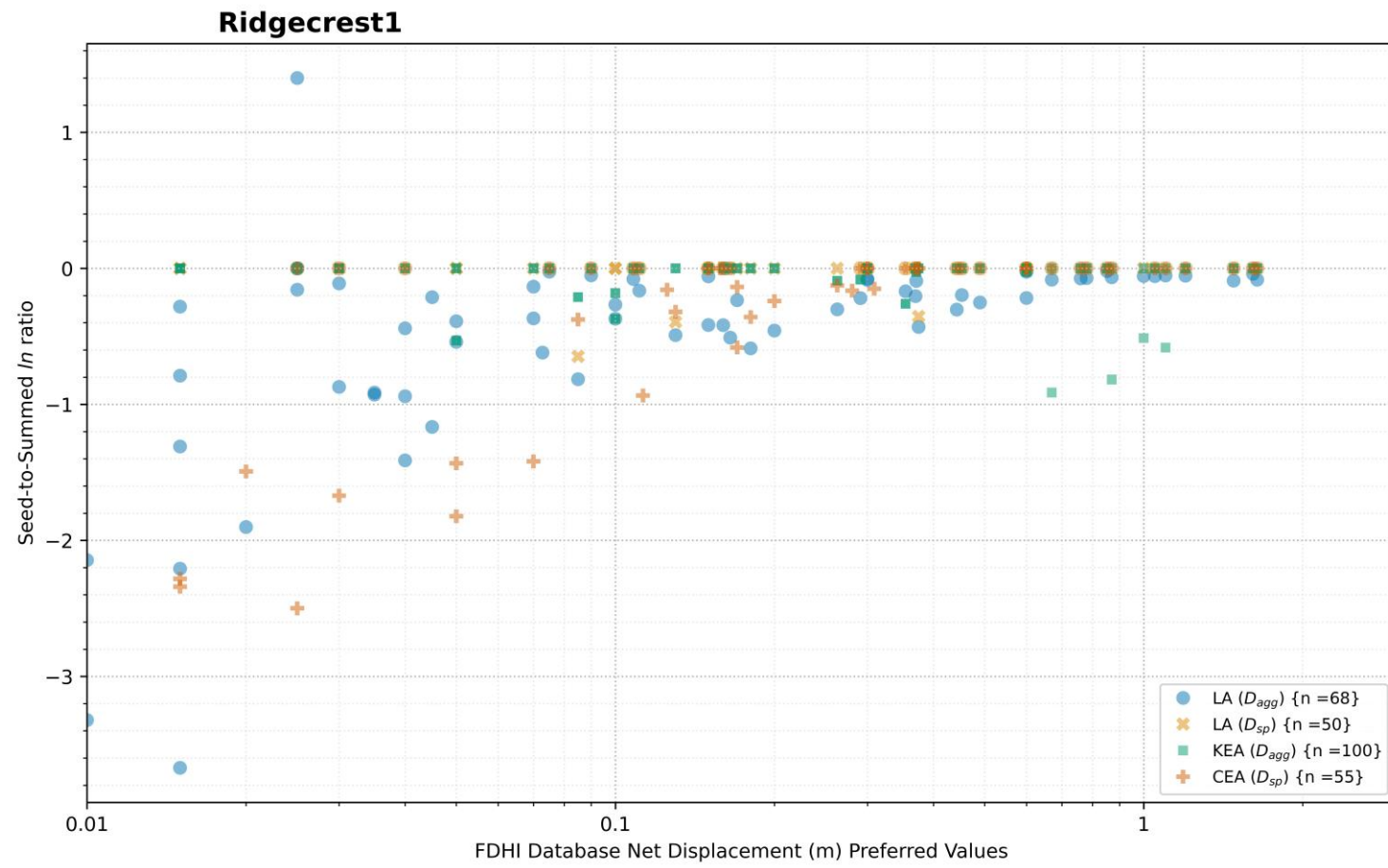


Figure A.16. Comparison of summed displacement results for each model (KEA24, CEA25, and LA23) as a function of seed measurement for 2019 M 6.4 Ridgecrest-1, California earthquake.

2.5 RIDGECREST-2

The 2019 M 7.1 Ridgecrest-2, California event was selected because it is a well-documented event with multi-stranded ruptures.

The marginal density plot (Figure A.17) shows good agreement in the spatial distribution of measurements along the rupture length for all models. Differences in the LA D_{agg} model, relative to KEA, spatially correspond with areas containing distributed displacements and are likely due to choices in the interpolation approach for incorporating distributed displacement measurements. The displacement amplitude densities are in strong agreement for all models. The results of the pair plots (Figure A.18) are in very strong agreement, with most of the values falling on the 1:1 equality line for each comparison.

Visual inspection of the differences in values between models as a function of mapped ruptures (Figure A.19) reveals the largest differences are spatially associated with increased rupture complexity. However, the overall differences are minor, consistent with the plots on Figures A.17 and A.18.

The seed-to-summed log ratios (Figure A.20) reveal some consistent trends. The ratios decrease as the seed (single-site measurement) increases (as observed for other events; see discussion at the end of Section 2.1). The CEA and LA ratios are generally lower than the KEA ratios.

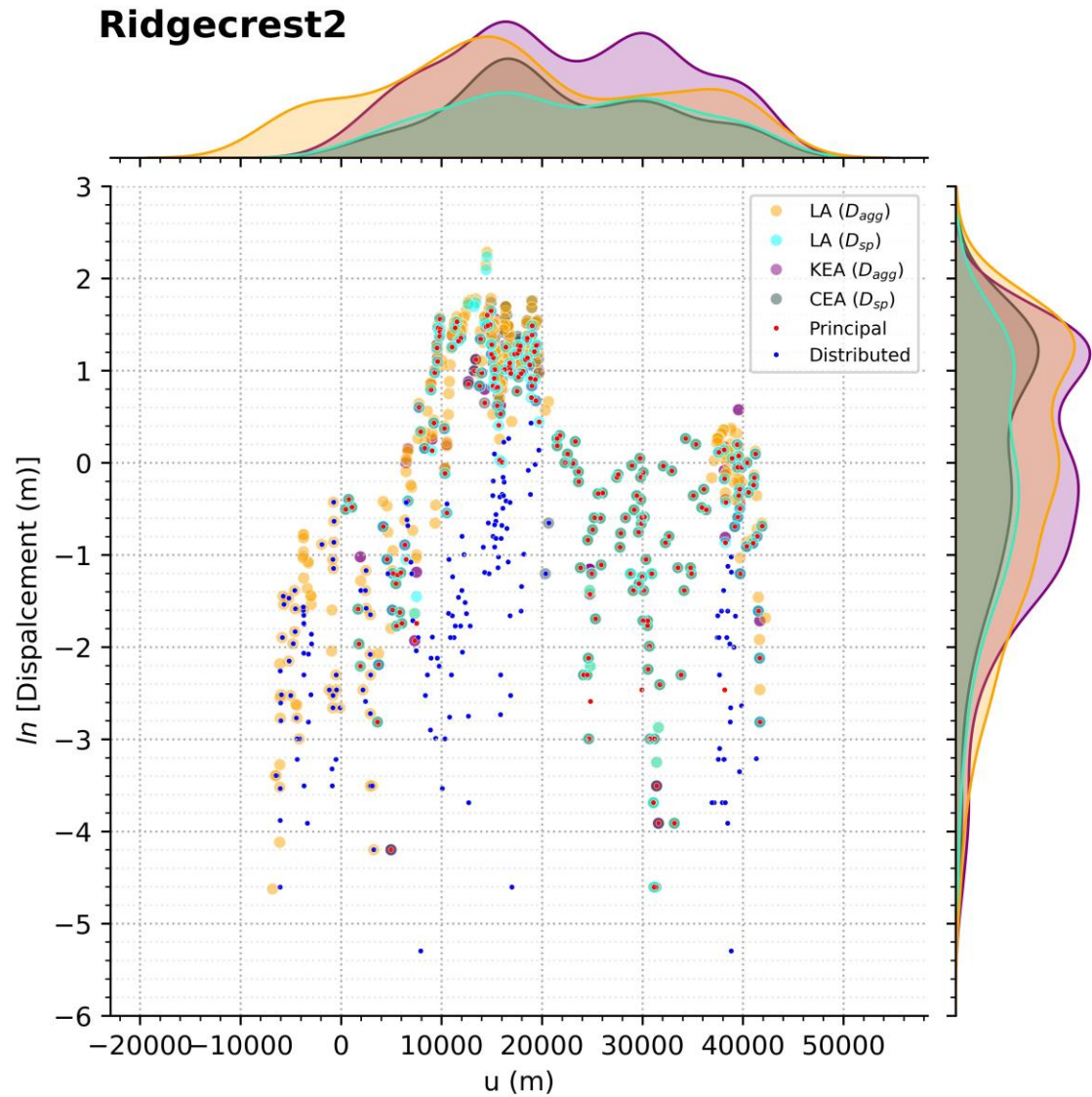


Figure A.17. Displacement measurements (Cumulative, Principal, and Distributed rank) from FDHI Database for 2019 M 7.1 Ridgecerest-2, California (FDHI EQ_ID =43) earthquake and summed displacements from KEA24, CEA25, and LA23 models. Marginal density plots shown for each model.

Ridgecrest2, Displacement (m)

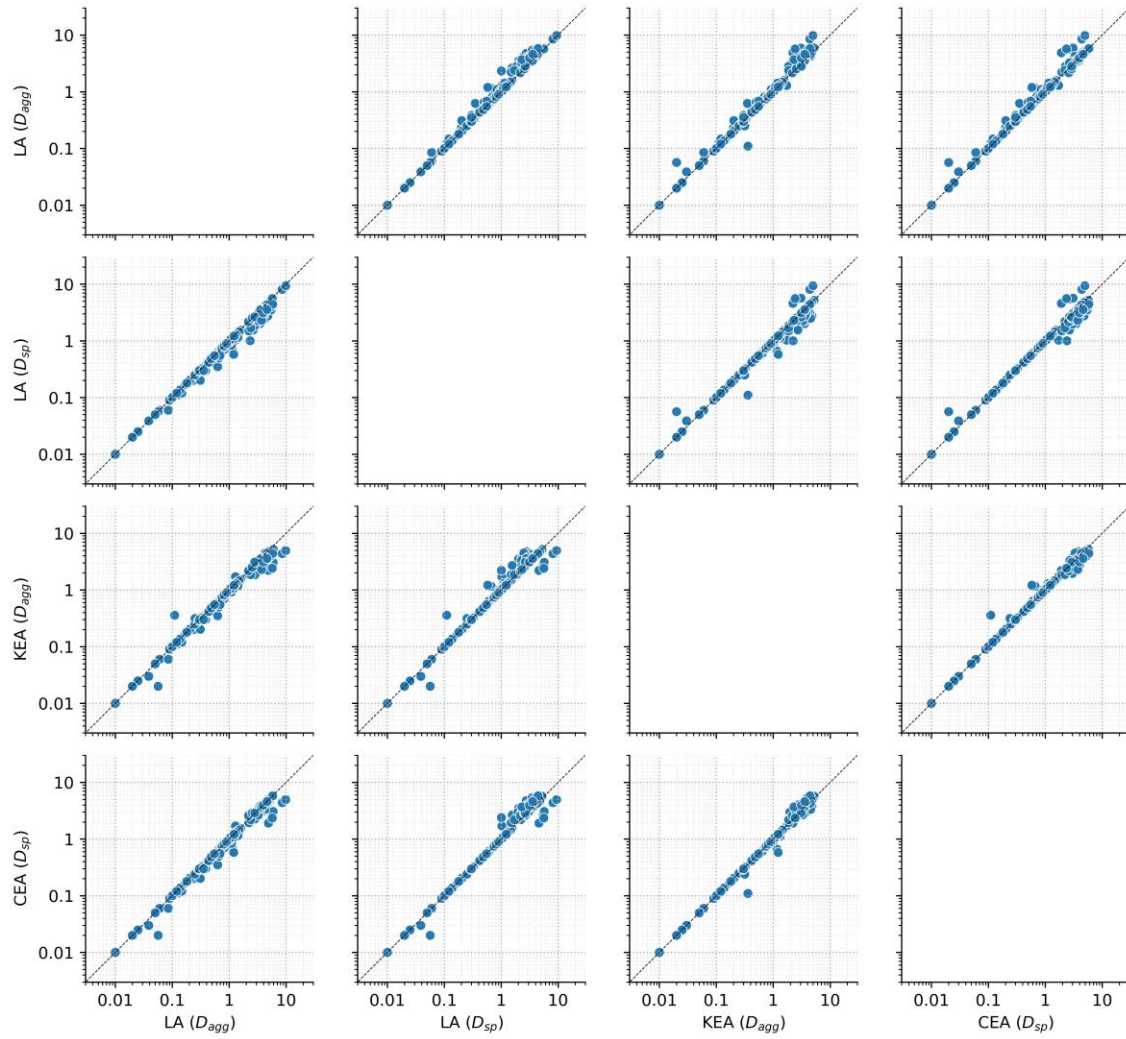


Figure A.18. Comparison of summed displacement results for each model (KEA24, CEA25, and LA23) based on measurement site for 2019 M 7.1 Ridgecrest-2, California earthquake.

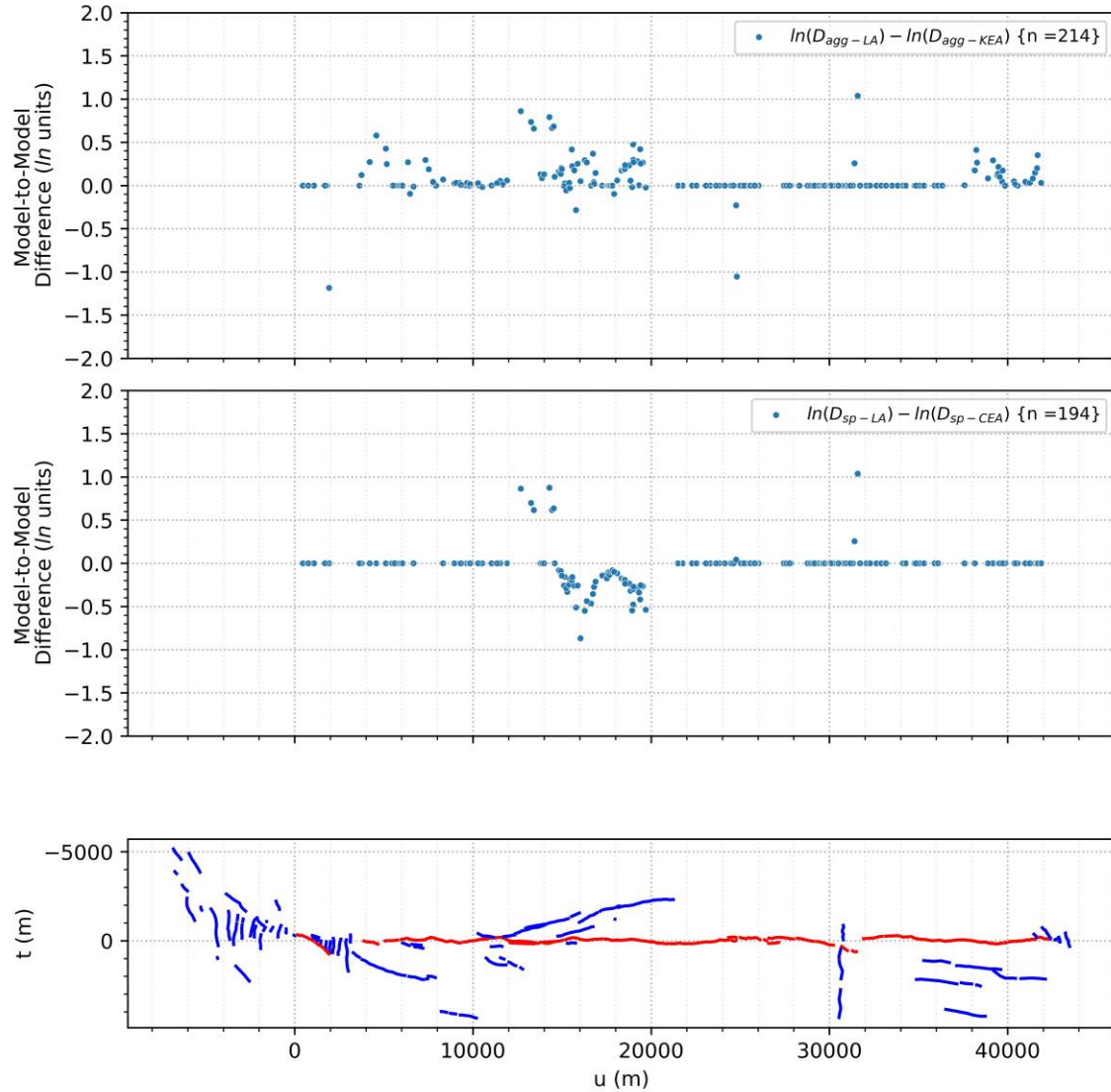


Figure A.19 Comparison of summed displacement results for D_{agg} and D_{sp} among the models as a function of rupture length for 2019 M 7.1 Ridgecrest-2, California earthquake. Principal (red) and distributed (blue) ruptures shown in projected (ECS) coordinates in bottom panel.

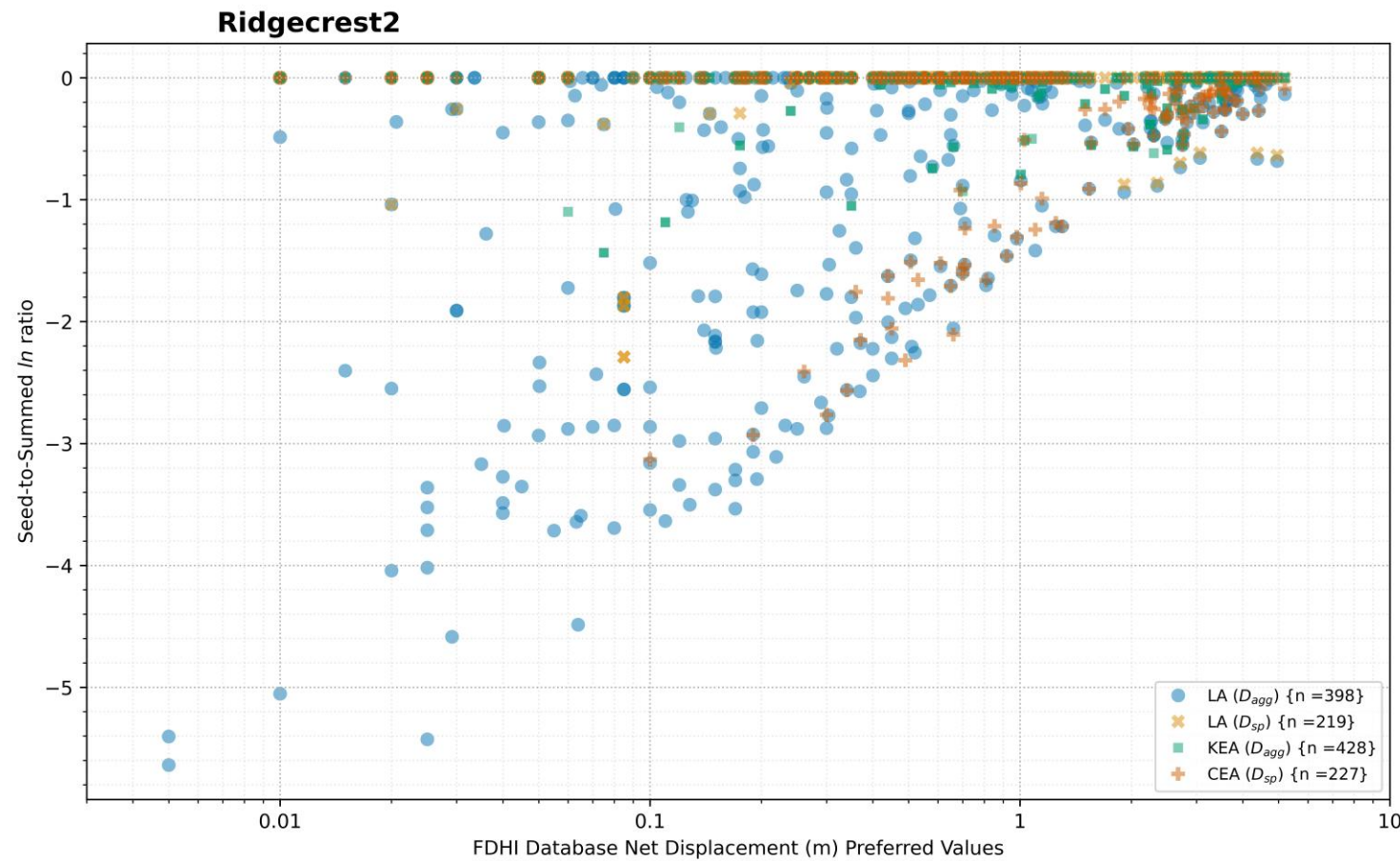


Figure A.20. Comparison of summed displacement results for each model (KEA24, CEA25, and LA23) as a function of seed measurement for 2019 M 7.1 Ridgecrest-2, California earthquake.

2.6 NEFTEGORSK

The 1995 M 7.0 Neftegorsk, Russia event was selected the surface rupture patterns are relatively simple.

The marginal density plot (Figure A.21) shows strong agreement in the spatial distribution of measurements along the rupture length for all models. The displacement amplitude densities are also in strong agreement for all models. This is expected due to the simplicity of the surface rupture data.

Generalized model comparisons can be made from the pair plots (Figure A.22) and are consistent with the trends in the displacement density plots. Where there are differences, the CEA model results are almost always slightly higher.

Visual inspection of the differences in values between models as a function of mapped ruptures (Figure A.23) reveals the largest differences are spatially associated with the northeast reach of the rupture ($u < 9,000$), where the CEA model treated some of the ruptures as principal instead of distributed. We infer that their approach for linear interpolation between measurement sites is contributing to the differences. In this area, the CEA results are higher than LA, and the LA results are higher than KEA.

The seed-to-summed log ratios (Figure A.24) reveal some consistent trends. The ratios decrease as the seed (single-site measurement) increases (as observed for other events; see discussion at the end of Section 2.1). The ratios amongst all models are similar overall.

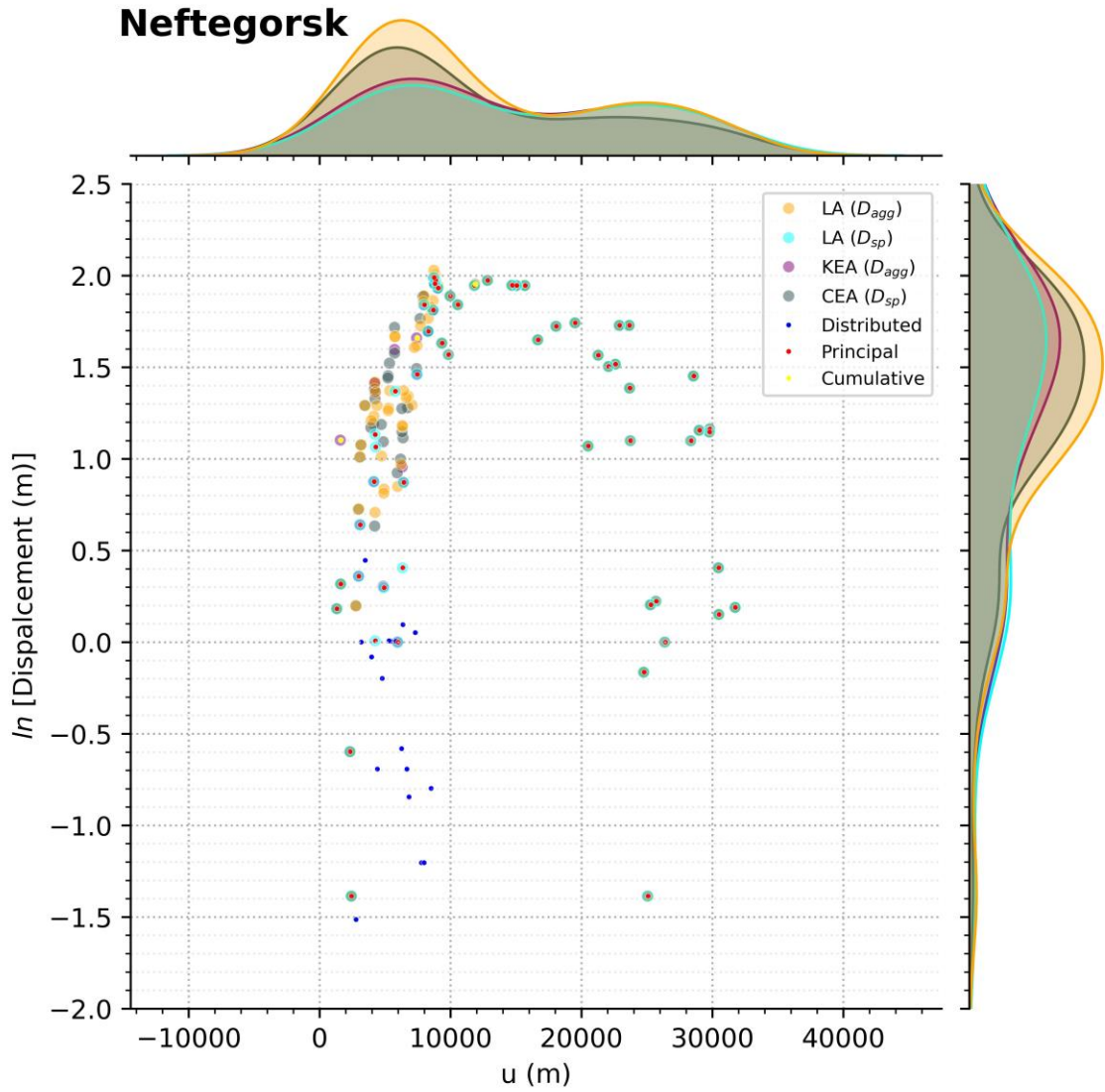


Figure A.21. Displacement measurements (Cumulative, Principal, and Distributed rank) from FDHI Database for 1995 M 7.0 Neftegorsk, Russia (FDHI EQ_ID =65) earthquake and summed displacements from KEA24, CEA25, and LA23 models. Marginal density plots shown for each model.

Neftegorsk, Displacement (m)

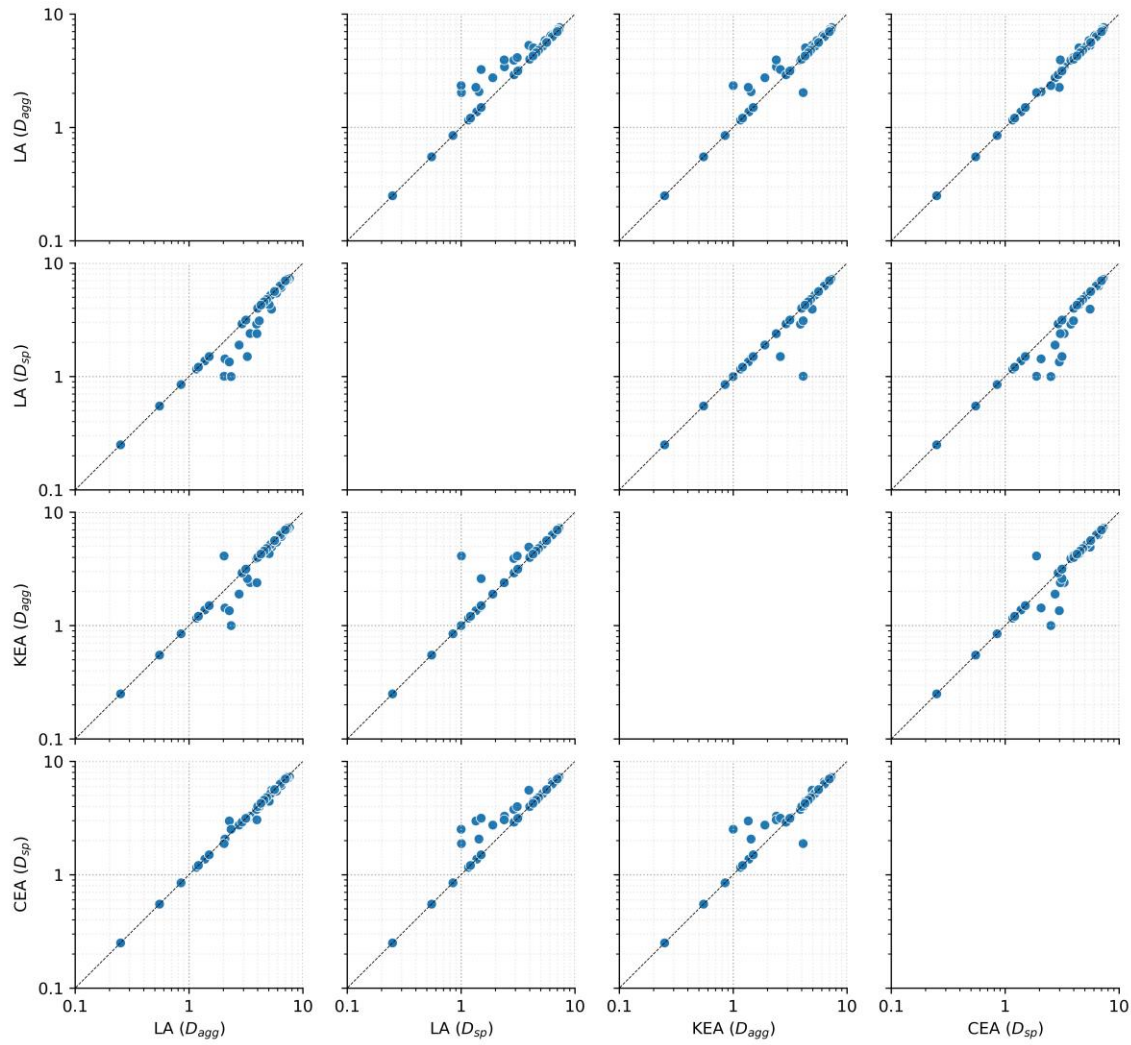


Figure A.22. Comparison of summed displacement results for each model (KEA24, CEA25, and LA23) based on measurement site for 1995 M 7.0 Neftegorsk, Russia earthquake.

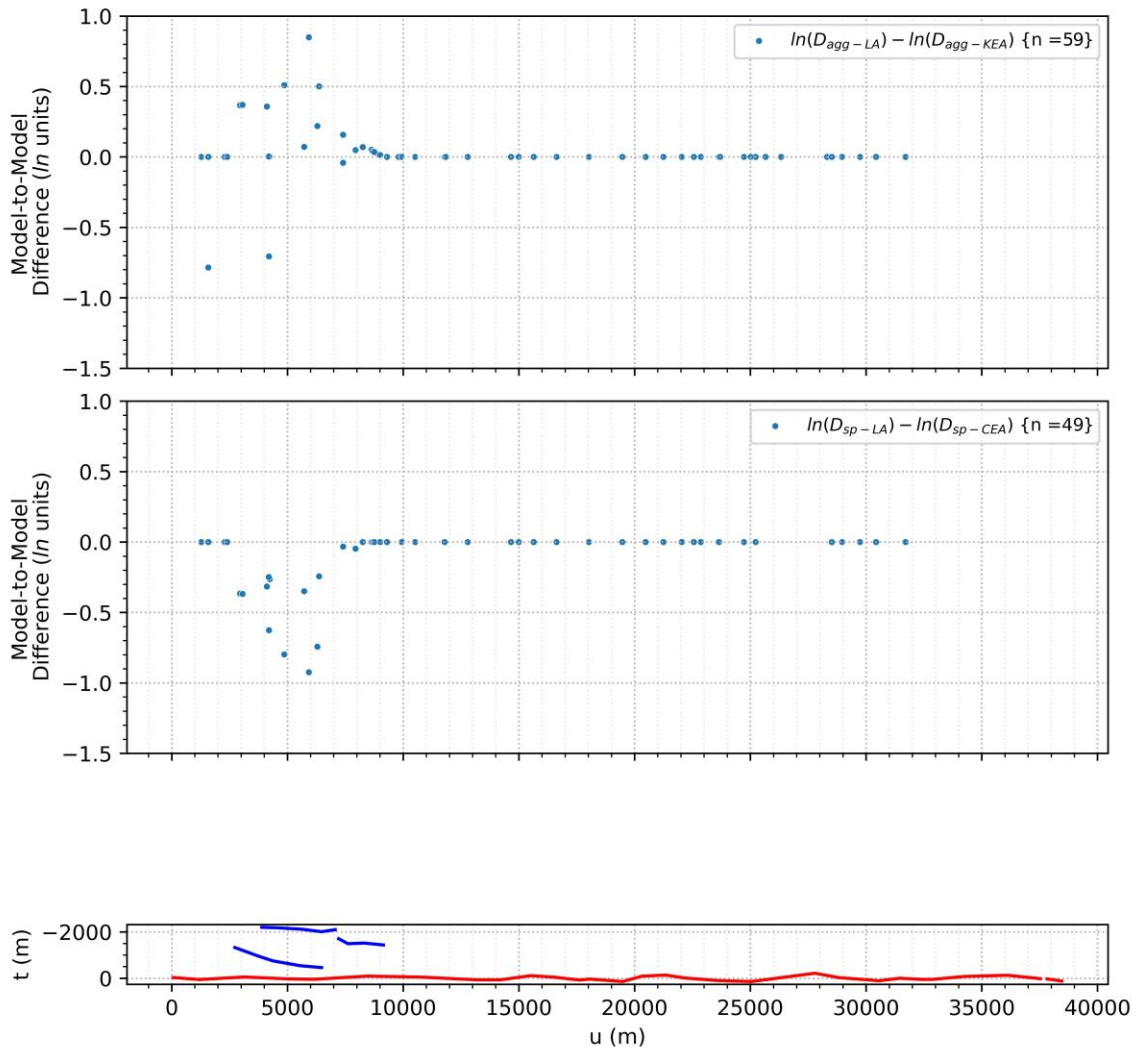


Figure A.23. Comparison of summed displacement results for D_{agg} and D_{sp} among the models as a function of rupture length for 1995 M 7.0 Neftegorsk, Russia earthquake.
Principal (red) and distributed (blue) ruptures shown in projected (ECS) coordinates in bottom panel.

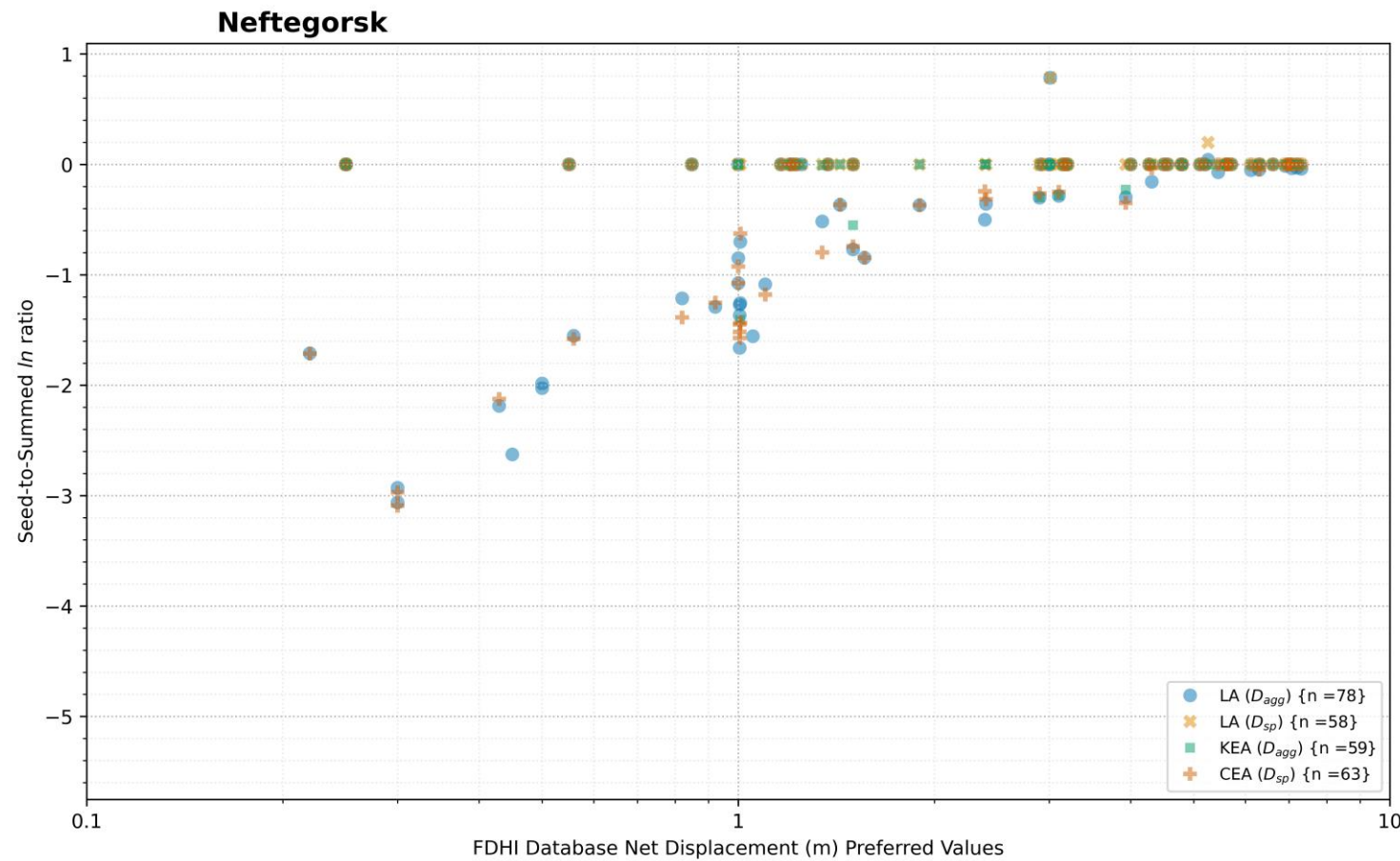


Figure A.24. Comparison of summed displacement results for each model (KEA24, CEA25, and LA23) as a function of seed measurement for 1995 M 7.0 Neftegorsk, Russia earthquake.

3 Summary

A Working Group convened in early 2021 to review results from different summation approaches for six earthquakes. This appendix documents comparisons in the form of measurement site and displacement amplitude density distributions, as well direct comparisons of the summed displacement amplitudes used in each model for each seed measurement site.

Overall, we find reasonable agreement between the LA23, KEA24, and CEA25 models. The differences are generally modest and are due to different methods used to sum measurements across (sub)parallel faults, using alternative rank classifications, or the inclusion of distributed displacement data. For example, the CEA25 model does not include distributed displacement measurements in their summation and used alternative interpretations of the rankings in the FDHI Database in some cases. These are modeler decisions and represent a component of epistemic uncertainty. Different techniques for summing the values are used among the models, which is also a component of modeling epistemic uncertainty. However, based on the findings of this Appendix, the differences in the summation methodology are modest.